

**Acta Universitatis Sapientiae**

**Electrical and Mechanical  
Engineering**

Volume 11, 2019

Sapientia Hungarian University of Transylvania  
Scientia Publishing House



# Contents

<i>S. Benzahiou, A. Metatla, A. Kerboua, D. Lefebvre, R. Bendib</i> <b>Use of Support Vector Machines for Classification of Defects in the Induction Motor .....</b>	<b>1</b>
<i>S. Vass, M. Zöldy</i> <b>Detailed Model of a Common Rail Injector.....</b>	<b>22</b>
<i>M. A. Eshag, M. Zarog</i> <b>The Effect of the Electrode Position on the Dynamic Behavior of an Electrostatically Actuated Microcantilever .....</b>	<b>34</b>
<i>A. Brahmia, R. Kelaiaia</i> <b>Design of a Human Knee Reeducation Mechanism .....</b>	<b>42</b>
<i>A. Ayadi, K. Meftah, L. Sedira, H. Djahara</i> <b>An Eight-Node Hexahedral Finite Element with Rotational DOFs for Elastoplastic Applications .....</b>	<b>54</b>
<i>K. Meftah, L. Sedira</i> <b>A Four-Node Tetrahedral Finite Element Based on Space Fiber Rotation Concept .....</b>	<b>67</b>
<i>A. Merah, R. Kelaiaia, F. Mokhtari</i> <b>A Liquid Metal Flow Between Two Coaxial Cylinders System .....</b>	<b>79</b>
<i>S. Guerbaai, M. Touiker, K. Meftah, A. Omara</i> <b>Numerical Study of Fluid Flow Through a Confined Porous Square Cylinder.....</b>	<b>87</b>
<i>E. Boussaha, S. Aouici, H. Aouici, A. Bahloul</i> <b>Study of Powder Particle Size Effect on Microstructural and Geometrical Features of Laser Claddings Using Response Surface Methodology RSM.....</b>	<b>99</b>





## Use of Support Vector Machines for Classification of Defects in the Induction Motor

Samia BENZAHIOUL<sup>1</sup>, Abderrezak METATLA<sup>1</sup>, Adlen KERBOUA<sup>1</sup>,  
Dimitri LEFEBVRE<sup>2</sup>, Riad BENDIB<sup>1</sup>

<sup>1</sup> Department of Mechanical Engineering, Faculty of Technology, University of August, 20, 1955, Skikda, Algeria, e-mail: {s.benzahoul, a.metatla, a.kerboua, r.bendib}@univ-skikda.dz

<sup>2</sup> Department of Electrical Engineering, Faculty of Sciences and Technologies, University of Le Havre, France, e-mail: dimitri.lefebvre@univ-lehavre.fr

Manuscript received September 22, 2018; revised June 15, 2019

**Abstract:** The classification and detection of defects play an important role in different disciplines. Research is oriented towards the development of approaches for the early detection and classification of defects in electrical drive systems. This paper, proposes a new approach for the classification of induction motor defects based on image processing and pattern recognition. The proposed defect classification approach was carried out in four distinct stages. In the first step, the stator currents were represented in the 3D space and projected onto the 2D space. In the second step, the projections obtained were transformed into images. In the third step, extraction of features whereas the Histogram of Oriented Gradient (HOG) is used to construct a descriptor based on several sizes of cells. In the fourth step, a method of classifying the induction motor defects based on the Support Vector Machine (SVM) was applied. The evaluation results of the developed approach show the efficiency and the precision of classification of the proposed approach.

**Keywords:** Induction motor, defect, pattern recognition, SVM, HOG, classification, detection.

### 1. Introduction

Today, squirrel cage asynchronous machines play an important role in the industrial world not only for their relatively low manufacturing cost, but also for their minimum maintenance requirements and their robustness. The asynchronous or induction machines have several advantages over other types of electrical machines. However, this kind of machines can suffer from some anomalies [1], resulting in the majority of cases in operational constraints that can cause the reduction of both production and yields rates, and in some cases the

process shutdown. Sophisticated supervision systems should be implemented to ensure the continuity and accuracy of operation, the safety of persons, the quality of services and to ensure that decisions are taken on ad-hoc basis. During the last 3 years, considerable efforts have been devoted to the detection and diagnosis of defects in the induction motors, and several researches and methods have been presented. These scientific works may be classified into two main fields.

- Methods based on models
- Methods based on signal processing

The methods of the first type use a reference model which is based on the analytical representation of the induction motor. For example, the method presented in [2] characterizes the winding function using the space harmonics while Tushar et al. [3], proposed a diagnosis method based on the use of direct and quadrature rotor currents to detect winding defects and to distinguish between stator winding defects and unbalanced supply voltage. In [4] authors presented another detection approach based on a multi-winding model. These studies have greatly enriched the modelling oriented points of view towards the diagnosis of defects in the induction motors.

On the other hand, in case of the method based on signal processing, the results are achieved by the extraction and quantification of measurable electrical or mechanical quantities related to defects. Several works have been developed in this context by researching internal and external indicators. Among them we mention the study carried out by Bonnet et al. [5] in the context of diagnosis of various rolling defects in the induction motor. Diallo et al. [6], presented a new method by using pattern recognition to detect rotor and stator defects in induction motors. Decision procedures, based on the k-nearest neighbor rule and direct limit calculation, were used to detect defects. In [7], the author has developed a method for pattern recognition based on a Multi-Layer Perception Artificial Neural Network (MLPANN) in order to detect and identify eccentricity defects and demagnetization of the synchronous machine. In a study presented in [8], the author used an approach that is based on the classical spectral analysis and a method of classification, inspired by the supervised learning theory of support vector machines (SVM), enabling the detection and identification of the ball bearing defect in the induction motor. In [9], the author proposes a technique of diagnosis of rotor electrical defects in the induction motor based on the analysis of acoustic signals collected from three motors.

In this study, we develop a new approach for detection and classification of defects in induction motors using learning algorithms for pattern recognition. The approach permits the detection of defects and classifies the majority of defects accurately and in real time. In order to allow an early classification of defects using the reduction of the number of samples, which facilitates online detection, the approach was optimized. Our goal is to synthesize a new diagnosis approach

and establish criteria of choice for their use in order to make a very advanced practical contribution to the diagnosis of defects in the induction motor. Our contribution can be summarized as follows.

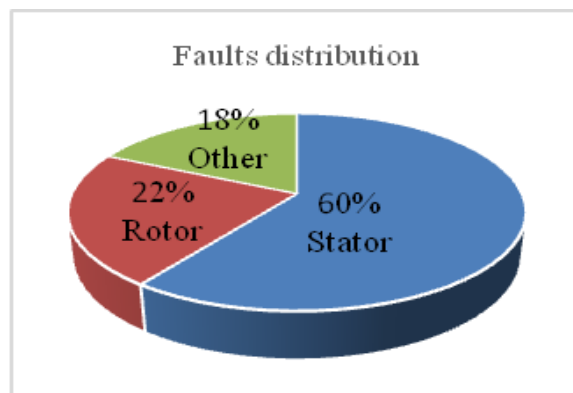
In the literature, many of the works use stator current processing with different signal processing approaches. In our study, instead of using stator current signal, we propose a Machine Learning approach based on image processing to classify defects in the induction motor.

We propose a defect diagnosis approach based on efficient classifier trained on small dataset.

This paper is organized as follows. In the sections 2 and 3 the test bench used in this work is presented. The fourth section concerns a flowchart description of the proposed method. Firstly, the stator currents are presented in the 3D and 2D spaces, followed by an application of two preprocessing operations (normalization and pixelization). Finally, the section was concluded by extracting points of interest and constructing a descriptor HOG. The fifth section is devoted to the presentation of SVM classifier used for classification of defects. The last section contains an experimental phase and discussion of the results. The study has been terminated by conclusion and perspective.

## 2. Defects in induction motors


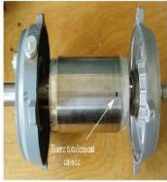

A defect of an induction motor means any accidental change in the normal operation. Defects have different origins: electrical, mechanical and magnetic. Statistical studies carried out by [6] on low and medium power induction motors are shown in *Fig. 1*.



*Figure 1:* Breakdown of defects in low and medium power induction motors.

In our study, we were interested in presenting at least one defect of each class in order to evaluate its influence on the behavior of the studied induction motor (*Table1*).

*Table 1*: Description of the defects in induction motors

Defects	Illustration	Causes	Effects
Rolling defect		<p>The rolling defect is generally related to the wear of the bearing and more specifically a degradation of the balls,</p> <ul style="list-style-type: none"> <li>*Wear due to aging,</li> <li>*High operating temperature,</li> <li>*Loss of lubrication,</li> <li>*Contaminated oil.</li> </ul>	<p>Oscillation of the load torque,</p> <ul style="list-style-type: none"> <li>*Appearance of additional losses,</li> <li>*Vibration by the displacement of the rotor around the longitudinal axis,</li> <li>*Generates impact on the power supply.</li> </ul>
Broken bar defect		<p>The break can be located either at its notch or at the end which connects to the rotor rings</p> <ul style="list-style-type: none"> <li>*The breaking of rotor bar is generally caused by: rotor/stator friction.</li> </ul>	<p>Induction of stator current harmonics in the winding</p> <ul style="list-style-type: none"> <li>*Reduction of the average value of the electromagnetic torque,</li> <li>*Increased oscillations of the rotation speed,</li> <li>*Mechanical vibration, abnormal operation of the machine</li> </ul>
Short circuit fault		<p>A short circuit defect for the same phase originates from an isolation defect in the concerned winding</p>	<p>An increase of the stator current in the affected phase, with a slight variation of the amplitude on the others,</p> <ul style="list-style-type: none"> <li>*Modification of the power factor and increase of the rotor circuit currents,</li> <li>*Increased temperature of the winding and accelerated isolation degradation.</li> </ul>



Different operation modes of the induction motor chosen for this study are listed in *Table 2* [10].

In the remainder of this paper, the following notations are used to denote different operating scenarios of the induction motor:

- \* Normal operating state:  $h$ ,
- \* Rolling defect:  $f_1$ ,
- \* Broken rotor bar:  $f_2$ ,
- \* Short circuit defect 2% ( $f_3$ ),
- \* Short circuit defect 5%.

*Table 2:* Operation modes of the induction motor used

Motor operating state	The loads %	Number of tests
Normal operating state ( $h$ )	20,50, 100	60
Rolling defect ( $f_1$ )	0, 20, 60, 100	22
Broken rotor bar defect ( $f_2$ )	0, 20, 60, 100	80
Short circuit defect 2% ( $f_3$ ) (Short circuit 2% means that 2% of the total number of turns are short circuited)	10, 20, 40	15
Short circuit defect 5% ( $f_4$ ) (Short circuit 5% means that 5% of the total number of turns are short circuited)	10, 20, 40	15
	Total	192

A test bench was realized to perform different scenarios or operating modes of an induction motor 450 W, 127V, 50 Hz, a pole pair and rotational speed 1480rpm.

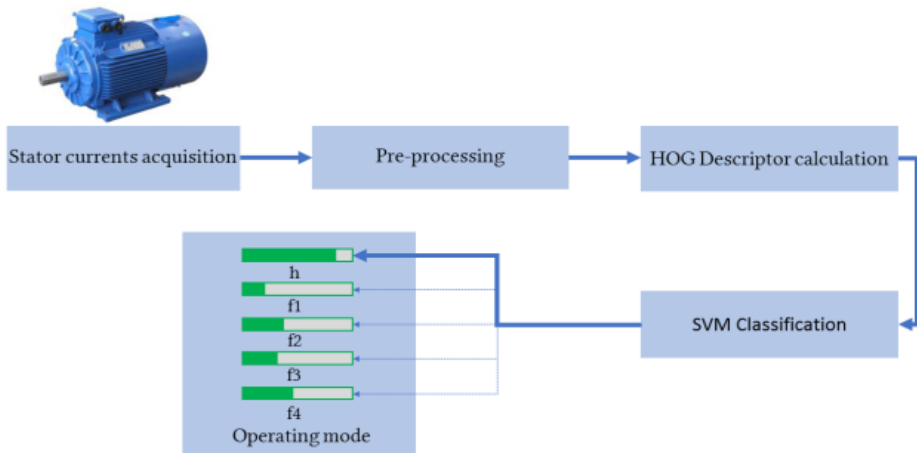
All the acquisitions were carried out at steady state over a period of 10 seconds, with sampling frequency equal to 10 KHz, i.e. 100001 samples for each of the following measured signals [10]:

- \* The line current of three stator phases,
- \* The three supply voltages,
- \* The electromagnetic torque.

### 3. The proposed approach used for defect detection

The principle of the approach developed in this work is based on the use of pattern recognition techniques in images representing the characteristic signals of each operation mode.

Our approach is divided into four stages. In the first step, we represent the magnitudes of the three phase system of the stator currents in the 3D space, followed by a projection on the three 2D spaces. In the next step, the preprocessing operations were performed. Firstly, scaling of the heterogeneous data was performed to facilitate their comparison. Secondly, a pixelization operation of the data was performed (graphical representation for the signals in 2D space). In the third step, a descriptor was computed by HOG algorithm containing a set of points of interest represented by two essential parameters, which are the modulus and the orientation of the local gradient [11]. In the last step, SVM classifier was used to label different operating scenarios of the induction motor [12]. The different stages of the developed approach are presented in *Fig. 2*.



*Figure 2:* Architecture of the used classification methodology.

#### 4. Representation of the currents in 3D space and the projection of the trajectories in 2D spaces

In general, a system of three quantities of the same nature and frequency is the superposition of three balanced systems of the same frequency: a three-phase direct system, a three-phase inverse system and a homopolar system. In practice, this means that the system of the three voltages or of the three currents can be represented by the components  $x_d$ ,  $x_i$  and  $x_0$  (voltages or currents) such that [10]:

- $x_d$ : represents the direct symmetrical component,
- $x_i$ : represents the inverse symmetrical component,
- $x_0$ : represents the homopolar component.

The 3D graphical representation of the three-phase stator currents also makes it possible to present plans or surfaces defined by a parametric equation or by a Cartesian equation of type:

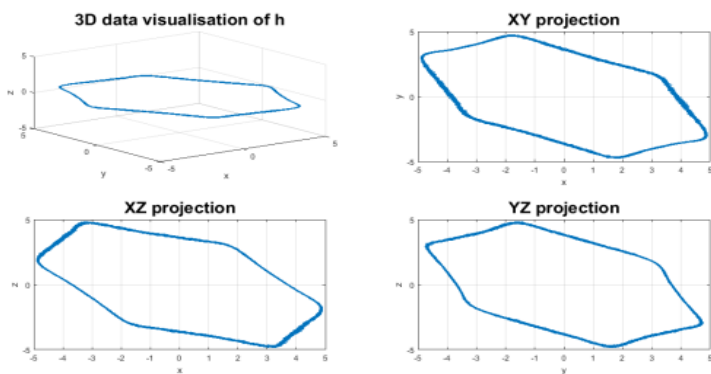
$$z = f(x,y) \quad (1)$$

with  $x = c$ ,  $y = i_{bs}$  and  $z = i_{cs}$ .

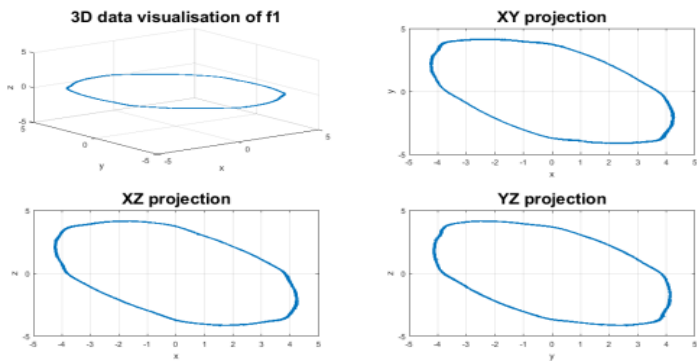
The projection of the three stator currents is in the parallel type projection plane depending on whether the projection direction is perpendicular to the projection plane  $xoy$ ,  $xoz$  and  $yoz$ .

In the case of the three-phase currents in healthy induction motor, the projections of currents  $i_{as} = f(i_{bs})$ ,  $i_{cs} = f(i_{as})$  and  $i_{bs} = f(i_{cs})$  on the three planes  $xoy$ ,  $xoz$  and  $yoz$ , are called Lissajous curves. This presentation has a circular shape centered at the origin and diameter equal to the magnitude of the stator currents corresponding to the state of operation of the machine. In the case of the faulty motor, the Lissajous curve changes in shape and thickness due to the presence of the harmonics created by the fault. This strategy consists in comparing the curves of Lissajous that result from the operation with and without faults. This strategy is not valid in our case because of the use of a real database containing measurement noise and state which makes lose the centered form of the Lissajous curve. For this purpose, we proposed a technique based on the transformation of the Lissajous curve into an image, then we applied the SVM for the detection and classification of defects.

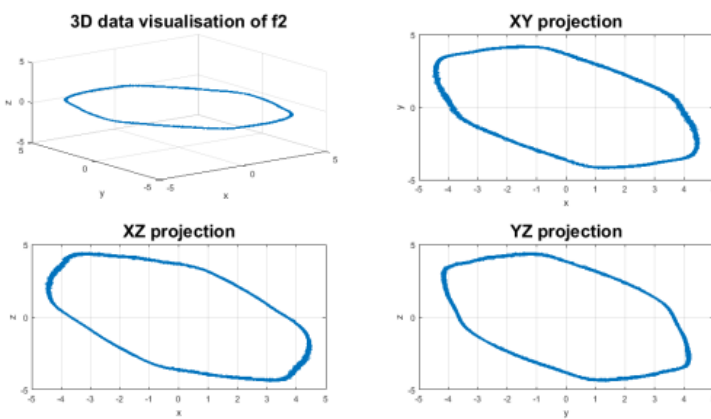
*Fig. 3* shows in different operation modes the three phase stator currents  $i_a$ ,  $i_b$  and  $i_c$  in the 3D space, and the projections of the trajectories in 2D space by applying (1). It was found that each mode of operation corresponds to a specific shape of the projections.



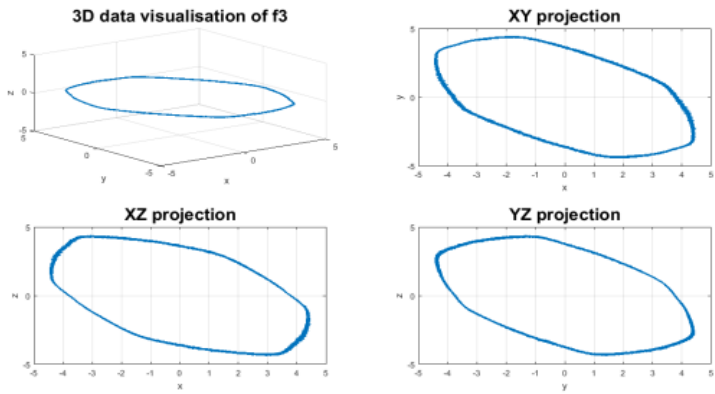
(a)



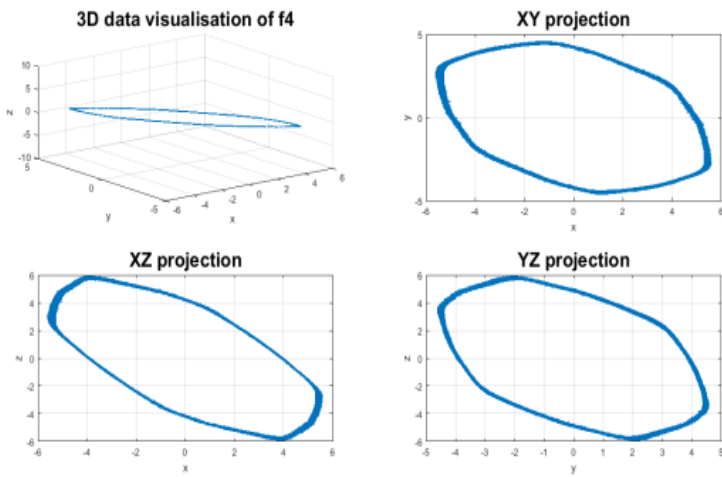
(b)



(c)



(d)



(e)

Figure 3: Representation of three stator currents in 3D space and projection in 2D planes for each operation mode: a. Healthy state; b. Rolling fault; c. Bearing fault; d. Short circuit fault 2%; e. Short circuit fault 5%.

## 5. Preprocessing

This step involves two operations. Firstly, normalization of the data (standardization) was carried out to a range  $[-1, 1]$  and, secondly, a pixelization step [13] is applied.

### 5.1. Normalization step

In order to compare the different magnitudes and to minimize the interclass variations with respect to the applied load, the scaling is done to let the data belong to  $[-1, 1]$ . *Fig. 3* illustrates the stator current with different loads before and after normalization. It can be seen that the change in load affects the shape size. For 20 % load (*Fig. 4.a*), signals vary in the range  $[-5, 5]$ , while a 100% load generates oscillating signals in a range  $[-9, 9]$ . The shapes represent the same operating state (interclass variation), which can lead to confusion for the classifier. After standardization (*Fig. 4.b*), the set of signals is included in the same interval  $[-1, 1]$ .

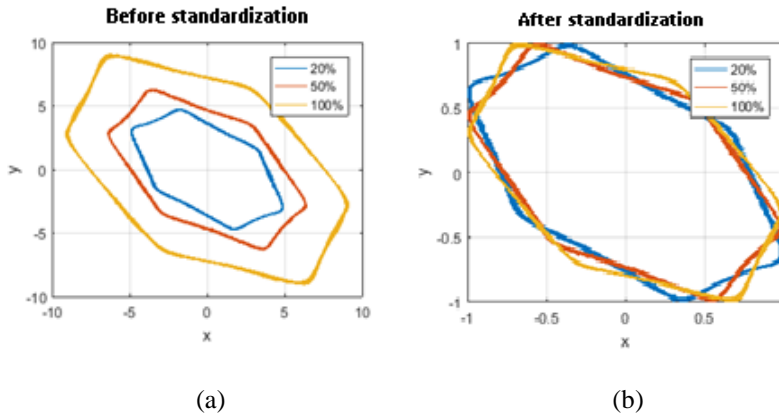


Figure 4: a. Before standardization; b. After standardization

The applied algorithm is expressed by the following formula by posing:  $[lim_1, lim_2] = [-1, 1]$ .

We can write:

$$\begin{cases} i_a = \left( \frac{i_a - \min(i_a)}{\max(i_a) - \min(i_a)} * (\lim_2 - \lim_1) \right) + \lim_1 \\ i_b = \left( \frac{i_b - \min(i_b)}{\max(i_b) - \min(i_b)} * (\lim_2 - \lim_1) \right) + \lim_1 \\ i_c = \left( \frac{i_c - \min(i_c)}{\max(i_c) - \min(i_c)} * (\lim_2 - \lim_1) \right) + \lim_1 \end{cases} \quad (2)$$

This operation results in keeping all characteristics of the appearance of the pattern.

## 5.2. Pixelization step

It is the transformation of the 2D data to a graphic from (image) by the representation of each signal sample measured by a pixel of intensity corresponding to the value of the reduced dimension so as not to lose the information relative to it:

For example, a pixel in the XY plane is represented by its coordinates (x,y) corresponding respectively to the two currents  $i_a$  and  $i_b$ , while the pixel intensity is the value of  $i_c$ . In fact, each measured signal sample was represented by the coordinates and the gray level intensity of one pixel to produce specific pattern for every operating mode. The algorithm applied for the three planes XY, YZ and XZ is as follows:

$$\begin{cases} (i_a * resolution, i_b * resolution) = i_c \\ (i_c * resolution, i_a * resolution) = i_b \\ (i_b * resolution, i_c * resolution) = i_a \end{cases} \quad (3)$$

Given that  $i_a, i_b$  and  $i_c \in [-1, 1]$ , these transformations allows us to obtain positive and not null integer indices which can be positioned in 2D images with well-defined resolutions. Our algorithm is based on the processing of images faithfully representing the system evolution in relation to time while being of reduced sizes in order to speed up the training process. In our case several resolutions have been used such as (64\*64), (128\*128), (256\*256) and (512\*512). The following figure illustrates the obtained images.

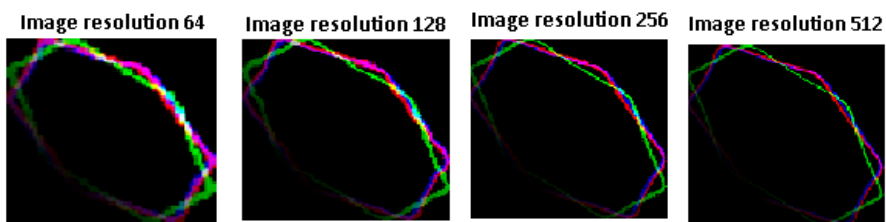


Figure 5: Image with different resolutions.

It can be that the image resolution (128\*128) represents almost the same level of detail as the image resolution (256\*256) while having only a quarter of pixel (1/4). However, the image resolution (128\*128) loses fine detail. So our choice is to use the image resolution (256\*256) which represents a good compromise between the data size of the encoded image and the level of desired detail.

## 6. Construction of the descriptor

Local characteristics refer to pattern or structure distinct immediate surroundings by texture, color or intensity. Their descriptors which are compact vector representations of a local neighborhood are the constitutive elements of many algorithms of computer vision. Their applications include pattern recognition, image recording, object detection and classification [14].

In our algorithm, we used the descriptor HOG adapted to the tasks of classification of deformable objects. It decomposes the image into square cells of a given size (CellSize) covering the entire image on one hand, and it computes, on the other hand, a histogram of oriented gradients in each cell by constructing the image gradient  $\nabla \ell(x, y)$  and using the central difference [11].

The images obtained during the pixelization phase have particular shapes for each mode of operation of the induction motor. This change of shape from one state to another, once characterized in a robust manner by the extraction of a HOG descriptor, can be used to train the classifier. Therefore, it is important to make sure that the HOG feature vector encodes the right amount of information about the local orientations in the images. The effect of the cell size parameter on the amount of the shape information encoded in the feature vector can be seen by varying the HOG cell size parameter ([4 4], [8 8], [16 16], [32 32] and [64 64]) and visualizing the result presented in *Fig. 6*.



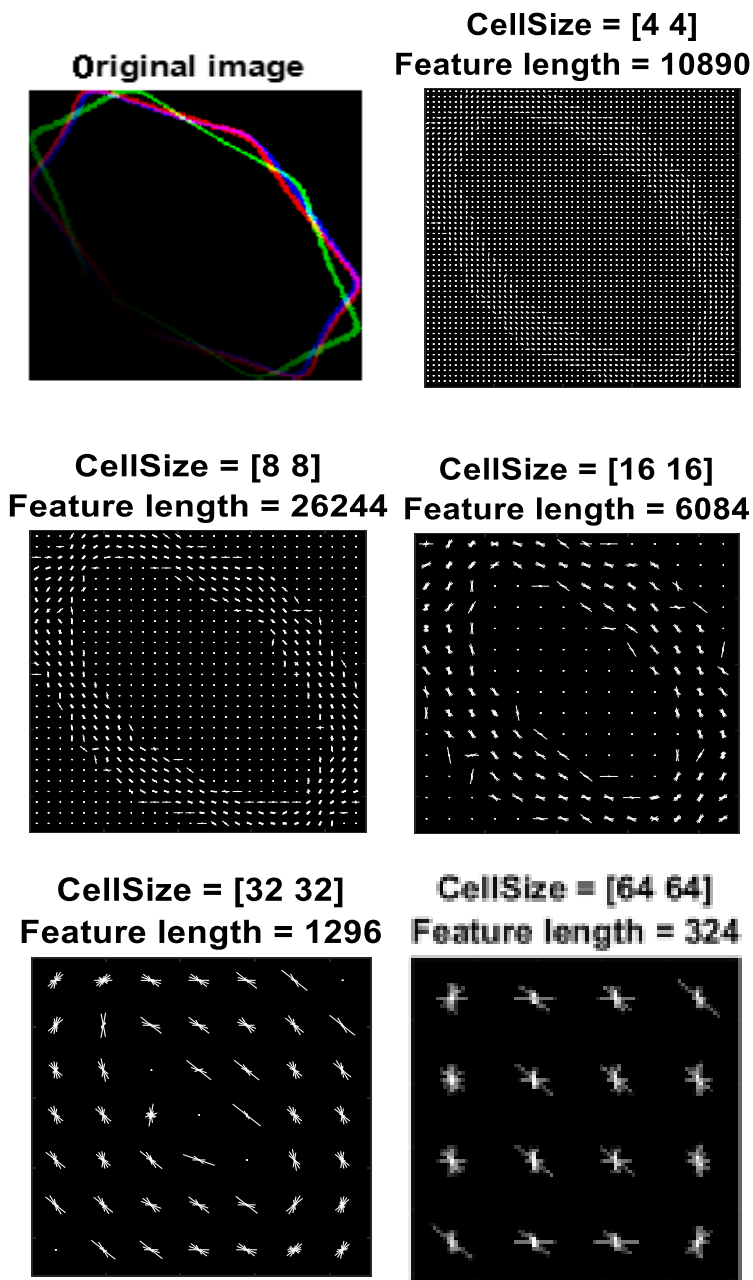


Figure 6: Effect of the cell size on the HOG descriptor.

It is found that cell sizes [64 64] and [32 32] do not give sufficient information about shapes, whereas a cell size of [4 4] contains a lot of shape information, but increases substantially the descriptor size. A good compromise would be to choose the two intermediate cell sizes [8 8] and [16 16] which are evaluated during the experimentation phase. This adjustment of the chosen cell size has sufficient information to enable us to visually differentiate the shape corresponding to the operating state concerned, while limiting the size of the descriptor, which makes it possible to accelerate the driving phase.

We assume that the final descriptor is the concatenation of the three descriptors extracted from the three images of the 2D projections (XY, YZ and XZ) as follows:

$$HOG = [HOG_{x,y}, HOG_{y,z}, HOG_{x,z}] \quad (4)$$

Using the cell size of [8 8] for each of the three-projection images, a total number of  $34596 \times 3 = 103788$  points of interest have been obtained. For the first descriptor [16 16] we get  $8100 \times 3 = 24300$  points of interest.

Since the obtained descriptor contains noise and redundant information, which affect the classification score and lead to unnecessary increases in the computation time. The application of the Principal Component Analysis (PCA) algorithm eliminates redundancy and noise. It is found that the 573 most representative elements contain more than 98% of the distinctive information.

## 7. Support vector machines (SVM) and mathematical principle

Support Vector Machines (SVM) are a set of supervised classification techniques. SVMs were developed by Vapnik et al. [15] as part of a statistical theory of learning. The SVMs have been applied to many fields and have become one of the most widely used models for classification and regression. The basic use of SVMs is the resolution of binary problems with two classes.

An SVM algorithm classifies the data by calculating the best hyper-plane that separates all the points belonging to one class from those of the other class. The best hyper-plane is the one with the widest margin between the two classes. The SVM is represented by the data points closest to the separation hyper-plane and those at the edge of the class to which the closest class belongs. *Fig. 7* illustrates this definition [16].

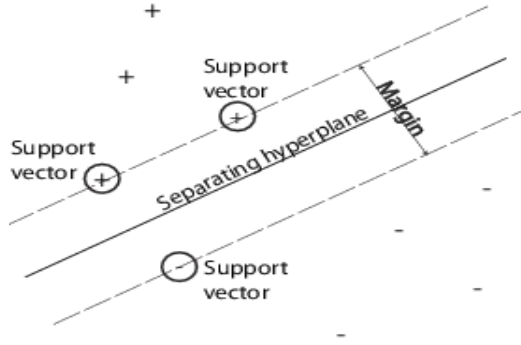


Figure 7: Principle of the SVM.

The + indicates the points of the first class, the – indicate the points of the second class.

The training data are a set of points or vectors  $x_i$  with their categories  $y_i$ . For some dimension  $d$  the  $x_j \in R^d$ , and the  $y_j = \pm 1$ . The equation of the hyper-plane is given by:

$$f(x) = x^T \beta + b \quad (5)$$

where,  $\beta \in R^d$  and  $b$  are real numbers.

The next problem defines the best separation hyper-plane between the two classes (i.e. the decision boundary). The calculation of  $\beta$  and  $b$  serves to minimize  $\|\beta\|$  such that for all the vectors  $(x_j, y_j)$ .

$$y_j f(x) \geq 1 \quad (6)$$

The support vector machines values  $x_i$  on the boundary between the two classes which satisfy the following condition:

$$y_j f(x) = 1 \quad (8)$$

The problem can be seen as a minimization of  $\|\beta\|$  which is a quadratic programming problem. The optimal solution  $(\beta, b)$  makes it possible to classify a vector  $z$  according to the following formalization:

$$\text{class}(z) = \text{sign}(z^T \hat{\beta} + b) = \text{sign}(\hat{f}(z)) \quad (9)$$

where  $\hat{f}(z)$  is the classification score which represents the distance of the vector  $z$  with respect to the decision boundary.

SVMs were originally developed to handle binary problems but they can be adapted for the handling of multi-class problems. We can distinguish two main

schemes: the first “one against all”, which consists in transforming the problem with  $k$  classes into  $k$  binary classifiers, whereas the second one is called “one against one”, this strategy consists in transforming into  $(k*(k-1))/2$  binary classifiers. In this work, we focus on the supervised classification of defects in the induction motor by the use of an OVA (One Versus All) multi class SVM [12,14].

This type reduces the classification problem with three or more classes into a set of simple binary classifiers. For each binary classifier, one class is positive and the others are considered negative. The chosen scheme requires a coding model which determines the training classes and a coding scheme which determines the aggregation of the prediction of the binary classifiers.

In this work, we have five (05) classes ( $h, f_1, f_2, f_3$  and  $f_4$ ) and consequently five classifiers. The coding model is represented by the coding matrix  $M$  of 5 rows and 5 columns. Each row represents a class and each column represents the SVM responsible for detecting the corresponding class as indicated in *Table 3*.

*Table 3*: Coding model or coding matrix  $M$

Class SVMs	SVM <sub>1</sub>	SVM <sub>2</sub>	SVM <sub>3</sub>	SVM <sub>4</sub>	SVM <sub>5</sub>
$h$	+	-	-	-	-
$f_1$	-	+	-	-	-
$f_2$	-	-	+	-	-
$f_3$	-	-	-	+	-
$f_4$	-	-	-	-	+

For the cells containing “+” the classifier should group all the observation in the classes corresponding to the positive class.

On the other hand, for the cells containing “-” the observation should be grouped in the classes corresponding to the negative class.

If  $m_k$  is the element of the matrix  $M$  at the row  $k$  and the column  $i$  ( $k, i \in \{1,2,3,4\}$ ), and  $s$  is the score of the classification of the positive class of the classifier SVM<sub>1</sub>, then a new observation is assigned to the class ( $k$ ) which minimizes the aggregation of the losses for the SVM<sub>1</sub> according to equations (9)

$$\hat{k} = (\operatorname{argmin}_k (\sum_{i=1}^5 |m_{ki}| g(m_{ki}, s_i)) / \sum_{i=1}^5 |m_{k,i}|) \quad (9)$$

## 8. Experiments

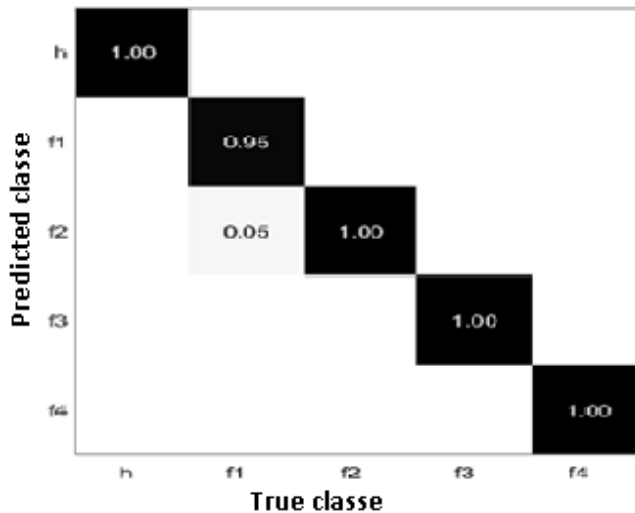
To be able to diagnose defects quickly, there is a need to make compromise between training speed, memory usage, accuracy and interoperability. This is

why we have chosen to use in this work a multi-class SVM classifier of the OVA type, with a cubic function of the kernel without standardization of the data that has already been done during the preprocessing phase.

Our algorithm is essentially written in MATLAB. We used Image Processing Toolbox TM and Statistics and Machine Learning Toolbox TM. The application is run on a Core i3 processor with a clock of 2.4GHz and 6GB of RAM.

The experiment consists of several scenarios starting with an evaluation of the distinctive strength of our descriptor. In order to make an equitable evaluation of the performance of our method, the Cross-validation protocol with K-Folds (K is equal to five), we partition the data into five (5) randomly chosen subsets. Each subset is used to validate the classifier driven on the rest of the subset. This process is repeated K times (K=5 in our case) so that each subset is used exactly once for validation. The mean of the cross-validation error is used as a performance indicator in order to avoid the phenomenon of over-fitting.

As the classification score obtained by classifying them with descriptors obtained using cells of sizes [8 8] and [16 16] is the same, *Fig.8* illustrates the confusion matrices obtained by the SVM classifier with a descriptor using cells of sizes [8 8].



*Figure 8:* Confusion matrix obtained by the SVM driven by HOG using cells of sizes [8 8].

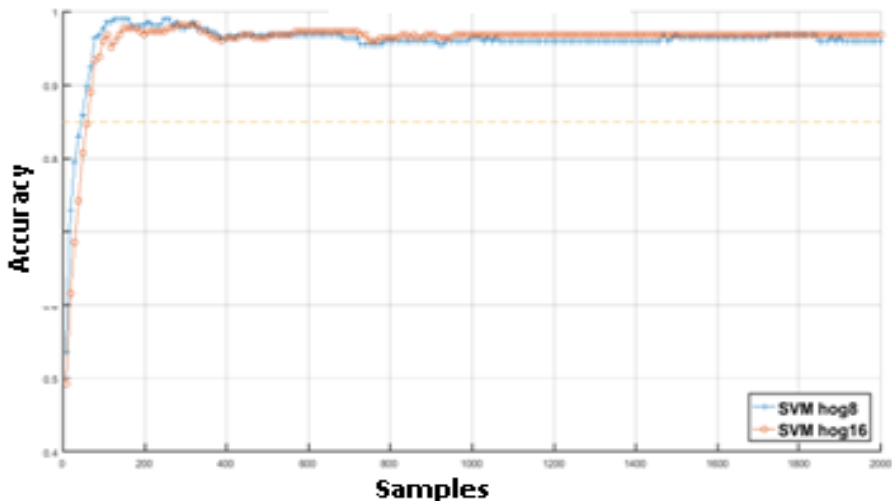
It is found that the results obtained by the SVM classifier driven by HOG descriptors using cells of sizes [8 8] and [16 16] give the same overall classification score of 99.5%. In both cases, only one operating state was misclassified, i.e. an operating state with a fault  $f_1$  was mistakenly classified as a defect in  $f_2$  with a percent of 5%. The use of a descriptor with cells of size [16 16] gives a faster execution response than that of the descriptor with cells of size [8 8], with an execution time of 1.8077 and 6.2389 seconds respectively.

## 9. Accuracy of defect classification

To ensure the safety of people and equipment in industrial field a system is needed to know the occurrence of a defect in real time. These type of systems are affected by two main factors:

1. The time needed to make a good prediction,
2. The time needed to make a good decision.

We test our method by reducing the number of samples necessary to create a descriptor to obtain a good classification (minimization of execution time or fast response speed), in order to evaluate the minimum number of samples necessary to obtain a good classification of the defects. *Fig. 9* illustrates the number of samples necessary to give a good decision with the classifier used.



*Figure 9:* Minimum number of samples for decision.

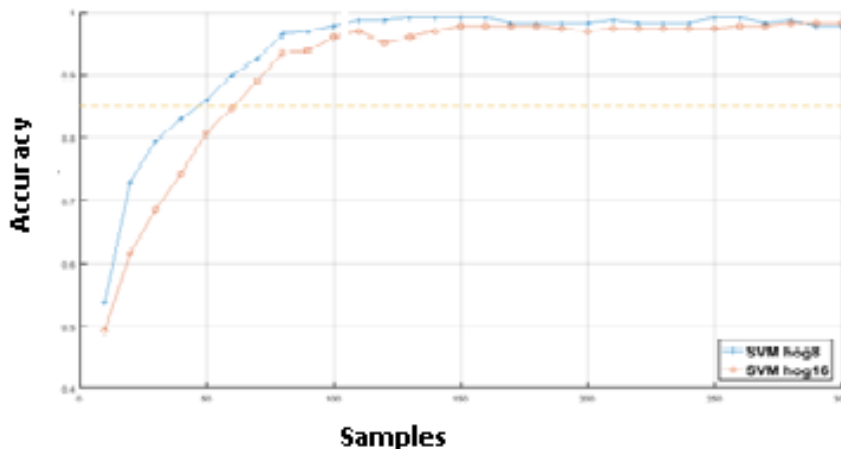


Figure 10: Minimum number of samples for decision.

As illustrated in *Fig.10*, it can be seen that the use of 10% to 15% of the samples is sufficient to achieve a score equivalent to the best score obtained in the previous experiment and using all the data.

## 10. Conclusion

This paper has focused on classification of induction motor defects, especially on the stator short circuit, the broken rotor bar and the rolling defect.

Through this work, it was shown that the monitoring and diagnosis of defects in the induction motor by stator current monitoring is an essential tool for obtaining clues as to the operating state of the induction motor. The occurrence of a defect causes a change in the shape and position of the stator currents represented in the 3D or 2D plane. The use of the pattern recognition technique makes it possible to detect and even identify certain defects in the induction motor, but the use of this technique remains limited for classification and quantification of defects. To this end, a new approach has been proposed for monitoring and classifying these defects. The proposed approach is developed through the realization of several steps starting by representing the stator currents in 3D space and the projection of their trajectories in 2D space followed by the pixelization process where the image resolution 256\*256 represents a good compromise. The last step is dedicated to the construction of the descriptors with different sizes of the cells. The results obtained by the various descriptors show that the descriptors using cells of sizes [8 8] and [16 16] present a good compromise and have sufficient significant information. The results obtained also

show that the developed approach gives a good classification score of the majority of defects with good decision and fast response. In our future work, an attempt will be made to develop modern techniques, classify defects with good accuracy and to increase response speed in more complicated systems such as multi-source energy systems.

## References

- [1] Ondel, O., Boutleux, E., and Clerc, G., "A method to detect broken bars in induction machine using pattern recognition techniques", *IEEE Transactions on Energy Conversion, Institute of electrical and Electronics engineers*, vol 20 (3), 2006, pp. 512-519.
- [2] Toliyat, H. A., and Lipo, T. A., "Analysis of a concentrated winding induction machine for adjustable speed drive applications. Part 2: Experimental results", *IEEE Transaction on Energy Conversion*, vol. 9(4), 1994, pp. 695-700.
- [3] Vilhekar, T. G., Ballal, S. M., and Suryawanshi, H. M., "Detection of winding faults in wound rotor induction motor using loci direct and quadrature axes of rotor currents", *Electrical power components and systems*, vol. 45, (11), 2017, pp 1217-1230.
- [4] Ritchie, E., Deng, X., and Jokinen, T., "Dynamic model of 3-phase squirrel cage induction motors with rotor faults", *ICEM '94*, B6(2), France, 2004, pp. 694-698.
- [5] Bonnett, A. H., "Cause and analysis of anti-friction bearing failures in A.C induction motors", *IEEE Transactions on Industry Application, Sept/Oct*, 1993, pp. 14-23.
- [6] Diallo, D., Benbouzid, M. E., Hamad, D., and Pierre, X., "Fault detection and diagnosis an induction machine Drive: A pattern recognition approach based on Concordia stator mean current vector", *IEEE Transactions on energy conversion, Institute of electrical and Electronics engineering*, vol 20 (3), 2005, pp 512-519.
- [7] Guota, K., and Kaut, A., "A review on fault diagnosis on induction motor using artificial neural networks", *International journal of science and research*, Vol, 3(7). pp. 680-684, 2014.
- [8] Tafinine, F., Mokrani, F., Antoni, K., Kabla, J., and Asradj, Z., "Introduction des SVM en MCSA", *4th International conference, Sciences of electronic, technologies of information and telecommunications*, pp.1-7 March 25-29, Tunisia, 2007.
- [9] Glowacz, A., "Recognition of acoustic signals on induction motors with the use of MSAF10 and bayes classifier", *Arc. Metall. Mater*, vol, 60 (1), 2016, pp. 153-158.
- [10] Sahaoui, M., Ghoggal, A., Zouzou, S., and Benbouzid, E. M. E., "Dynamic eccentricity in squirrel cage induction motors-simulation and analytical study of its spectral signatures on stator currents", *Simulation Modelling Practice and Theory*, 2008, pp. 1503-1513.
- [11] Navneet, D., and Triggs, B., "Histograms of oriented gradients for human detection", *International Conference on computer Vision and Pattern recognition, (CVPR'05), San Diego, United States*, pp.886-893, 10.1109/CVPR.2005.177. inria-00548512.
- [12] Christianini, N., and Shawe-Taylor, J., "An Introduction to Support Vector Machines and Other Kernel-Based Learning Methods", computer science, mathematics, *Cambridge University Press, Cambridge, UK*, pp. 103-109. Published 2000. DOI: 10.1017/CBO9780511801389.012
- [13] Hadeif, M., Djerdir, A., Ikhlef N., Mekideche, M. R., and N'diaye, A. O., "A Fault severity index for stator winding faults detection in vector controlled PM synchronous motor", *J. Electr Eng Techno*, vol 10 (6), pp.2326-2333 2015.



- [14] Namdaran, M., and Jazayeri-Rad, H., "Incipient fault diagnosis using support vector machines based on monitoring continuous decision functions", *Engineering Applications of Artificial Intelligence*, vol 28, 2014, pp 22-35.
- [15] Weston, J., and Watkins, C., "Support vector machines for multi-class pattern recognition", In *Proceedings of the Seventh European Symposium on Artificial Neural Networks (ESANN 1999)*, pp. 219-224. MIT Press, Cambridge, MA, 1999.
- [16] Vapnik, V., "Statistical Learning Theory", *Wiley, New York*, 1998.
- [17] Gelbart, M., Snoek, J. R., and Adams, P., "Bayesian Optimization with Unknown Constraints", <http://arxiv.org/abs/1403.5607>, 2014.

## Detailed Model of a Common Rail Injector

Sándor VASS<sup>1</sup>, Máté ZÖLDY<sup>2</sup>

<sup>1</sup>Department of Automotive Technologies, Faculty of Transportation Engineering and Vehicle Engineering, Budapest University of Technology and Economics, Budapest,  
e-mail: sandor.vass@gjt.bme.hu

<sup>2</sup>Department of Automotive Technologies, Faculty of Transportation Engineering and Vehicle Engineering, Budapest University of Technology and Economics, Budapest,  
e-mail: mate.zoldy@gjt.bme.hu

Manuscript received February 29, 2019; revised July 16, 2019

**Abstract:** This work is about the validation of a Common Rail (CR) injector model. The model describes injector internal behavior in a detailed way, validation is done using dosage measurements and needle lift traces.

The model contains fluid dynamic, mechanic and electro-magnetic parts describing all important internal processes. To compare the modelling results against measurement data, three test cases were chosen on a medium duty test engine to represent a wide range of operation points. Dosage measurements were done by averaging the injected mass of 1500 injections, each measurement repeated three times. Needle displacement was measured using an injector equipped with a needle lift sensor in the same operating points. The results of the simulated injector and the measured values showed good conformity both in needle displacement and injected fuel mass, so the model can be a basis for further injector and combustion analyses.

**Keywords:** Common Rail, injector, simulation, modelling, validation, internal combustion engines.

### 1. Introduction

Introduction of the Common Rail (CR) injection systems was one of the most important steps in injection developments. CR systems offer a flexibility in injection pressure, timing and length under any engine operating point [1]. CR systems separate the pressure generation physically from the fuel metering, eliminating injection pressure drop at low speeds and loads, a hallmark of conventional injection systems [2]. This flexibility, coupled with the possibility of cutting the injection into three to seven phases, allows more control over the combustion and exhaust after treatment processes, as they mostly depend on the air-fuel mixing and burning during and after the injection event. However, it is highly time and resource consuming to set up the system for all operating points

of different engines. Controlling combustion is the best tool to minimise tail pipe emission that is one of the most neuralgic barriers of the utilisation of diesel engines [3,4].

It is challenging to measure the internal mechanisms of a CR injector, due to the high pressures, quick pressure changes, small chambers and holes, fast operation and high flow velocities. The best solution for these problems is to create a detailed model of the injector, where all hydraulic, mechanic and electromagnetic subsystems are represented, so the internal working conditions can be analysed in an economical and efficient manner.

As CR systems became more and more popular, CR injector models continuously appeared in literature more and more frequently. Some tried to model the whole injection system, including high pressure pump and rail pipes [5-6], making them very complex, but most works contained only the injector itself. Control oriented models with simplified structures were developed [7-8], but most of the papers describe injector operation in a detailed manner. However, the latter mostly included only mechanical and fluid dynamical parts [9-13]. Publications rarely contain the electromagnetic circuit of the solenoid, but the work of Bianchi et al. stands out [14-17], as a complete, detailed and validated CR injector. If the solenoid model is neglected, usually an interpolation of force data acting on the anchor is used instead [18-19].

Elastic axial deformation of the needle and control piston is taken into consideration in all works, along with the injector body if necessary [20]. This phenomenon affects the effective needle displacement and the needle-seat passage area at the orifice holes crucially, so it cannot be neglected.

An accurate fluid dynamic part is also a key factor of CR injector modelling. Cavitation is always a part of that, since it affects the discharge coefficient of the nozzle and other holes, and through this on the injected fuel mass. This is why much emphasize was put on determining and describing this phenomenon occurring in various hole geometries [21].

Based on the references listed above, a CR injector shall employ three main model types: an electrical, a hydraulic and a mechanical one. If the goal is to create an accurate and predictive injector model, all three of them have to be considered and simulation results shall be compared to measurement data. There can be several aspects of injector model validation, e.g. mechanical parts, fluid dynamic behavior, etc. In this paper the needle movement measurements will be used to validate the mechanical and electromagnetic systems, while the dosage measurements serve to validate the hydraulic description. These together describe injector operation comprehensively and if simulation results show good conformity with the measurement data, the model can be stated valid.

## 2. Injector model

The model described below was based upon a Bosch CRIN1 type injector for commercial vehicles. The description of the internal buildup and detailed working principles of the injector can be seen in [2].

A hybrid model containing electromagnetic, hydraulic and mechanical parts was built up in order to maintain accuracy and study of the injectors' internal processes. The structure was first presented in [22], and then validated against control piston lift measurements in [23], but dosage validation was needed to make it predictive.

The model was implemented in a commercial simulation software named GT-Suite, in the GT-Fuel submodule. It is capable of calculating problems in different disciplines of physics, i.e. it is capable of electromechanical, thermal, fluid-dynamical and mechanical simulations [24].

### A. The mechanical model

Mass-spring-damper scheme was used to model the moving part of the injector. Masses in the simulation environment may translate with a given velocity in planar directions; equations are based on Newton's second law and calculated in every coordinate direction.

Viscous, elastic and body forces are also calculated during simulation, external forces can also be applied.

As *Fig. 1* shows, the injector needle in this model is handled as a rigid body, although the high working pressures of the injection system causes appreciable deformation of the parts. Modelling of this phenomenon has a critical importance on the accuracy of the simulation. To simulate the change of the actual needle stroke due to deformation, material stiffness and damping was reduced into one element, namely the control piston. The mass of the control piston was split into two parts with identical masses and connected by a spring and a damper element. These could be described as resultant stiffness and damping of the whole system, which could be defined using measurement results of the needle lift sensor and the line pressure sensor. As the needle lift sensor indicates the control piston stroke change due to deformation, the force acting on the piston can be obtained from the measured fuel pressure and the piston diameter. This method eliminates the laborious work of defining the stiffness of all different parts one by one and provides accurate results.

Evaluation of the damping factor is far more difficult, considering that the damping factor shall include elements not only by the internal friction, but also from fluid viscosity and friction between piston and liner. Experimental evidences show that the friction component of the damping is more important,

but it cannot be evaluated theoretically, since machining tolerances affect it mostly. Therefore, damping must be estimated during the model tuning phase.

Masses of all parts were measured using a medical grade scale. Contact stiffnesses were estimated during the model tuning phase, here the main target was to adjust the bouncing of the needle, control piston and solenoid anchor according to other measurements in literature.

### *B. Hydraulic model*

The hydraulic model strictly follows the system layout. This means that all volumes downstream the high pressure tubes coming from the rail, down to the nozzle holes are modelled, containing all internal flow passages defined with the exact geometries as they were manufactured. The rail tube and high pressure pump is replaced by an unsteady pressure boundary condition, which was measured in the rail tube during the injection event. Thus the hydraulic system of the injector has been modelled as a network of pipes and chambers connected by orifices, higher level components from the software model library were used to calculate hydraulic forces caused by fuel pressure and flow and fuel leakage is also modelled at the joint surfaces. Calculation is based on one-dimensional, unsteady, compressible flow and takes into consideration the dynamics of the attached mechanical components and structural heat transfer. *Fig. 1* and *Fig. 2* show the hydraulic and mechanical model parts of the injector. In *Fig. 1* the injector body is presented, while *Fig. 2* shows the assembly located in the solenoid.

The geometrical parameters needed in fluid-dynamic equations were measured and implemented in the model; the characteristics of the three main orifices can be followed in *Table 1*. The diameters of internal flow passages and pistons, chambers were measured using simple slide-gauge. Smaller holes i.e. A- and Z-throttles were measured with the help of a microscope and a microscope scale ruler. The geometry nozzle hole was defined by a destructive measurement method, where a similar nozzle body was cut through the axis of a nozzle hole, so the length, diameter and shape of the hole could be determined (*Fig. 3*).

Because pressure and temperature can remarkably vary in CR systems, it is important to have accurate properties of the medium. In these simulations ISO4113 test oil was used; density, dynamic viscosity and bulk modulus were given as functions of temperature and pressure.

*Table. 1:* Geometric parameters of orifices ( $D_h$  - diameter of hole,  $L$  – length of hole,  $r$  – inlet corner radius)

	$D_h$ [ $\mu\text{m}$ ]	$L$ [mm]	$r$ [ $\mu\text{m}$ ]
Injector orifice hole	152	1	20
Hole A	268	0.6	65
Hole Z	220	0.47	55

### *C. Electromagnetic model*

The electromagnetic model of the solenoid is responsible for transforming input current to mechanical force acting on the anchor mass through magnetic circuits. The electromagnetic force is considered by the mechanical model part and anchor dynamics are calculated according to its value. It is calculated based on the reluctance of the circuit: when current begins to flow in the coil, magnetic flux flows through the elements and electromagnetic force will be generated between the surfaces of the air gaps. A detailed explanation of the system and its working principles can be found in [25].

## **3. Results and discussion**

### *A. Test bench layout*

All measurements were realized using a four cylinder turbocharged Diesel engine installed on an engine test bench [26]. Due to the specific high pressure fuel connection of the CRIN1, an injector mount would be difficult to manufacture, so a cylinder head similar to the one on the engine was used to accommodate the injector (*Fig. 4*). One of the injectors on the engine was disconnected from the rail tube and the ECU. A flexible high pressure fuel hose was mounted between the rail and the injector fuel inlet, to provide fuel supply to the examined injector, thus the engine ran with three cylinders while the connections of the fourth drove the examined injector.

The tested injector was equipped with a needle lift sensor measuring control piston movement; a current clamp was used to record the driving current of the injector, while a line pressure sensor measured instantaneous rail pressure.

Different injection pressures and excitation times were reached by setting different engine operation points on the test bench in the most commonly used engine speed and load range.

Injections occurred in a measuring glass in order to measure the cumulated injected mass, from which the dosage could be calculated.

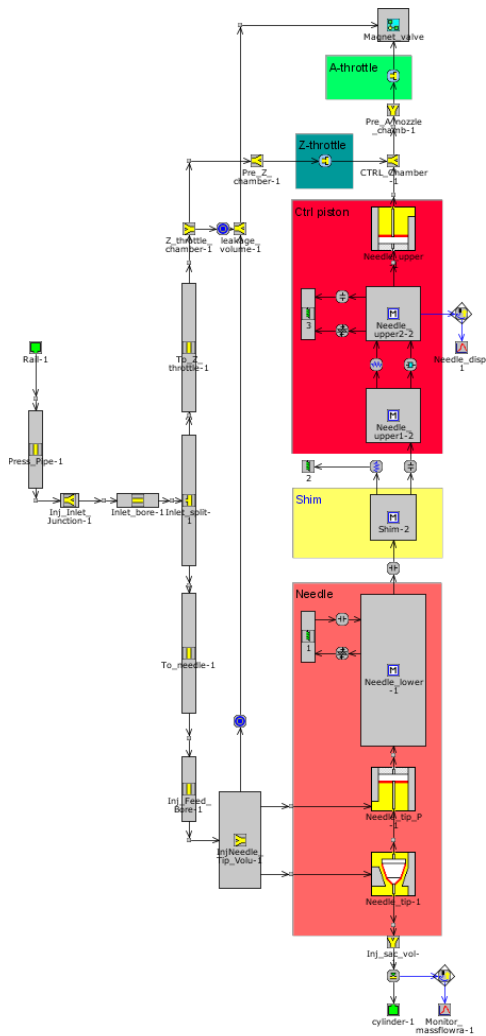


Figure 1: Hydraulic and mechanical models of the injector body.

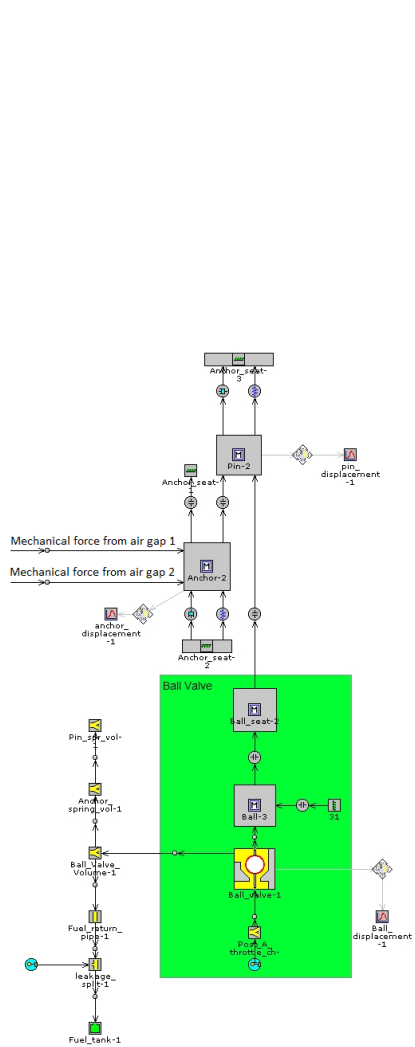


Figure 2: Hydraulic and mechanical models of the solenoid assembly.

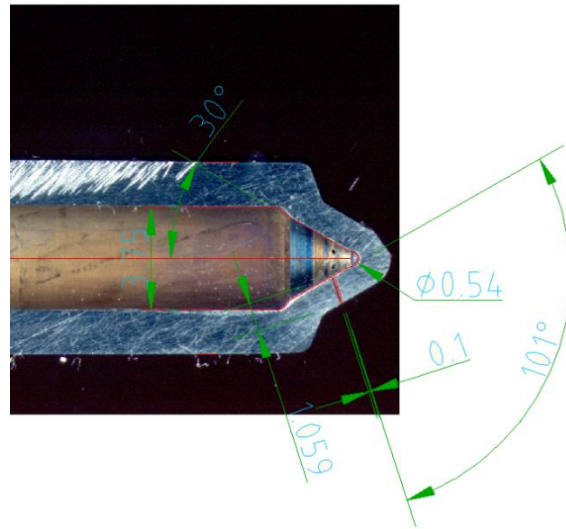


Figure 3: Geometry of the injector nozzle hole.

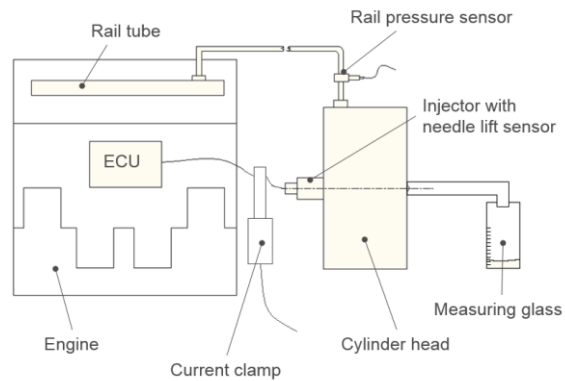


Figure 4: Test-bench layout.

### B. Test cases and boundary conditions

Three different test cases are presented in this work with three different engine operating points. The engine speeds, loads and the corresponding measured injection pressures and excitation times can be followed in *Table 2*.



Table. 2: Test case parameters

Test case	Engine speed [Rpm]	Engine torque [Nm]	Injection pressure [bar]	Excitation time [ms]
1	1500	300	680	2.55
2	1500	200	540	1.9
3	1500	100	450	1.15

### C. Validation and results

The model has been validated by comparison with measurements in terms of injector control piston lift and injected dosage. Needle lift could not be directly measured, the sensor recorded the control piston position. Dosage was calculated from the cumulated injected mass, derived from the number of injections.

Three experimental cases were studied with different rail pressures and opening times. All of the cases represent single injections without pre or post phases, because this particular engine does not use pilot or post injection in the main operation range. Control piston lifts of the three cases can be followed in Fig. 5.

The effect of axial deformation of the control piston and needle is obvious on these position traces. Case 1 has the largest stroke, because rail pressure is the highest here and along with rail pressure the axial force increases also. It is worth noticing that stroke difference reaches 20 $\mu$ m between cases 1 and 3. It is also worthwhile to point out the ‘humps’ at the beginning of every needle lift. This is caused by the sudden pressure drop when the ball valve opens the control chamber and the control piston expands axially before the actual movement begins.

All simulations follow the measured traces with good accuracy. To determine this accuracy, the root mean square (RMS) errors were calculated for every case based on the following equation:

$$\varepsilon_i = \sqrt{\frac{1}{T} \int_0^T \left( \frac{l_{i,meas} - l_{i,sim}}{l_{i,meas}} \right)^2} \quad (1)$$

where:

$\varepsilon_i$  - RMS error,

$T$  - simulation time range,

$l_{i,meas}$  - measured control piston lift,

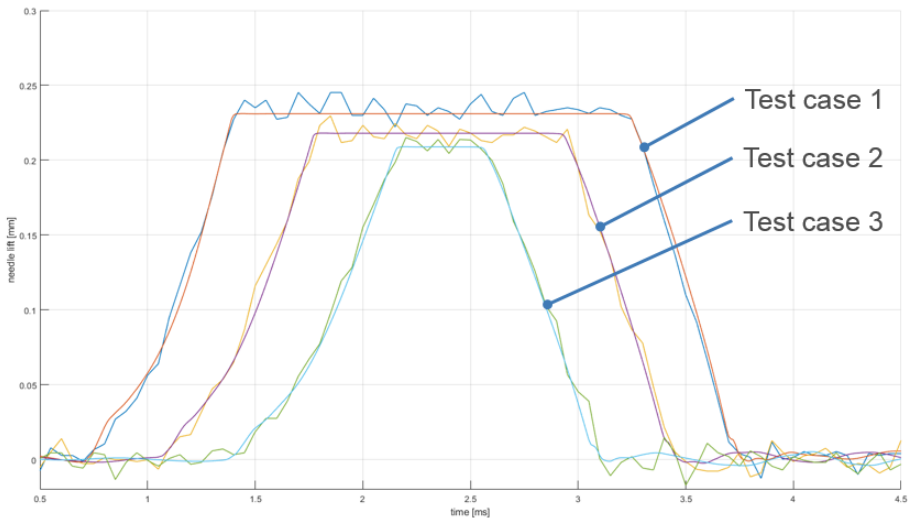
$l_{i,sim}$  - simulated control piston lift.

In all cases a certain amount of noise can be noticed, but it stays in a tolerable range, so no filtering was used. This way the time shift of the filter was avoided and more accurate results could be provided.

The RMS values are presented in *Table 3*. All RMS error values are less than 1%, so based on *Fig. 5* with the results shown in *Table 3*, it can be stated, that the simulation predicts the needle lifts of the injector accurately.

Dosage calculation was based on cumulative injected mass measurement. Measuring time was chosen to get a sufficiently large cumulated injected mass value and number of injections, this way measuring accuracy could be increased. All measurements were repeated three times. *Table 4* contains the measuring circumstances, measured and simulated dosage values.

*Table 5* shows the absolute and relative deviations of the simulated dosage. Looking at the deviation values it can be clearly stated, that the model reproduces measured dosage accurately in the studied operating points. All deviation values are below or equal to 2%.



*Figure 5:* Measured and simulated control piston lifts for test cases 1 to 3.

*Table 3:* RMS error of the needle lifts

Test case	RMS error
1	0.0054
2	0.0054
3	0.0054

Table 4: Measured and simulated dosage

Test case No.	Measuring time [s]	Measured mass [g]	Number of injections [pcs]	Dosage [mg]	Simulated dosage [mg]
1	120	140,41	1500	93,60	91,38
2	120	90,32	1500	60,21	59,40
3	120	48,88	1500	32,59	33,25

Table 5: Measured and simulated dosage deviation

Test case No.	Deviation [mg]	Deviation [%]
1	2,22	<b>2,03</b>
2	0,81	<b>0,48</b>
3	0,66	<b>0,22</b>

## 4. Conclusion

In this paper a detailed model of a CR injector for commercial vehicles was presented and validated against needle lift data and dosage values. Three test cases were chosen to represent operation points in the mostly used partial load range. The simulated control piston movement and injected mass accurately matched the measured curves and values in every test case.

The fluid dynamic and mechanic model parts were presented in details to investigate the working principles of the injector internal parts. Simulation validation against injection rate measurements shall be done in the future to make the model fully predictive.

## References

- [1] Strumpp, G., Ricco, M. "Common Rail – An Attractive Fuel Injection System for Passenger Car DI Diesel Engines", *SAE Technical Paper Series* 960870, 1996.
- [2] Zellbeck, H. and Schmidt G. "Einspritzsysteme für zukünftige Anforderungen an schnellaufenden Dieselmotor", *MTZ*, vol. 56, no. 11, pp. 648-655, 1995.
- [3] Tutak W, Jamrozik A, Bereczky Á and Lukács K. "Effects of injection timing of diesel fuel on performance and emission of dual fuel diesel engine powered by diesel/E85 fuels", *TRANSPORT (VILNIUS)*, vol. 33, no. 3, pp. 633-646, 2018.
- [4] Farkas, O., Szabados, G., Antal, Á. and Török, Á. "Experimental Investigation of Discoloration Generated by a CI ICE's Exhaust Gas on Various Stone Types", *Periodica Polytechnica Transportation Engineering*, vol. 46, no. 3, pp. 158-163. doi: <https://doi.org/10.3311/PPtr.12120>, 2018.
- [5] Sabau, A., Barhalescu, M. and Oanta, E. "Modeling of high pressure fuel injection systems", *Annals of DAAAM for 2012 & Proceedings of the 23rd International DAAAM Symposium*, vol. 23, no.1, 2011.

- 
- [6] Chiavola, O., Giulanelli, P. "Modeling and Simulation of Common rail Systems", *SAE Technical Paper Series*, 2001-01-3183, 2001.
  - [7] Lino, P., Maione, B. and Rizzo, A. "Nonlinear modelling and control of a common rail injection system for diesel engines", *Applied Mathematical Modeling*, vol. 31, pp. 1770-1784, 2007.
  - [8] Palamondon, E., Seers, P., "Development of a simplified dynamic model for a piezoelectric injector using multiple injection strategies with biodiesel / diesel-fuel blends", *Applied Energy*, no. 131, pp. 411-424, 2014.
  - [9] Brusca, S., Giuffrida, A., Lanzafame, R. and Corcione, G. E. "Theoretical and experimental analysis of diesel sprays behavior from multiple injections common rail systems", *SAE Technical Paper Series*, 2002-01-2777, 2002.
  - [10] Catalano, L. A., Tondolo, V. A. and Dadone, A. "Dynamic rise of pressure in the common rail fuel injection system", *SAE Technical Paper Series*, 2002-01-0210, 2002.
  - [11] Digesu, P., Ficarella, A., Laforgia, D., Bruni, G. and Ricco, M. "Diesel Electro-Injector: A Numerical Simulation Code", *SAE Technical Paper Series*, 940193, 1994.
  - [12] Mulemane, A., Han, J-S., Lu P-H., Yoon, S-J. and Lai, M-Ch. "Modeling Dynamic Behavior of Diesel Fuel Injection Systems", *SAE Technical Paper Series*, 2004-01-0536, 2004.
  - [13] Payri, R., Climent, H., Salvador, F. J. and Favenec, A. G. "Diesel injection system modelling. methodology and application for a first-generation common rail system", *Proceedings of the Institution of Mechanical Engineering*, vol. 218, part D, 2004.
  - [14] Bianchi, G. M., Pelloni, P., Corcione, E. and Luppino, F. "Numerical analysis of passenger car HSDI diesel engines with the 2nd generation of common rail injection systems: The effect of multiple injections on emissions", *SAE Technical Paper Series*, 2001-01-1068, 2001.
  - [15] Bianchi, G. M., Falfari, S., Pelloni P., Filicori, F. and Milani, M. "A Numerical and Experimental Study on the Possible Improvements of C.R. Injectors", *SAE Technical Paper Series*, 2002-01-0500, 2002.
  - [16] Bianchi, G. M., Falfari, S., Pelloni P., Kong, S-C. and Reitz, R.D. "Numerical Analysis of High Pressure Fast-Response C.R. Injector Dynamics", *SAE Technical Paper Series*, 2002-01-0213, 2002.
  - [17] Bianchi, G. M., Falfari, S., Parotto, M. and Osbat, G. "Advanced Modeling of Common Rail Injector Dynamics and Comparison with Experiments", *SAE Technical Paper Series*, 2003-01-0006, 2003.
  - [18] Amiola, V., Ficarella, A., Laforgia, D., De Mattheis, S. and Genco, C. "A theoretical code to simulate the behavior of an electro-injector for diesel engines and parametric analysis", *SAE Technical Paper Series*, 970349, 1997.
  - [19] Ficarella, A., Laforgia, D. and Landriscina, V. "Evaluation of instability phenomena in a common rail injection system for high speed diesel engines", *SAE Technical Paper Series*, 1999-01-0192, 1999.
  - [20] Dongiovanni, C., Coppo, M. "Accurate Modelling of an Injector for Common Rail Systems", Fuel Injection, InTech, ISBN: 978-953-307-116-9, 2010.
  - [21] von Kunsberg Sarre, C., Kong, S-C. and Reitz, R. D. "Modeling the Effects of Injector Nozzle Geometry on Diesel Sprays", *SAE Technical Paper Series*, 1999-01-0912, 1999.
  - [22] Vass, S., Németh, H. "Sensitivity analysis of instantaneous fuel injection rate determination for detailed Diesel combustion models", *periodica polytechnica, Transportation Engineering*, vol. 41, no. 1, pp. 77-85, 2013.
  - [23] Vass S., Zöldy M. "Detailed modeling of the internal processes of an injector for Common Rail Systems", *Journal of KONES Powertrain and Transport*, vol. 25, no. 2, pp. 415-426, 2018.
  - [24] Kolade, B., Boghosian, M. E., Reddy, P.S. and Gallagher, S. "Development of a General Purpose Thermal- Hydraulic Software and its Application to Fuel Injection Systems", *SAE Technical Paper Series*, 2003-01-0702, 2003.

- 
- [25] Vass S., Németh H. “Detailed electromagnetic model of a Common Rail injector”, *34<sup>th</sup> International Colloquium on Advanced Manufacturing and Repairing Technologies in Vehicle Industry, Visegrád, Hungary*, ISBN 978-963-313-258-6, pp. 165-168., May 2017.
- [26] Bárdos, Á., Vass, S., Németh, H. “Validation of a detailed commercial vehicle turbocharged diesel engine model”, *A Jövő Járőve*, vol. 2014, no. 1-2, pp. 25-31, 2014.



## The Effect of the Electrode Position on the Dynamic Behavior of an Electrostatically Actuated Microcantilever

Mohamed Ahmed ESHAG<sup>1,2,3</sup>, Musaab ZAROG<sup>4</sup>

<sup>1</sup> School of Electrical Engineering, Southwest Jiaotong University, Chengdu, 610031, China

<sup>2</sup> School of Mechanical Engineering, Faculty of Engineering, Sudan University of Sciences and Technology, P.O. Box.407, Khartoum, Sudan

<sup>3</sup>PLOP Department, Petro-Energy E&P Co. Ltd, PDOC & PE Tower, Alsunut Area, Almogran, Khartoum, Sudan

<sup>4</sup> Department of Mechanical and Industrial Engineering, College of Engineering, Sultan Qaboos University, P.O. Box 33, Al-Khod, Muscat, 123, Oman, e-mail: musaabh@squ.edu.om

Manuscript received August 8, 2017; revised May 25, 2019

**Abstract:** Electrostatic actuators have major role in many MEMS devices, e.g. sensors, actuators. The amount of applied voltage to an electrostatic micro-actuator has a direct impact on the amplitude of deflection throughout the cantilever. This research aims to study the effect of the electrode length and the applied voltage on the amplitude of deflection of the micro-cantilever. Also, the resonant frequency for the cantilever was computed for full length and compared with simulation results. Finite element method, ANSYS was used as a simulation tool.

**Keywords:** Electrode size, finite element analysis, cantilever.

### 1. Introduction

MEMS resonators are the key players in most of the MEMS sensors and actuators. Electrostatic actuation is the most commonly used method of actuation compared to other alternative methods (e.g. electrothermal and piezoelectric), and this is mainly due to the low power consumption and ability to very high resonance frequencies [1], [2]. Electrode layers are used to apply electrostatic voltage to the actuated resonators. For the cantilever resonator a top layer of electrode is deposited. The electrode characteristics (geometrical dimensions and elastic parameters) influence the performance of the resonating structure [3]. On the other hand, the deposited electrode material might have undesirable mechanical and electronic properties compared to the resonator device. Reducing the electrode length will reduce their effect but at the same time this will affect the active area for electrostatic actuation which may require high voltage to be applied. The effect of reshaping the metal electrode as well as of changing its

thickness, on the functionality of the resonators, has been investigated in the literature [4], [5], [6] [7]. This work aims to investigate the effect of the electrode length on the amplitude of deflection of the electrostatically actuated microcantilever.

## 2. The model of the electrostatic actuator

The electrostatic actuator consists of four main parts: silicon base layer (200\*2\*20  $\mu\text{m}$ ), silicon dioxide isolator layer (50\*3\*20  $\mu\text{m}$ ), silicon actuator layer (200\*2\*20  $\mu\text{m}$ ), and copper pad layer (200\*2\*20 $\mu\text{m}$ ). The actuator was modelled in finite element software (ANSYS v.15) as shown in in *Fig. 1*. The properties of the materials used are presented in *Table.1*.

*Table.1*: Material properties

Material	Elastic module E	Poisson's ratio PR	Density D	Thermal expansion coefficient $\alpha$	Thermal conductivity k	Resistivity R
	MPa		kg/m <sup>3</sup>	1/K	W/mK	$\Omega\text{m}$
Si	$185 \cdot 10^3$	0.28	$2.3 \cdot 10^3$	$2.33 \cdot 10^{-6}$	157	$6.4 \cdot 10^2$
SiO <sub>2</sub>	$73 \cdot 10^3$	0.23	$2.27 \cdot 10^3$	$0.5 \cdot 10^{-6}$	1.4	$10 \cdot 10^8$
Cu	$110 \cdot 10^3$	0.34	$8.9 \cdot 10^3$	$16.56 \cdot 10^{-6}$	393	$1.72 \cdot 10^{-8}$

Size of element: smart sizing, number of elements=4, element type: soild227, pick under size control: global.

From *Fig. 1.c* it can be observed, that the electrostatic force is distributed over the geometry, and the base layer is fixed, while the actuator layer can move due to the actuation force.

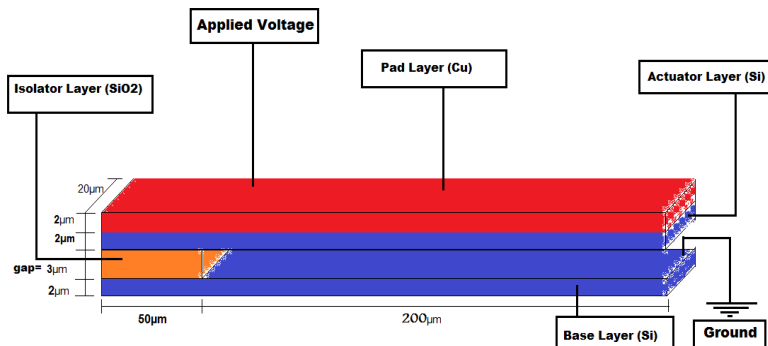


Figure 1.a: The geometry of the electrostatic microcantilever.

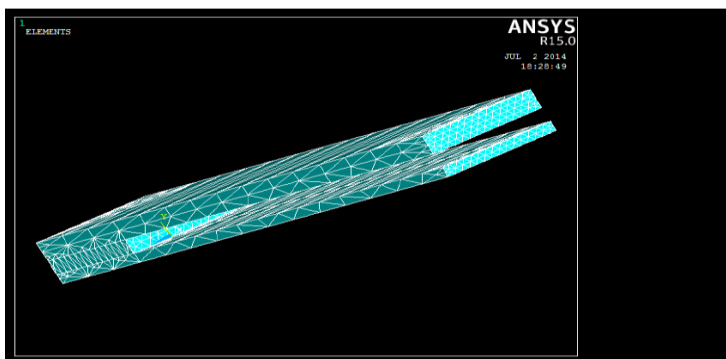


Figure 1.b: Finite element model with mesh.

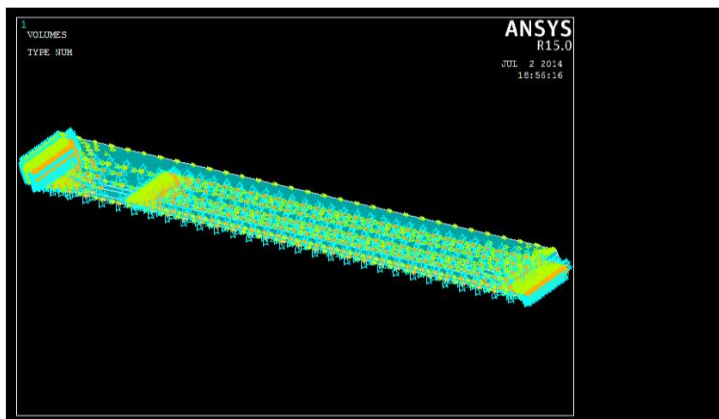


Figure 1.c: The geometry with the loading scheme.



To verify the ANSYS model, we calculated the resonance frequency and compared it with the value obtained from simulation as follows.

Firstly, we found the position of the neutral axis  $\Delta$  from the equilibrium conditions by

$$\Delta = \frac{E_1 b_1^2 - E_2 b_2^2}{2(E_1 b_1 + E_2 b_2)} = 0.254 \mu\text{m} \quad (1)$$

where  $E_1$  and  $E_2$  are the Young's moduli of the actuator layer and pad layer respectively.  $b_1$  and  $b_2$  are the thicknesses of the actuator layer and pad layer respectively as shown in Fig 2.

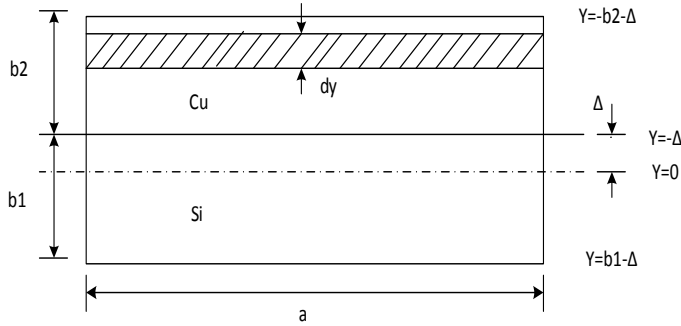


Figure 2: Microcantilever cross-section.

Subsequently, we computed the bending stiffness of the cross-section by substituting (1) in (2):

$$k = \frac{a}{3} [E_1 (b_1^3 - 3b_1^2 \Delta + 3b_1 \Delta^2) + E_2 (b_2^3 - 3b_2^2 \Delta + 3b_2 \Delta^2)] = 14971 \times 10^{-12} \text{ N.m}^2, \quad (2)$$

where  $a$  is the width of the actuator layer and of the pad layer.

Thirdly, we obtained the equivalent Young's modulus (which is valid for a homogenous cross section with identical size, that leads to the same bending stiffness) by substituting the results from (2) in (3):

$$E_{eq} = \frac{k}{y_z} = 140 \text{ GPa}, \quad (3)$$

where  $y_z = a(2b)^3/12$ .

Then, we calculated the mean mass density of the cross-section from the equality of the unit-length masses as  $A \cdot \rho_{eq} = A_1 \cdot \rho_1 + A_2 \cdot \rho_2$ , as shown below:

$$\rho_{eq} = \frac{\rho_1 b_1 + \rho_2 b_2}{b_1 + b_2} = 5600 \text{ kg / m}^3 \quad (4)$$

where  $\rho_1$  and  $\rho_2$  are the densities of the actuator layer and of the pad layer respectively.

Finally, we obtained the resonance frequency of the cross-section by substituting the results from (3) and (4) in (5):

$$f = 0.1616 \frac{t}{l^2} \sqrt{\frac{E_{eq}}{\rho_{eq}}} = 80.8 \text{ kHz} \quad (5)$$

where  $t$  is the thickness of the cross-section, and  $l$  is the length of the cantilever.

The calculated value of the resonance frequency (80.8 kHz) is close to the value obtained by ANSYS (78.12 kHz) in *Fig. 3*. This error stems from the consequence of the approximations in the numerical methods of the eigenvalue computation using FEM.

## 2. Results and discussion

A voltage of 54 mV was applied to the electrode layer (when the electrode covered 100% of the actuator layer) and the maximum deflection of the cantilever was measured as shown in *Fig. 4*. Later on, the electrode length was varied and the corresponding maximum deflection was obtained. The DMX value shown in *Fig. 4* is the maximum displacement of the tip of the cantilever (about 3  $\mu\text{m}$ ).

The applied voltage was then varied from 0 to 200 mV, while reducing the size (length) of the electrode layer from 100% (when it fully covers the actuator layer) to 10% of the actuator layer. The results are shown in *Fig. 5*. Although some of the maximum deflection values exceed the electrostatic gap value (which indicates that the actuator will hit the base layer), it is acceptable since it is not meant to mimic a real case. Alternatively, we can consider the values of deflection that are below 3  $\mu\text{m}$  or even below the pull in gap. If the geometry of the model is modified, a larger gap can be specified, and we could still obtain same relations about the effect of the electrode length. In addition, the resonance frequency of the cross-section is obtained analytically by (5) and by ANSYS as in *Fig. 3*. The errors between the calculated frequency and frequency obtained from ANSYS could be related to the meshing errors.

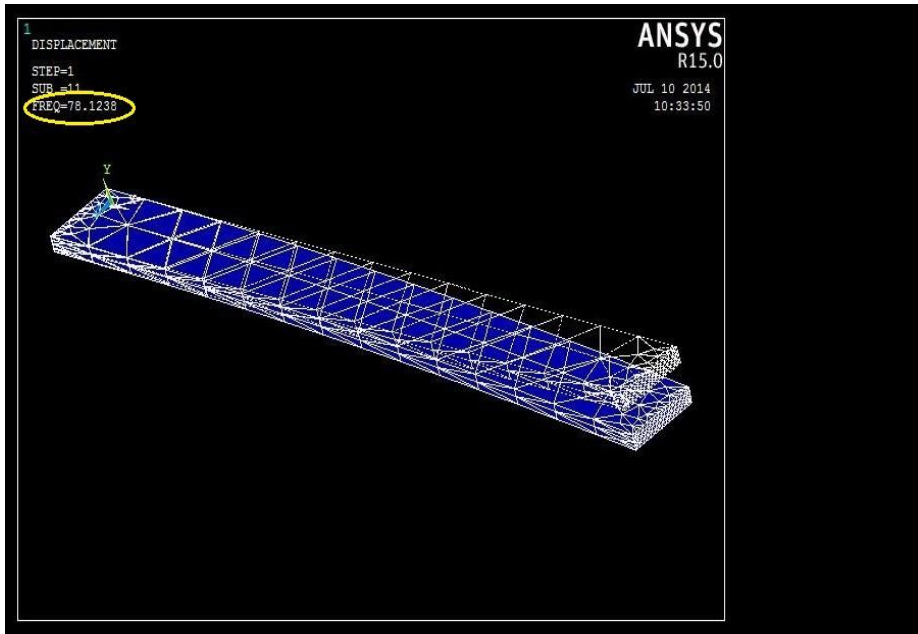


Figure 3: The first eigenmode with the highlighted resonant frequency of the cantilever.

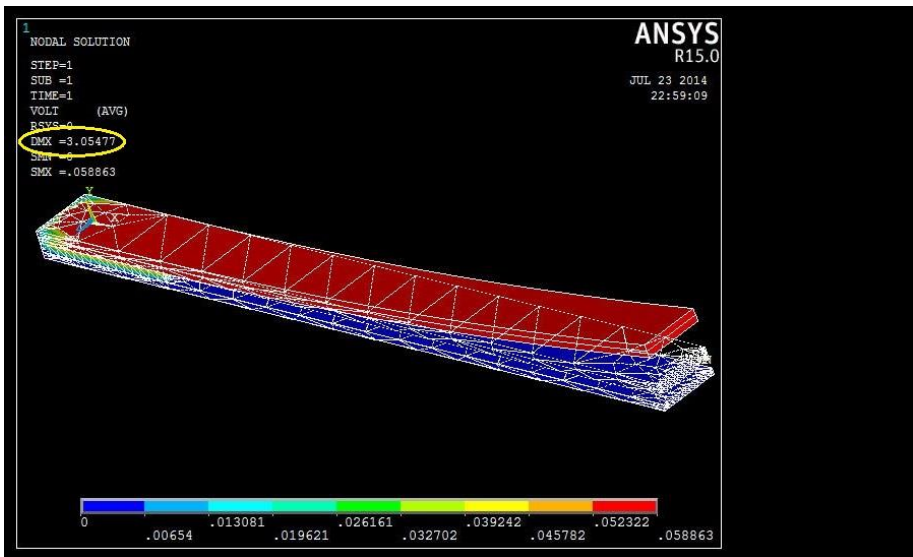


Figure 4: The electrical potential and the amplitude of deflection under applied voltage (54 mV) for 100% coverage of actuator layer.

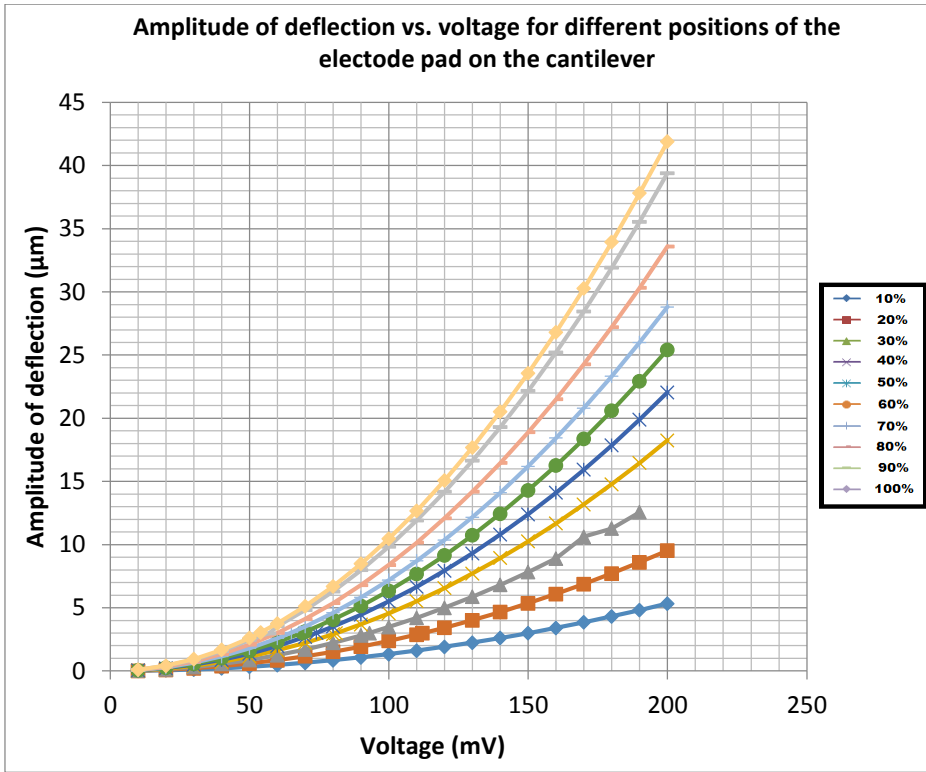


Figure 5: The amplitude of deflection vs. voltage for different positions of the electrode pad on the cantilever.

### Conclusion

The effect of the electrode’s geometrical dimensions (length) on the performance of the resonating structure was investigated. For comparison, the resonant frequency of the cantilever cross section is obtained analytically and by simulation in the case of the entirely covered cantilever. Sizing the electrode length affects the amplitude of the deflection and the voltage necessary to achieve a certain deflection level. The results show that the amplitude of deflection may decrease significantly as a result of reducing the size of the electrode. For example, at 200 mV, reducing the electrode length to one tenth reduces the amplitude of deflection almost eight times.

## References

- [1] Abdallah, A., Ishag, A., Osman, S. E., Yousif, M., and Hassan, M., "Thermal Analysis of Electrostatic Micro Actuator", *International Journal of Mechatronics, Electrical and Computer Technology*, Vol.4(10), 2014.
- [2] Atia, A., Ibrahim, M. M., Mohamed, O. A. A., and Hassan, M., "Modeling of Electrostatically Actuated Temperature Sensor", *International Conference on Computing, Electrical and Electronics Engineering*, Khartoum, 2013.
- [3] Brissaud, M., Ledren, S., and Gonnard, P. "Modelling of a cantilever non-symmetric piezoelectric bimorph", *Journal of Micromechanics and Microengineering*, 13(6), 832–844.
- [4] Kuang, J.-H., and Chen, C.-J. "The nonlinear electrostatic behavior for shaped electrode actuators" *International Journal of Mechanical Sciences*, 47(8), 1172–1190, 2005.
- [5] Yuan, Y., Du, H., Xia, X., and Wong, Y. "Analytical solutions to flexural vibration of slender piezoelectric multilayer cantilevers", *Smart Materials and Structures*, 23(9), 2014.
- [6] Lee, C.-C., Guo, Q., Cao, G. Z., and Shen, I. Y. "Effect of electrode size and silicon residue on piezoelectric thin-film membrane actuators", *Sensors and Actuators A: Physical*, 147(1), 279–285, 2008.
- [7] Ghayesh, M. H., Farokhi, H., and Alici, G. "Size-dependent electro-elasto-mechanics of MEMS with initially curved deformable electrodes", *International Journal of Mechanical Sciences*, 103, 247–264, 2015.
- [8] Maluf, N., N., Williams, K., "An Introduction to Microelectromechanical Systems Engineering, Second Edition", *Artech House, Inc.*, 2004.

## Design of a Human Knee Reeducation Mechanism

Allaoua BRAHMIA<sup>1</sup>, Ridha KELAIAIA<sup>2</sup>

<sup>1</sup> Faculté de Technologie, Université 20 Aout 1955, Skikda, Algerie,  
e-mail: a.brahmia@univ-skikda.dz

<sup>2</sup> Faculté de Technologie, Université 20 Aout 1955, Skikda, Algerie,  
e-mail: r.kelaiaia@univ-skikda.dz

Manuscript received January 21, 2019; revised July 7, 2019

**Abstract:** To establish an exercise in open muscular chain rehabilitation (OMC), it is necessary to choose the type of kinematic chain of the mechanical / biomechanical system that constitutes the lower limbs in interaction with the robotic device. Indeed, it's accepted in biomechanics that a rehabilitation exercise in OMC of the lower limb is performed with a fixed hip and a free foot. Based on these findings, a kinematic structure of a new machine, named Reeduc-Knee, is proposed, and a mechanical design is carried out. The contribution of this work is not limited to the mechanical design of the Reeduc-Knee system. Indeed, to define the minimum parameterizing defining the configuration of the device relative to an absolute reference, a geometric and kinematic study is presented.

**Keywords:** Rehabilitation robots, lower limbs, open muscle chain, kinematic chain, model geometric and kinematic.

### 1. Introduction

During the last decades, scientific research in the field of medical engineering and rehabilitation has led to important advances. Thus, rehabilitation robots have been created in order to help therapists during complex and repetitive tasks [1-3]. The robot then allows the realization of predetermined movements constituting the heart of the physical exercise to be performed. Furthermore, the use of a rehabilitation device following the appearance of the deficit allows rapid recovery of motor function. In addition, locum robotics makes it possible to facilitate notably the realization of daily tasks (demotic, chair lifts, object lifts, etc.) [4]. Moreover, the use of robotic devices has become widespread in the field of sports training. Indeed, the addition of controlled actuators makes it possible to extend the range of movements proposed in order to achieve specific objectives that cannot be achieved by conventional drive machines whose principle is limited to the displacement of a heavy load [5]. Thus, the realization of such devices

requires, in addition to the medical expertise necessary for the formalization of needs, varied knowledge from many disciplines such as: robotics, biomechanics, mechatronics, automation, and electronics. Robotics Rehabilitation and training has grown considerably in recent years. Motorized devices have been designed and are generally based on architectures similar to those of the weight machines found in the weight rooms. The definition of reference trajectories, the achievable domain or the consideration of articular biomechanics requires collaborative work between experts in the medical field and the designers of the robotic system. From the point of view of the automatic controller, the objective is to guarantee a safe operation for the user while ensuring the realization of the movements according to the performances desired by the medical profession. The automatic controller then allows the definition of control structures ensuring the stability of the controlled system during movements performed, but also allows to take into account the user's interactions with the rehabilitation device to generate physiologically consistent trajectories.

The objective of this work is therefore the design of a new device for knee rehabilitation. The adopted approach follows a process of several stages: study and definition of the objectives in terms of rehabilitation, design of the mechanical architecture, dimensioning of the actuators, and study of the control part, experimental validation and finally clinical study. Note that this entire process cannot be performed in a single job and, therefore, the last three points will be subject to further study.

## **2. Kinematic description of the movements of the knee joint**

### *A. Segments and joints of the lower limb*

The human body is considered as a set of rigid poly-articulated segments. Thus, the joints each have one or more degrees of freedom and each segment may be associated with a reference frame to position it in space. The analysis of the human movement can, by convention, be realized with respect to three planes of references, also called anatomical planes, which are the sagittal plane, the frontal/coronal plane and the transverse plane, as well as three anatomical axes, which are the sagittal axis, the transverse axis and the longitudinal axis (*Fig. 1*). The lower limb consists of three body segments: the thigh, the leg and the foot.

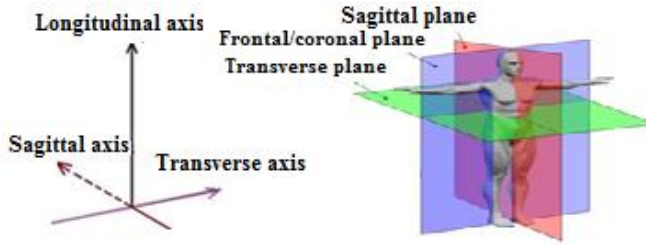


Figure 1: Anatomical planes.

### B. The knee joint

The knee is a synovial joint that joins the leg to the thigh, it is located at the lower end of the femur and the upper end of the tibia, it is a joint that supports the weight of the body. It involves three bones, the femur, the tibia and patella (Fig. 2), through three joints, the patellofemoral joint the double femoro-tibial joint.

### C. Amplitudes of the movements of the knee

The knee is the distal articulation of the thigh. It arouses the interest of the biomechanical community because of its complexity and the multiplicity of its pathologies.

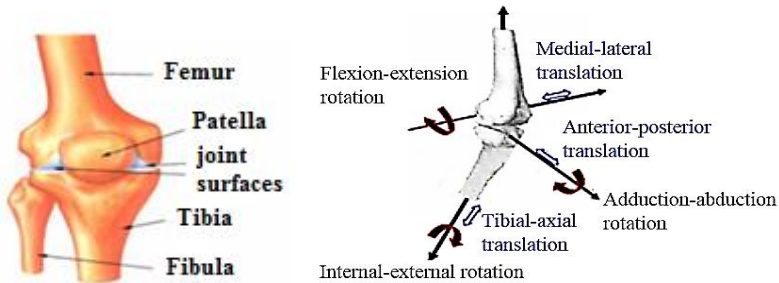


Figure 2: The knee joint [6]. Figure 3: Kinematic description of knee joint movements.

Recent studies have shown that, from an anatomical point of view, the kinematic description of the movements of the knee joint has six axes and six degrees of freedom [7]. These are presented in Fig. 3, and consist of three rotations and three translations arranged in a simple kinematic chain [8]. Note that it is commonly accepted that the amplitudes of the translational movements



are negligible vis-à-vis the amplitudes of the movements for ordinary tasks (walking, lifting chair). The amplitudes of the flexion-extension movement of the knee vary between  $0^\circ$  in hyperextension and  $150^\circ$  in hyper-flexion *Fig. 4.a* shows that knee flexion can reach  $160^\circ$  when the patient is in a squat position [9]. In addition, the internal and external rotations respectively admit maximum amplitudes of  $30^\circ$  and  $40^\circ$  (*Fig. 4.b*). Thus, in this work, a single axis of rotation will be considered [10], that is to say: the mediolateral axis around which the flexion-extension takes place.

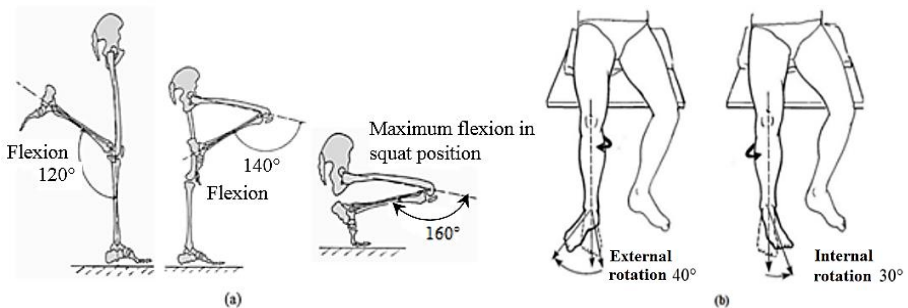


Figure 4: Amplitudes of knee movements.

### 3. Open Muscular Chain exercises (OMC)

Usually, clinicians commonly accept a definition of OMC exercise: it is an exercise of the lower limbs during which the foot is free during the movement [11]. A knee flexion-extension exercise is performed in an open muscular chain if the dynamic resultant of the force  $F_d$  opposing the movement is perpendicular to the longitudinal axis of the leg. *Fig. 5* [12] presents, in a simplified way, the knee flexion and extension movements in OMC.

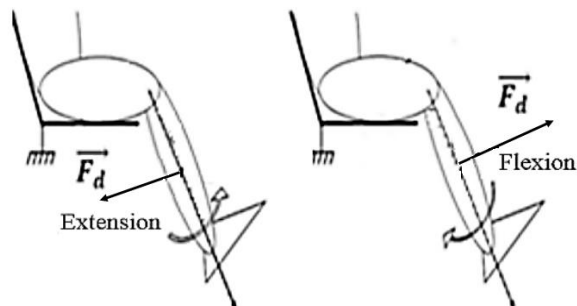


Figure 5: OMC exercises.

#### 4. Concept of the reeducation mechanism “Knee-Reeduc”

The goal of our work is to develop a machine for lower limb rehabilitation to perform open muscle chain exercises. For a device to perform this type of exercise, its kinematic structure must meet certain constraints. By analogy with robotic systems, the mechanical assembly consisting of the lower limbs and the rehabilitation device is a set of polyarticulated rigid segments. Indeed, man is often considered in biomechanics of movement as a poly-articulated and self-controlled mechanical system [13,14].

##### A. Kinematic concept

For a knee rehabilitation movement to be considered as an exercise in OMC [11], it is possible to consider that the foot must rest on a support. In order to achieve this constraint, the considered choice of the Knee-Reeduc mechanism assumes that the hip is not fixed relative to the frame and that the movement is generated by a mobile support on which the foot rests. In addition, in order to be able to develop a kinematic chain allowing OMC movement to be achieved, the mechanical assembly consisting of the lower limb must form an open kinematic chain, and the rehabilitation device chosen is formed of a closed kinematic chain (*Fig. 6.a* and *Fig. 6.b*). The kinematic design of the new device therefore amounts to defining the nature of  $L_i$  links (*Fig. 7*).

$L_1$  corresponds to the connection between the frame and the segment-thigh. The patient is seated on a seat, which is not fixed to the frame of the machine. The resulting kinematic linkage is a pivot connection corresponding to the coxo-femoral hip joint (connecting the lower limb to the hip).  $L_2$  corresponds to the knee. Let us note that only the movements of the knee along the main axis of flexion extension are sufficient for the kinematic definition of the concept Reeduc-Knee.  $L_3$  represents the connection between the mobile support and the linear module of the machine. This is done by a pivot connection.  $L_4$  corresponds to the connection between the linear module and the frame of the machine. It is characterized by a helical connection along the longitudinal axis defined by the lower limb in full extension.  $L_5$  corresponds to the connection between the moving part of the linear module with the frame. It is characterized by a slider joint.

*Fig. 7* shows the kinematic concept used for the knee rehabilitation machine in the sagittal plane. Note that here; the kinematic structure is presented for only one of the two lower limbs. Indeed, the functions of each of the lower limbs are symmetrical.

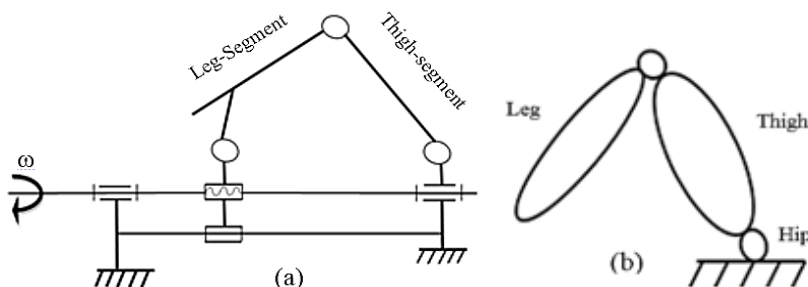


Figure 6: (a) Kinematic chain of the rehabilitation device;  
(b) Kinematic chain of lower member in OMC.

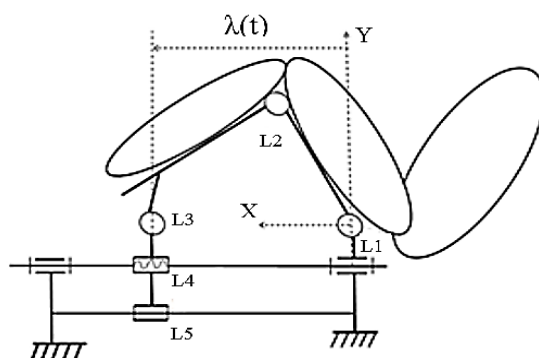


Figure 7: Kinematic concept of Knee-Reeduc in the sagittal plane.

### B. Mechanical structure

The design of the mechanical structure of Knee-Reeduc is performed in accordance with the kinematic structure proposed above. Thus, Knee-Reeduc comprises a motorized linear transfer performing the translation  $L_3$ . The latter then sets in motion a mobile support (leg-segment and thigh-segment) realizing the rotation  $L_2$  and thus allowing the flexion/extension of the foot. The thigh-segment provides the connection between the leg-segment (pivot link) and the frame through a pivot link  $L_1$ . Fig. 8 shows the type of linear transfers retained to carry out the translation  $L_5$ . The moving part of this module is set in motion by the rotation of a transmission screw  $L_4$ , the latter being actuated by a reducing motor. The design of this module is carried out for a useful run of 0.8 m to reach a wide panel of users taking into account the maximum length of the lower limb in full extension of a large patient. Finally, the linear module is mounted on a fixed platform (frame). Fig. 9 shows the mobile support (segment-leg and segment-thigh) made to support the lower limbs. The design of this support is made for a width of 0.25 m. The maximum length of this support including the

two segments is equal to 0.95 m (this length is adjustable). *Fig. 10* shows the mechanical part of the Knee-Reeduc machine as a whole.

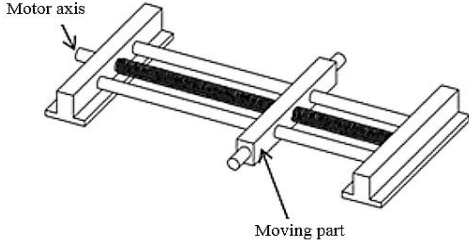


Figure 8: Linear module.

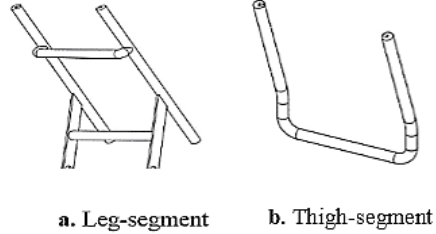


Figure 9: Mobile support.

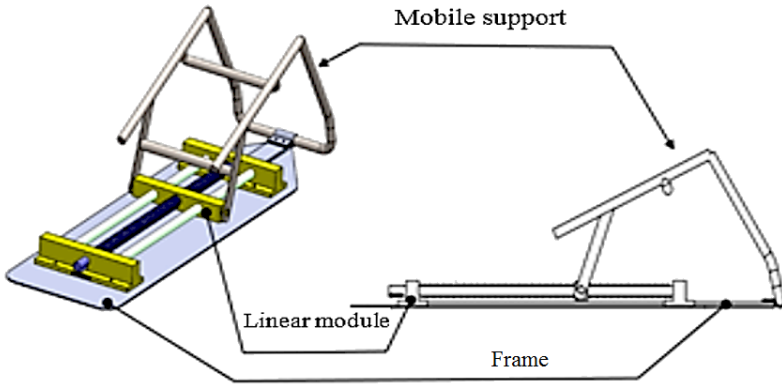


Figure 10: Mechanical part of the machine Knee-Reeduc.

### 5. Geometric and kinematic modeling of the “Knee-Reeduc” machine

The device is driven by a DC motor, which delivers a constant rotation speed  $\omega$  (control variable). A nut forming a support is driven by the transmission screw by the speed  $\omega$ , which makes it possible to move the nut by a translation speed  $VB$  (configuration variable or operational variable). The therapist needs to know the value of the flexion of the knee  $\alpha$  (the output) at each position  $\lambda$  (the entrance), for that, we have to find a relation between these quantities according to the constants of the system.

### A. Geometric model

For a geometric closure, we have:

$$\overrightarrow{OA} + \overrightarrow{AB} + \overrightarrow{BO} = \vec{0} \quad (1)$$

$$D_2 \vec{i}_1 + D_3 \vec{i}_2 - \lambda \vec{i}_3 = \vec{0} \quad (2)$$

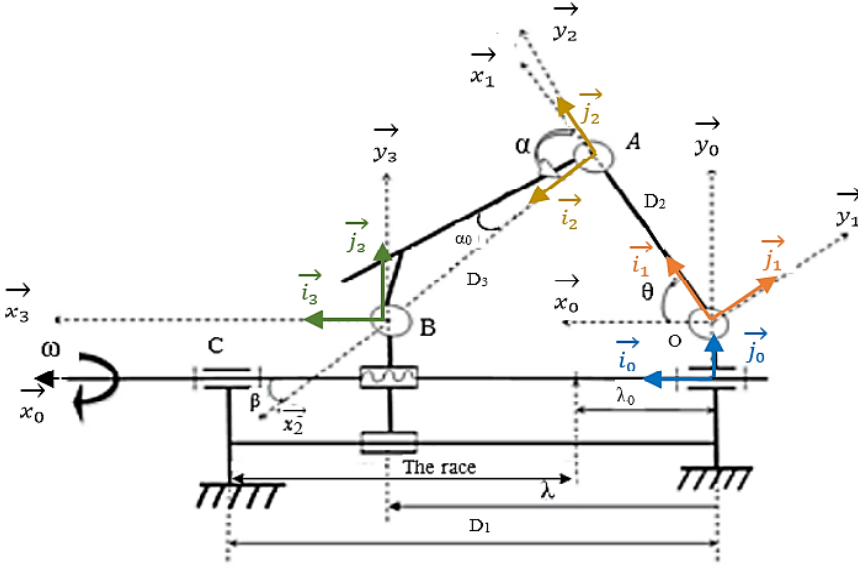


Figure 11: Mechanism of the Knee-Reeduc Device.

In (2),  $\lambda$  is the race ( $\lambda_0 \leq \lambda \leq D_1$ );

We have:

$$\vec{i}_1 = \cos \theta \vec{i}_0 + \sin \theta \vec{j}_0 \quad (3)$$

$$\vec{i}_2 = \cos \beta \vec{i}_0 - \sin \beta \vec{j}_0 \quad (4)$$

$$\vec{i}_3 = \vec{i}_0 \quad (5)$$

Replace (3), (4) and (5) in (2) we find:

$$(D_2 \cos \theta + D_3 \cos \beta - \lambda) \vec{i}_0 + (D_2 \sin \theta - D_3 \sin \beta) \vec{j}_0 = \vec{0} \quad (6)$$

Therefore, we can find this system

$$\begin{cases} D_2 \cos \theta + D_3 \cos \beta - \lambda = 0 \\ D_2 \sin \theta - D_3 \sin \beta = 0 \end{cases} \quad (7)$$

The system (7) can be written in the form

$$\begin{cases} D_2 \cos \theta + D_3 \cos \beta = \lambda \\ D_2 \sqrt{1 - \cos^2 \theta} - D_3 \sqrt{1 - \cos^2 \beta} = 0 \end{cases} \quad (8)$$

Putting  $\cos \theta = W$  and  $\cos \beta = Z$ , the system (8) becomes:

$$\begin{cases} D_2 W + D_3 Z = \lambda \\ D_2 \sqrt{1 - W^2} - D_3 \sqrt{1 - Z^2} = 0 \end{cases} \quad (9)$$

The resolution of the system (9) can give:

$$\begin{cases} W = \frac{D_2^2 - D_3^2 + \lambda^2}{2D_2\lambda} \\ Z = \frac{\lambda^2 - D_2^2 + D_3^2}{2D_3\lambda} \end{cases} \quad (10)$$

We finally find:

$$\begin{cases} \theta = \text{Arc cos } W \\ \beta = \text{Arc cos } Z \end{cases} \quad (11)$$

The angular closure allows us to write:

$$\alpha = \theta + \beta \quad (12)$$

$\alpha$ : flexion angle of the knee

*Interpretation of the geometric model:*

- If the value of  $\lambda$  is minimal ( $\lambda = \lambda_0$ ), we will have a maximum value of  $\alpha$ : equivalent to a maximum knee flexion ( $\alpha - \alpha_0 = 150^\circ$ ).
- If the value of  $\lambda$  is maximal ( $\lambda = D_l$ ), we will have a minimum value of  $\alpha$ : equivalent to a minimum knee flexion ( $\alpha - \alpha_0 = 0$ ).

### B. Kinematic model

The kinematic model consists of calculating the configuration variable (or operational variable)  $V_B$  according to the control variable  $\omega$ .

We consider that:

$$\varphi = \omega t, \quad (13)$$

where  $\varphi$  represents the angle of rotation of the screw (constant uniform rotation), and  $t$  represents the time.

We will have a uniform translation of point  $B$ .

If:

$$L_a = V_B \cdot t, \quad (14)$$

the pitch “ $S$ ” of the screw corresponds to the unit advance “ $L_a$ ”

By advancing one turn of the screw, this gives  $\varphi = 2\pi$  and  $L_a = S$ .

Therefore, we get:

$$V_B = \frac{S}{t}. \quad (15)$$

For the establishment of the inverse kinematic model, we use the relation between  $\omega$  and  $V_B$ , which is given by:

$$\omega = \frac{2\pi}{S} \cdot V_B. \quad (16)$$

To get uniform translation movement, we use the following expression:

$$\lambda = V_B \cdot t. \quad (17)$$

This equation allows us to calculate the value of the race at any moment  $t$ . This value is introduced into the system (10) to find the value of knee flexion  $\alpha$  at any moment  $t$ .

#### *Interpretation of the kinematic model:*

The velocity vector of the knee joint is none other than the derivative with respect to the time of the position vector  $\overrightarrow{OA}$ .

So:

$$\overrightarrow{V}_A = \frac{d}{dt}(\overrightarrow{OA}) \quad (18)$$

Therefore:

$$\vec{V}_A = (\dot{\lambda} + D_3 \dot{\beta} \sin \beta) \vec{x}_0 - D_3 \dot{\beta} \cos \beta \vec{y}_0 \quad (19)$$

To validate the equations of the geometric and kinematic model, a simulation in Matlab is carried out. *Fig. 12.* shows the different configurations of the Knee-Reeduc for a race of 0.7 m. *Table 1* shows the values of the flexion / extension angles for each position of the Knee-Reeduc, i.e. as a function of the  $\lambda$  stroke, for values of:  $D2 = 0.45$  m;  $D3 = 0.4$  m;  $\alpha_0 \approx 39.5^\circ$ .

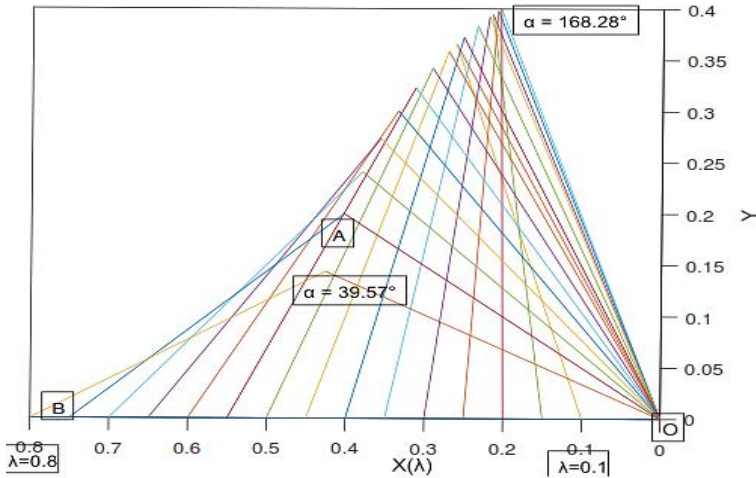


Figure 12: Knee-Reeduc Configuration for  $0,1m \leq \lambda \leq 0,8m$ .

Table 1: Values of the flexion / extension angles as a function of the race  $\lambda$

The race $\lambda$ [m]	flexion / extension angle [°]
0.1	168.284
0.2	153.615
0.3	139.195
0.4	124.228
0.5	108.200
0.6	90.397
0.7	69.257
0.8	39.571

Thus:

- the maximum flexion of the knee is:  $\alpha - \alpha_0 = 168.284 - 39.5 = 128.78^\circ$
- the minimum flexion of the knee is:  $\alpha - \alpha_0 = 39.57 - 39.5 = 0.07^\circ$ .



## 6. Conclusion

In this paper, we have presented a mechanical design of a new human knee reeducation mechanism, named Knee-Reeduc, which is consistent with a fixed hip and a free foot. First we have studied the movements of the knee joint (type, amplitudes, etc.), then we have studied the open muscular chain exercises (OMC), which allowed us to design the mechanical structure of the reeducation mechanism "Knee-Reeduc". Finally, a geometric and kinematic modeling of the developed mechanism was presented. Taking into account the generic approach followed in this design problem and based on the obtained results, future work concerns the realisation of this machine.

## References

- [1] Buchbauer, J., Steininger, K., "Techniques de renforcement musculaire en rééducation: traumatologie du sport, pathologie de l'appareil locomoteur", Edition Paris Maloine, 2003.
- [2] Moughamir, S., "Conception et développement d'une machine d'entraînement et de rééducation des membres inférieurs", Thèse de doctorat de l'université de Reims Champagne Ardenne, France, 1999.
- [3] Denève, A., "Développement et commande d'un robot pour la rééducation des membres supérieurs", Thèse de doctorat à l'université de Reims Champagne-Ardenne, 2007.
- [4] Enjalbert, M., Busnel, M., Gabus, J.C., "Robotique, domotique et handicap Rencontres en rééducation", n° 16, édition Masson, 2001.
- [5] ANAES, "Les appareils d'isocinétisme en évaluation et en rééducation musculaire: intérêt et utilisation". 113 p, 2001.
- [6] <http://www.medecine-et-sante.com/anatomie/anatgenou.html>
- [7] Riener, R., Frey, M., Bernhardt, M., Nef, T., Colombo, G., "Human centred rehabilitation robotics", in *Proc. of the IEEE International Conference in Rehabilitation Robotics*, 2005.
- [8] Seddiki, L., Guelton, K., Afilal, L., Zaytoon, J., "A 6 degrees of freedom kinematical model of the knee for the design of a new rehabilitation device", in *Proc. of the 3rd European Medical and Biological Engineering Conference EMBEC'05*, Prague, République Tchèque, n° 2134, 20-25 Novembre 2005.
- [9] Kapandji, I.A., "Physiologie articulaire. Membre inférieur: La hanche, le genou, la cheville, le pied, la voûte plantaire", Edition S.A. Maloine, 1985.
- [10] Bull, A.M.J., Amis, A.A., "Knee joint motion: Description and measurement", in *Proceedings of the Institution of Mechanical Engineers*, Part H, Journal of Engineering in Medicine, vol. 212, n° 5, 1998.
- [11] Viel, E., M. Esnault., "Récupération du sportif blessé. De la rééducation en chaîne fermée au stretching en chaîne musculaires", Edition Masson, 2003.
- [12] Seddiki, L., "Développement et commande T-S d'une machine de rééducation des membres inférieurs en chaîne musculaire fermée", Thèse de doctorat à l'université de Reims Champagne-Ardenne, France 2008.
- [13] Allard, P., Blanchi, J.P., "Analyse du mouvement humain par la biomécanique", 2ème édition, Décarie Ed., Montréal, 2000.
- [14] Winter, D.A., "Biomechanics and motor control of human movement", Wiley Inters. Publ., 2nd Ed., New York, 1990.



## An Eight-Node Hexahedral Finite Element with Rotational DOFs for Elastoplastic Applications

Ayoub AYADI<sup>1</sup>, Kamel MEFTAH<sup>1</sup>, Lakhdar SEDIRA<sup>2</sup>,  
Hossam DJAHARA<sup>1</sup>

<sup>1</sup> Laboratoire de Génie Energétique et Matériaux (LGEM), University of Biskra, BP145 RP Biskra, Algeria, e-mail: a.ayadi@univ-biskra.dz, k.meftah@univ-biskra.dz, hossam.djahara@univ-biskra.dz

<sup>2</sup> Laboratoire de Génie Mécanique (LGM), University of Biskra, BP145 RP Biskra, Algeria, e-mail: l.sedira@univ-biskra.dz

Manuscript received January 21, 2019; revised May 14, 2019.

**Abstract:** In this paper, the earlier formulation of the eight-node hexahedral SFR8 element is extended in order to analyze material nonlinearities. This element stems from the so-called Space Fiber Rotation (SFR) concept which considers virtual rotations of a nodal fiber within the element that enhances the displacement vector approximation. The resulting mathematical model of the proposed SFR8 element and the classical associative plasticity model are implemented into a Fortran calculation code to account for small strain elastoplastic problems. The performance of this element is assessed by means of a set of nonlinear benchmark problems in which the development of the plastic zone has been investigated. The accuracy of the obtained results is principally evaluated with some reference solutions.

**Keywords:** 3D finite elements, hexahedral elements, Space Fiber Rotation, elastoplasticity.

### 1. Introduction

Modeling physical phenomena leads in many cases to nonlinear problems. In structural engineering, elastoplastic analysis is important for a wide range of industrial processes and many applications might be a source of material nonlinearities. For instance, in automobile and aerospace industries, crash-worthiness is a major area of interest. Another example is metal forming processes, where tests in the design of new products are required to evaluate their performance. More recently, drop impact test of some mobile devices such as mobile phones, personal digital assistants and laptops which involve plastic deformation have been an object of research [1]. As these tests are high priced,

nonlinear finite element analysis has emerged as a viable alternative in addressing these kinds of problems. As a matter of fact, the finite element method is considered the most adopted procedure for solving elastoplastic problems [2]. Since the first published papers addressing elastoplastic problems using finite element method in the mid-1960s [3-6], the debate about accuracy and efficiency of finite elements in nonlinear structural analysis has gained fresh prominence. As a result, many shell, solid, as well as solid-shell element formulations have been developed and extended to nonlinear problems involving elastoplastic analysis. Surveys such as that conducted by Yang et al. [7] compiles the important literature on shell finite elements in both linear and nonlinear regimes. It includes several techniques to improve classical shell element efficiency as they suffer from some undesirable responses such as locking phenomenon and zero energy modes. However, the classical shell element formulations carry with them various limitations especially when information across the thickness is required as in hydroforming process and draw-bending tests [8].

To solve this problem, several shell formulations have been proposed to take the thickness stretch into consideration (see [9-11] to cite only a few). Despite these pioneering achievements, solid-shell elements have emerged as a powerful platform for modeling elastoplastic problems [12-15] as they provide many advantages with respect to shell elements such as the natural treatment of double-sided contact and the straightforward connection with solid elements. On the other hand, many solid elements have been also developed to address a large set of linear and nonlinear problems [16-18] as they offer easier formulation, in comparison with shell elements, based on three dimensional constitutive laws. May et al. [19], investigated the elastoplastic behavior of beams under pure and warping torsion using a 20-noded isoparametric brick element. In order to overcome some well-known deficiencies of the classical first-order element, including volumetric locking, Roehl and Ramm [20] developed two enhanced elements denoted by HEXA8-E3 and HEXA8-E6 based on the enhanced assumed strain concept to account for large elastoplastic analysis of solids and shells. In the same context, Liu et al. [21] suggested four-point quadrature hexahedral element in which the shear locking was avoided by means of generalized strain vector written in a local corotational system. To improve the elastoplastic analysis of irregular meshes, Cao et al. [22] proposed a brick element where a penalty term is introduced into the Hu-Washizu functional to enforce stresses to satisfy the equilibrium equations. Also, Wang and Wagoner [8] developed the so-called WW3D solid element, a mixed eight-node hexahedral element, for sheet forming analysis where the strain components corresponding to locking modes are eliminated. Recently, Artioli et al. [23] proposed a linear hexahedral element based on the assumed strain

technique. This element has its origins in the Nodally Integrated Continuum Element (NICE) formulation [24] and it was successfully implemented to solve plasticity problems.

This study aims at investigating a recently published 3D solid element performance, named SFR8, in small strain nonlinear elastoplastic problems. The element's formulation is based on the so-called Space Fiber Rotation (SFR) approach firstly proposed by Ayad [25]. This approach considers 3D rotations of a virtual fiber within the finite element that improves the displacement vector approximation. Hence, the SFR concept adds rotational DOFs along with the classical displacement ones. Ayad et al. [26] adopted the SFR concept to formulate two eight-node hexahedral elements SFR8 and SFR8I. The response of these two elements in the linear static regime was examined through a series of benchmarks where the findings show a better accuracy than the classical first order hexahedral element and close to the quadratic 20-node hexahedral element. In the same vein, the SFR concept was adopted in the works of Meftah et al. [27, 28] to develop a six-node wedge element SFR6 and a multilayered hexahedral element SFR8M. In recent developments on the SFR elements, the SFR8 and the SFR8I elements were implemented into the commercial code ABAQUS by means of the UEL interface to address nonlinear geometric problems [29]. The accuracy of the proposed elements and especially the nonconforming element SFR8I was shown to be close to that of the ABAQUS quadratic element C3D20.

The remaining part of the paper proceeds as follows. In the following section, the general formulation of the eight-node hexahedral element SFR8 is presented. Then, the constitutive model for small strain elastoplasticity is described briefly. The third section is concerned with the nonlinear finite element procedure. Finally, and before highlighting the concluding remarks, the performance of the proposed SFR8 element is assessed through a variety of nonlinear elastoplastic problems.

## 2. Kinematics of the SFR concept

This section details the formulation of the SFR8 hexahedral finite element. As shown in *Fig. 1*, this formulation is based on the so-called Space Fiber concept which considers a virtual nodal fiber within the element (fiber  $\bar{i}q$ ). This fiber rotation, defined by the rotation vector  $\bar{\theta}_i$ , develops additional displacements that enhance the classical approximation of the displacement vector. Accordingly, the final displacement field takes the following form:

$$\bar{U}_q = \sum_{i=1}^8 [N_i \bar{d}_i + f(\bar{\theta}_i, \bar{i}q)] \quad (1)$$

where  $f(\bar{\theta}_i, \bar{i}q)$  is the additional displacement vector,  $\bar{d}_i = \{U_i V_i W_i\}^T$  is the vector of nodal displacements, and  $N_i$  are the classical shape functions associated with the eight-node brick element given by:

$$N_i(\xi, \eta, \zeta) = \frac{1}{8}(1 + \xi_i \xi)(1 + \eta_i \eta)(1 + \zeta_i \zeta) \quad \text{with } -1 < \xi, \eta, \zeta < +1 \quad (2)$$

The additional displacement vector  $f(\bar{\theta}_i, \bar{i}q)$  is written as:

$$f(\bar{\theta}_i, \bar{i}q) = N_i(\bar{\theta}_i \wedge \bar{i}q) \quad (3)$$

where

$$\{i q\} = \{X_q - X_i\} = \begin{Bmatrix} X - X_i \\ Y - Y_i \\ Z - Z_i \end{Bmatrix} \quad ; \quad \{\theta_i\} = \begin{Bmatrix} \theta_{X_i} \\ \theta_{Y_i} \\ \theta_{Z_i} \end{Bmatrix} \quad (4)$$

$X$ ,  $Y$ , and  $Z$  are the global coordinates of  $q$  given by the following expressions

$$X = \sum_{i=1}^8 N_i X_i; \quad Y = \sum_{i=1}^8 N_i Y_i; \quad Z = \sum_{i=1}^8 N_i Z_i, \quad (5)$$

where  $X_i, Y_i, Z_i$  are the global coordinates of node  $i$ .

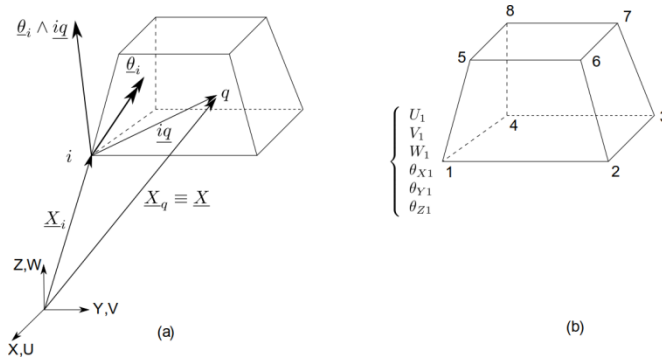


Figure 1: The SFR approach; (a) 3D rotation of the virtual fiber  $i q$  inducing an additional displacement, (b) the eight-node hexahedral element SFR8 and its nodal variables.

By performing the cross product  $\bar{\theta}_i \wedge \bar{i}q$ , we obtain the following approximation of the displacement vector (the Einstein summation convention on  $i$  is used):

$$\begin{Bmatrix} U \\ V \\ W \end{Bmatrix} = \begin{Bmatrix} N_i U_i + N_i(Z - Z_i)\theta_{Y_i} - N_i(Y - Y_i)\theta_{Z_i} \\ N_i V_i + N_i(X - X_i)\theta_{Z_i} - N_i(Z - Z_i)\theta_{X_i} \\ N_i Y_i + N_i(Y - Y_i)\theta_{Z_i} - N_i(X - X_i)\theta_{X_i} \end{Bmatrix}. \quad (6)$$

The approximation (6) can be expressed in a matrix form:

$$\{U\} = [N]\{d_n\} \quad ; \quad [N] = \begin{bmatrix} \{N_{ui}\}^T \\ \dots \\ \{N_{vi}\}^T \dots i=1,8 \\ \{N_{wi}\}^T \end{bmatrix} = \begin{bmatrix} \{N_u\}^T \\ \{N_v\}^T \\ \{N_w\}^T \end{bmatrix}, \quad (7)$$

where

$$\begin{aligned} \{N_{ui}\} &= \{N_i \ 0 \ 0 \ 0 \ N_i(Z - Z_i) \ -N_i(Y - Y_i)\}^T \\ \{N_{vi}\} &= \{N_i \ 0 \ 0 \ -N_i(Z - Z_i) \ 0 \ N_i(X - X_i)\}^T \\ \{N_{wi}\} &= \{N_i \ 0 \ 0 \ 0 \ N_i(Y - Y_i) \ -N_i(X - X_i)\}^T \end{aligned} \quad (8)$$

$$\text{and} \quad \{d_n\} = \{\dots | U_i \ V_i \ W_i \ \dots \ \theta_{X_i} \ \theta_{Y_i} \ \theta_{Z_i} | \dots i=1,8\}^T \quad (9)$$

is the global displacement vector of the SFR8 element.

### 3. Constitutive equation for rate independent elastoplasticity

After initial yielding, the total strain is made up additively of an elastic component  $\varepsilon^e$  and a plastic component  $\varepsilon^p$  so that:

$$\varepsilon_{ij} = (\varepsilon_{ij})^e + (\varepsilon_{ij})^p. \quad (10)$$

The elastic part of strain field is linked to stress field though the relation:

$$\sigma_{ij} = D_{ijkl}^e (\varepsilon_{kl} - \varepsilon_{kl}^p), \quad (11)$$

where  $D_{ijkl}^e$  is the tensor of elastic constants which for an isotropic material may be formulated as:

$$D_{ijkl}^e = G \left( \frac{2\nu}{1-2\nu} \delta_{ij} \delta_{kl} + \delta_{ik} \delta_{jl} + \delta_{il} \delta_{jk} \right), \quad (12)$$

in which  $G$  is the shear modulus;  $\nu$  is Poisson's ration and  $\delta_{ij}$  represents the Kronecker delta.

In this paper, the elastoplastic constitutive model based on the von Mises associated yield criterion is adopted. Therefore, the following yield function is considered.

$$f = \sigma_e - \sigma_y(\varepsilon^p) \leq 0, \quad (13)$$

where  $\sigma_e$  is the von Mises effective stress and  $\sigma_y$  is the yield stress which can be described by a nonlinear function of the equivalent plastic strain  $\varepsilon^p$ .

The plastic part of strain  $\varepsilon_{ij}^p$  is only defined by its increment  $d\varepsilon_{ij}^p$  which, by using the normality flow rule, is given by:

$$d\varepsilon_{ij}^p = \bar{\lambda} \frac{\partial f}{\partial \sigma_{ij}} = \bar{\lambda} P, \quad (14)$$

where  $\bar{\lambda}$  is a scalar function called the plastic multiplier, which determines the magnitude of plastic flow and  $P$  represents the direction of plastic strain rate.

Differentiation of (11) with respect to virtual time and combination of the result with Eq.14 and using the consistency condition  $df = 0$ , the plastic multiplier  $\bar{\lambda}$  can be elaborated as:

$$\bar{\lambda} = \frac{(\partial f / \partial \sigma_{ij}) D_{ijkl}^e d\varepsilon_{ij}}{(\partial f / \partial \sigma_{rs}) D_{rstu}^e (\partial f / \partial \sigma_{tu}) + H_y}, \quad (15)$$

where  $H_y$  is the hardening moduli involved in the evolution laws describing the isotropic hardening.

By substituting the expression of the plastic multiplier  $\bar{\lambda}$  into Eq. 11, the elastoplastic tangent modulus is derived as:

$$D_{ijkl}^{ep} = D_{ijkl}^e - \gamma \frac{D_{ijmn}^e (\partial f / \partial \sigma_{mn}) (\partial f / \partial \sigma_{pq}) D_{pqkl}^e}{(\partial f / \partial \sigma_{rs}) D_{rstu}^e (\partial f / \partial \sigma_{tu}) + H_y}, \quad (16)$$

where  $\gamma = 0$  for elastic loading/unloading, and  $\gamma = 1$  for strict loading.

Finally, the complete elastoplastic stress strain relation can be expressed:

$$\sigma_{ij} = D_{ijkl}^{ep} \varepsilon_{kl}. \quad (17)$$

#### 4. Numerical implementation

In order to solve the above nonlinear system, a two-step algorithm based on the state update procedure is adopted [30, 31]. The steps of the algorithm are:

1. Perform a predictor step in which we assume that the step  $(t_n, t_{n+1})$  is elastic. Accordingly:

$$\varepsilon_{n+1}^{trial} = \varepsilon_n^e + \Delta\varepsilon \quad (18)$$

The corresponding trial stress is given by:

$$\sigma_{n+1}^{trial} = D(\varepsilon_{n+1} - \varepsilon_n^p) \quad (19)$$

## 2. Evaluation of the yield function

If  $f(\sigma_{n+1}^{trial}, H_y) \leq 0$ , the stress lies within the yield surface and the trial state represents the actual final state of the material. Accordingly:

$$(\bullet)_{n+1} = (\bullet)_{n+1}^{trial} \quad (20)$$

If  $f(\sigma_{n+1}^{trial}, H_y) \geq 0$ , the elastic trial state is not plastically admissible and the consistency condition is violated. Therefore, a plastic corrector step (or return mapping algorithm) is required.

An outline of the numerical procedure is provided in *Fig. 2*.

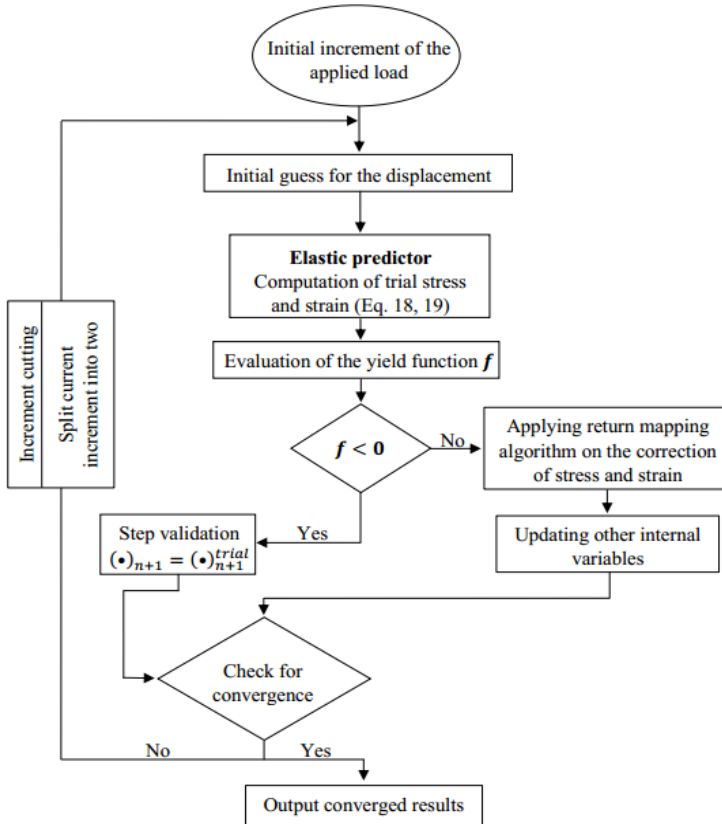


Figure 2: Flowchart of the numerical procedure.

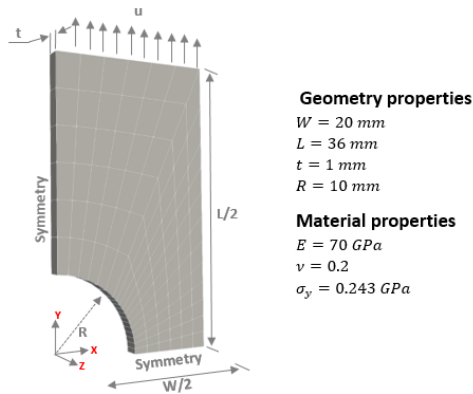


## 5. Numerical examples

The proposed SFR8 element is implemented into HYPLAS software, a FORTRAN Finite Element code developed by de Souza Neto et al. [2] to account for hyperelastic and elastoplastic analysis. The performance of the SFR8 element, for elastoplastic problems, is evaluated with known benchmarks. The obtained results are compared with the ABAQUS Hybrid element C3D8H, the second-order ABAQUS hexahedral element C3D20, the NICE-H8 element developed by Artioli [23] and the standard hexahedral element H8.

### 5.1 Stretched perforated rectangular plate

In this example, a rectangular perforated plate subjected to longitudinal stretching is considered. This problem is frequently used as a benchmark to assess the precision and the effectiveness of the plasticity model as well as the adopted numerical technique. Material properties, geometric dimensions, boundary conditions and the finite element mesh of this example are all summarized in *Fig. 3*.



*Figure 3:* Stretched perforated plate: Geometry, FEM mesh and material properties.

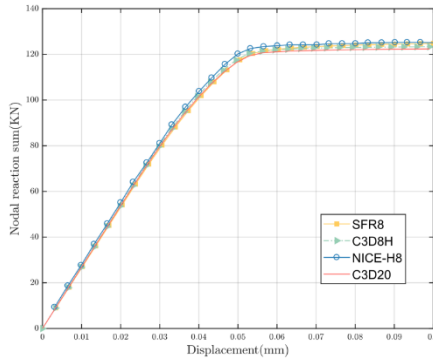


Figure 4: Stretched perforated plate: Reaction-displacement diagram.

A total displacement of 10 mm is applied on the upper edge of the plate. The final load is reached by performing 30 equal steps where the material is considered elastic perfectly plastic and the von Mises model is adopted. Fig.4 shows the load deflection curve where the total reaction force at the bottom surface of the plate is plotted against the applied displacement. The results obtained by the SFR8 element are compared with some reference elements from the literature. The good agreement between the SFR8 element and the reference solutions is noticeable.

The evolution of the plastic strain is illustrated in Fig.5. Note that the first yielding is observed at the intersection of the Y-Symmetry plan and the edge of the hole where the plastic region extends in an oblique front along the entire cross section of the stretched plate.

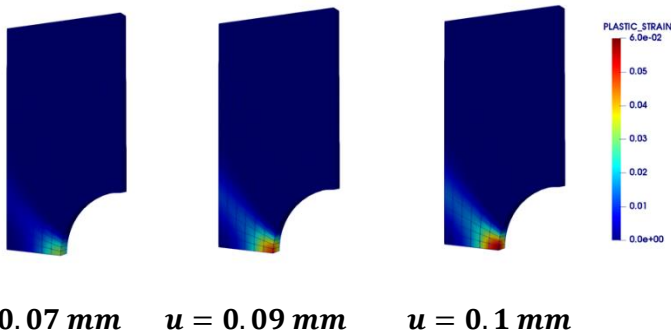
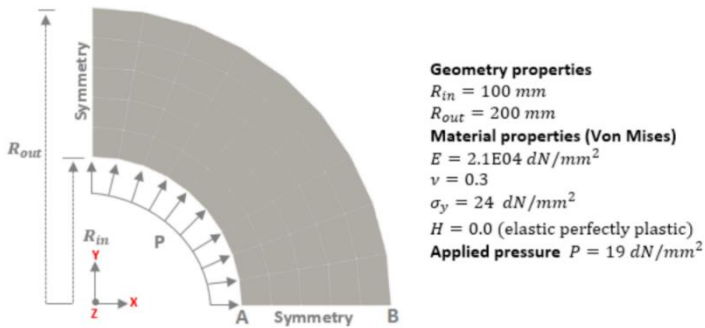


Figure 5: Stretched perforated plate: Equivalent plastic strain at different stages of the prescribed displacement.

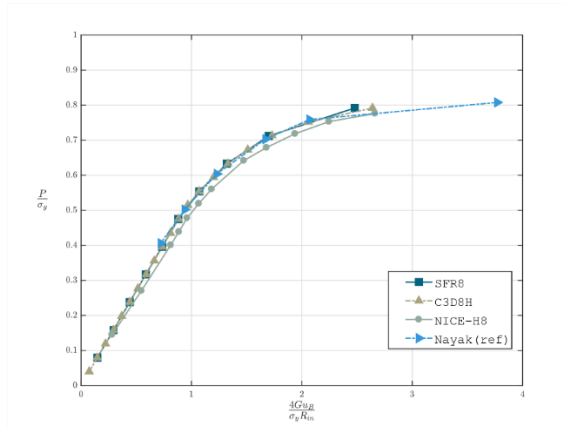
## 5.2 Thick walled cylinder subjected to internal pressure

The second numerical example is illustrated in *Fig. 6*. This problem consists of an infinitely long, thick cylinder subjected to a gradually increasing internal pressure. This benchmark test has been studied by several authors [23, 32].



*Figure 6:* Thick cylinder: Geometry, Material properties and FE mesh.

Considering an elastic perfectly plastic material, the cylinder is assumed to have the properties shown in *Fig. 6*. Like the first example, only one quarter of the cylinder is considered where the boundary condition is assumed according to a plane strain condition assumed along the axis of the thick cylinder. The load is applied according to an incremental scheme of 10 equal steps.



*Figure 7:* Thick walled cylinder: Pressure-displacement curve.

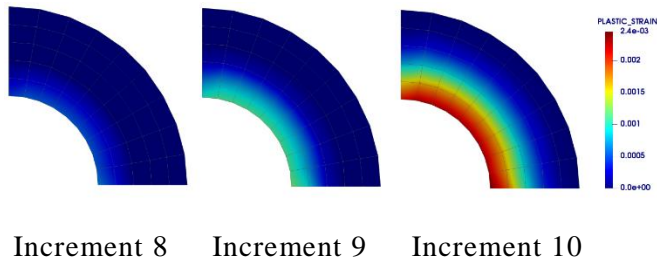


Figure 8: Thick walled cylinder: Evolution of the plastic deformation.

The pressure-displacement curve at point B is depicted in Fig. 7 ( $G$  represents the shear modulus). The results obtained by the SFR8 element are compared with those given by ABAQUS as well as with the analytical solution taken from Nayak et al. [32]. It can be seen that the SFR8 element shows a good agreement with C3D8H, NICE-H8 element and the reference solution [32]. The evolution of the equivalent plastic strain is also illustrated in Fig.7. The plastic deformation starts at the inner surface and extends along the radius where it reaches a maximum of  $\varepsilon_{Pmax}^{SFR8} = 0.0024$ . When compared to ABAQUS results ( $\varepsilon_{Pmax}^{C3D8H} = 0.002429$ ), the results are almost the same.

## 6. Conclusion

This work was designed to evaluate the performance of the SFR8 hexahedral element for small strain elastoplasticity analysis. The element formulation relies on the consideration of virtual rotations of a nodal fiber within the element that improves the displacement vector approximation. The adopted constitutive model is the classical associative von Mises plasticity model where the Newton-Raphson scheme has been implemented for solving the nonlinear numerical system. The element shows reliability and robustness when compared with some reference elements from the literature.

## References

- [1] Che, F. X., and Pang, J. H. "Study on Board-Level Drop Impact Reliability of Sn–Ag–Cu Solder Joint by Considering Strain Rate Dependent Properties of Solder", *IEEE Transactions on Device and Materials Reliability*, vol. 15, no. 2, pp. 181-190, 2015.
- [2] de Souza Neto, E. A., Peric, D., & Owen, D. R., "Computational methods for plasticity: theory and applications", John Wiley & Sons, 2011.
- [3] Pope, G. G., "A discrete element method for the analysis of plane elasto-plastic stress problems", *The Aeronautical Quarterly*, vol. 17, no. 1, pp. 83-104, 1966.
- [4] Marcal, P. V., & King, I. P., "Elastic-plastic analysis of two-dimensional stress systems by the finite element method", *International Journal of Mechanical Sciences*, vol. 9, no. 3, pp. 143-155, 1967.

- 
- [5] Yamada, Y., Yoshimura, N., & Sakurai, T., "Plastic stress-strain matrix and its application for the solution of elastic-plastic problems by the finite element method", *International Journal of Mechanical Sciences*, vol. 10, no. 5, pp. 343-354, 1968.
- [6] Oden, J. T., "Finite element applications in nonlinear structural analysis", in *Proceedings of the ASCE Symposium on Application of Finite Element Methods in Civil Engineering*, Vanderbilt University, 1969, pp. 419-456.
- [7] Yang, H. T., Saigal, S., Masud, A., & Kapania, R. K., "A survey of recent shell finite elements", *International Journal for numerical methods in engineering*, vol. 47, no. 1-3, pp. 101-127, 2000.
- [8] Wang, J., & Wagoner, R. H., "A practical large-strain solid finite element for sheet forming", *International journal for numerical methods in engineering*, vol. 63, no. 4, pp. 473-501, 2005.
- [9] Brank, B., Korelc, J., & Ibrahimbegović, A., "Nonlinear shell problem formulation accounting for through-the-thickness stretching and its finite element implementation", *Computers & structures*, vol. 80, no. 9-10, pp. 699-717, 2002.
- [10] Cardoso, R. P., & Yoon, J. W., "One point quadrature shell element with through-thickness stretch" *Computer Methods in Applied Mechanics and Engineering*, vol. 194, no. 9-11, pp. 1161-1199, 2005.
- [11] Klinkel, S., Gruttmann, F., & Wagner, W., "A mixed shell formulation accounting for thickness strains and finite strain 3D material models", *International journal for numerical methods in engineering*, vol. 74, no. 6, pp. 945-970, 2008.
- [12] Legay, A., & Combescure, A., "Elastoplastic stability analysis of shells using the physically stabilized finite element SHB8PS", *International Journal for Numerical Methods in Engineering*, vol. 57, no. 9, pp. 1299-1322, 2003.
- [13] Abed-Meraim, F., and Combescure, A., "An improved assumed strain solid-shell element formulation with physical stabilization for geometric non-linear applications and elastic-plastic stability analysis", *International Journal for Numerical Methods in Engineering*, vol. 80, no. 13, pp. 1640-1686, 2009.
- [14] Schwarze, M., Vladimirov, I. N., & Reese, S., "Sheet metal forming and springback simulation by means of a new reduced integration solid-shell finite element technology", *Computer Methods in Applied Mechanics and Engineering*, vol. 200, no. 5-8, pp. 454-476, 2011.
- [15] Wang, P., Chalal, H., & Abed-Meraim, F., "Quadratic solid-shell elements for nonlinear structural analysis and sheet metal forming simulation", *Computational Mechanics*, vol. 59, no. 1, pp. 161-186, 2017.
- [16] Mackerle, J., "Finite element linear and nonlinear, static and dynamic analysis of structural elements: a bibliography (1992-1995)", *Engineering Computations*, vol. 14, no. 4, pp. 347-440, 1997.
- [17] Mackerle, J., "Finite element linear and nonlinear, static and dynamic analysis of structural elements—an addendum—A bibliography (1996-1999)", *Engineering computations*, vol. 17, no. 3, pp. 274-351, 2000.
- [18] Mackerle, J., "Finite element linear and nonlinear, static and dynamic analysis of structural elements, an addendum: A bibliography (1999–2002)", *Engineering Computations*, vol. 19, no. 5, pp. 520-594, 2002.
- [19] May, I. M., & Al-Shaarbaf, I. A. S., "Elasto-plastic analysis of torsion using a three-dimensional finite element model", *Computers & structures*, vol. 33, no. 3, pp. 667-678, 1989.
- [20] Roehl, D., & Ramm, E., "Large elasto-plastic finite element analysis of solids and shells with the enhanced assumed strain concept", *International Journal of Solids and Structures*, vol. 33, no. 20-22, pp. 3215-3237, 1996.

- 
- [21] Liu, W. K., Guo, Y., Tang, S., & Belytschko, T., "A multiple-quadrature eight-node hexahedral finite element for large deformation elastoplastic analysis", *Computer Methods in Applied Mechanics and Engineering*, vol. 154, no. 1-2, pp. 69-132, 1998.
- [22] Cao, Y. P., Hu, N., Fukunaga, H., Lu, J., & Yao, Z. H., "A highly accurate brick element based on a three-field variational principle for elasto-plastic analysis", *Finite elements in analysis and design*, vol. 39, no. 12, pp. 1155-1171, 2003.
- [23] Artioli, E., Castellazzi, G., & Krysl, P., "Assumed strain nodally integrated hexahedral finite element formulation for elastoplastic applications", *International Journal for Numerical Methods in Engineering*, vol. 99, no. 11, pp. 844-866, 2014.
- [24] Krysl, P., & Zhu, B., "Locking-free continuum displacement finite elements with nodal integration", *International Journal for Numerical Methods in Engineering*, vol. 76, no. 7, pp. 1020-1043, 2008.
- [25] Ayad, R., "Contribution to the numerical modeling of solids and structures and the non-Newtonian fluids forming process: Application to packaging materials", Habilitation to conduct researches, University of Reims, 2002.
- [26] Ayad, R., Zouari, W., Meftah, K., Zineb, T. B., & Benjeddou, A., "Enrichment of linear hexahedral finite elements using rotations of a virtual space fiber", *International Journal for Numerical Methods in Engineering*, vol. 95, no. 1, pp. 46-70, 2013.
- [27] Meftah, K., Ayad, R., & Hecini, M., "A new 3D 6-node solid finite element based upon the Space Fibre Rotation concept", *European Journal of Computational Mechanics/Revue Européenne de Mécanique Numérique*, vol. 22, no. 1, pp. 1-29, 2013.
- [28] Meftah, K., Sedira, L., Zouari, W., Ayad, R., & Hecini, M., "A multilayered 3D hexahedral finite element with rotational DOFs", *European Journal of Computational Mechanics*, vol. 24, no. 3, pp. 107-128, 2015.
- [29] Meftah, K., Zouari, W., Sedira, L., and Ayad, R., "Geometric non-linear hexahedral elements with rotational DOFs", *Computational Mechanics*, vol. 57, no. 1, pp. 37-53, 2016.
- [30] Simo, J. C., and Taylor, R. L., "Consistent tangent operators for rate-independent elastoplasticity", *Computer methods in applied mechanics and engineering*, vol. 48, no. 1, pp. 101-118, 1985.
- [31] Simo, J. C., and Taylor, R. L., "A return mapping algorithm for plane stress elastoplasticity", *International Journal for Numerical Methods in Engineering*, vol. 22, no. 3, pp. 649-670, 1986.
- [32] Nayak, G. C., & Zienkiewicz, O. C., "Elasto-plastic stress analysis. A generalization for various constitutive relations including strain softening", *International Journal for Numerical Methods in Engineering*, vol. 5, no. 1, pp. 113-135, 1972.
- [33] Peng, Q., and Chen, M. X., "An efficient return mapping algorithm for general isotropic elastoplasticity in principal space", *Computers & Structures*, vol. 92, pp. 173-184, 2012.
- [34] Owen, D. R. J., and Hinton, E., "Finite elements in plasticity", Pineridge press, 1980.



## A Four-Node Tetrahedral Finite Element Based on Space Fiber Rotation Concept

Kamel MEFTAH<sup>1</sup>, Lakhdar SEDIRA<sup>2</sup>

<sup>1</sup>University of Biskra, Laboratoire de Génie Énergétique et Matériaux, LGEM, Faculty of Sciences and Technology, Biskra, 07000, Algeria, e-mail: k.meftah@univ-biskra.dz

<sup>2</sup>University of Biskra, Laboratoire de Génie Mécanique, LGM, Faculty of Sciences and Technology, Biskra, 07000, Algeria, e-mail: l.sedira@univ-biskra.dz

Manuscript received August 23, 2019; revised September 19, 2019

**Abstract:** The paper presents a four-node tetrahedral solid finite element SFR4 with rotational degrees of freedom (DOFs) based on the Space Fiber Rotation (SFR) concept for modeling three-dimensional solid structures. This SFR concept is based on the idea that a 3D virtual fiber, after a spatial rotation, introduces an enhancement of the strain field tensor approximation. Full numerical integration is used to evaluate the element stiffness matrix. To demonstrate the efficiency and accuracy of the developed four-node tetrahedron solid element and to compare its performance with the classical four-node tetrahedral element, extensive numerical studies are presented.

**Keywords:** Four-node tetrahedral element, 3D finite element, Space Fiber Rotation concept, rotational DOFs.

### 1. Introduction

Three types of solid elements are commonly used in modeling three-dimensional solid structures: tetrahedron, hexahedron (also known as brick) and prism (also known wedge or pentahedron) elements. Because of their suitability for arbitrary complex geometries and fully automatic mesh generations, the use of tetrahedral elements becomes practically unavoidable in complex finite element structural analyses. Over the past two decades, there had been a revival of interest in the tetrahedral solid elements possessing rotational degrees of freedom (DOFs), to improve the computational efficiency of the standard first-order elements. Various formulations have been used for the development of tetrahedral finite elements with rotational degrees of freedom. One of the first achievements in this direction was due to Pawlak et al. [1] in the development of the 4-node tetrahedral element, including translations and rotations as nodal

DOFs for 3D elasticity problems. In the work of Sze and Pan [2], a hybrid stress tetrahedron element with Allmans rotation DOFs is developed. Stabilization techniques are used to control the spurious modes by the four skew symmetric stress modes. It is interesting to note that the advanced 4-node elements with only corner nodes and rotational DOFs are obtained from that a subparametric 10-node tetrahedron element. Another simple approach to construct a 4-node tetrahedron element with rotational DOFs has been proposed by Matsubara et al. [3]. Working along the lines of rotational DOFs framework, Tian and Yagawa [4] developed a 4-node quadratic tetrahedron element with four corner nodes using the generalized node following the idea of the partition-of-unity-based finite element approximation. Later, Tian et al. [5] published the work on advanced 4-node tetrahedron elements using vertex rotational DOFs. It is noteworthy that the accuracy of their solid elements is significantly better than the accuracy of the classical first-order elements and globally close to that of the classical quadratic elements. A description of other available theories can be found, for example, in the review article by Tian et al. [6]. Also, in Reference [7] various elements are described that add rotational degrees of freedom to a four-node tetrahedron with the rotational formulation generally based on assumed strains or displacement gradients of a ten node tetrahedron.

The so-called Space Fiber Rotation (SFR) concept was firstly introduced by Ayad [8] and later by Meftah [9] to enhance the accuracy of first-order finite elements. This SFR concept was then adapted to 3D elastic structures by Meftah et al. [10] by developing a 3D six-node prismatic solid element, named SFR6, and by Ayad et al. [11] by introducing two 3D eight-node hexahedral solid elements named SFR8 and SFR8I (with incompatible mode). One would like to recall that the present concept was firstly derived from 2D and extended later for 3D virtual rotations of a nodal fiber that improves the approximation of the displacement vector. These SFR concept-based solid elements present three rotational and three translational DOFs per node. Furthermore, in the work of Meftah et al. [12], an extension of the SFR eight-node hexahedral elements SFR8 and SFR8I, was proposed to account for geometrically nonlinear problems. Moreover, Meftah et al. [13] developed a multilayered extension of the eight-node hexahedral element named SFR8M to study composite laminate structures. In particular, it was shown that these 3D SFR solid elements yield results that are significantly better than those of the classical first-order wedge and hexahedral elements and globally close to those of the classical quadratic elements. It should be noted that the SFR solid elements maintain a good performance especially for coarse and distorted meshes [9-14].

In this work, we present a four-node tetrahedral solid finite element SFR4 to study full three-dimensional solid structures. Hence, the element has six DOFs per node, i.e. three displacements and three rotational parameters. The proposed



tetrahedral element is developed by exploiting the concept of Space Fiber Rotation. These terms, represented by the fictitious rotational degrees of freedom, would result in the creation of an interesting added value by providing a reliable and accurate solution. The intent is to introduce a four-node tetrahedral element that is computationally attractive when compared with the classical four-node tetrahedral element with translations only as DOFs. This element uses an exact integration scheme with four-point rule. Their performances are investigated by studying several solid structures.

## 2. The SFR concept finite element approximation

The SFR concept is based on the space rotation of a virtual fiber. *Fig. 1* shows the geometry of the four-node tetrahedral element, in which a virtual space fiber  $\underline{i}q$  is incorporated at the nodal level. The fiber rotation, represented by the rotation vector  $\underline{\theta}$ , will generate an additional displacement vector that would enrich the classical displacement field  $\underline{U}_q$  of point  $q$ , used to formulate the standard 4-node solid tetrahedral element [10, 11].

$$\underline{U}(\xi, \eta, \zeta) = \sum_{i=1}^4 N_i(\xi, \eta, \zeta) (\underline{U}_i + \underline{\theta}_i \wedge \underline{i}q); \quad \underline{U}_q \equiv \underline{U}, \quad (1)$$

where  $\{\underline{U}_i\} = \{U_i, V_i, W_i\}^T$  is the nodal displacement vector and  $N_i$  are the classical interpolation functions associated with the classical four-node tetrahedral element given by:

$$[N] = [1 - \xi - \eta - \zeta \quad \xi \quad \eta \quad \zeta], \quad (2)$$

where  $\xi$ ,  $\eta$  and  $\zeta \in [0, 1]$  with  $1 - \xi - \eta - \zeta \geq 0$ .

In addition

$$\{\underline{i}q\} = \begin{Bmatrix} x - x_i \\ y - y_i \\ z - z_i \end{Bmatrix}; \quad \{\underline{\theta}_i\} = \begin{Bmatrix} \theta_{xi} \\ \theta_{yi} \\ \theta_{zi} \end{Bmatrix}, \quad (3)$$

where  $(x_i, y_i, z_i)$  are the Cartesian coordinates of node  $i$ , and  $(x, y, z)$  are the Cartesian coordinates of any point  $q$  of the element SFR4 given by the following approximations:

$$x = \sum_{i=1}^4 N_i x_i; \quad y = \sum_{i=1}^4 N_i y_i; \quad z = \sum_{i=1}^4 N_i z_i. \quad (4)$$

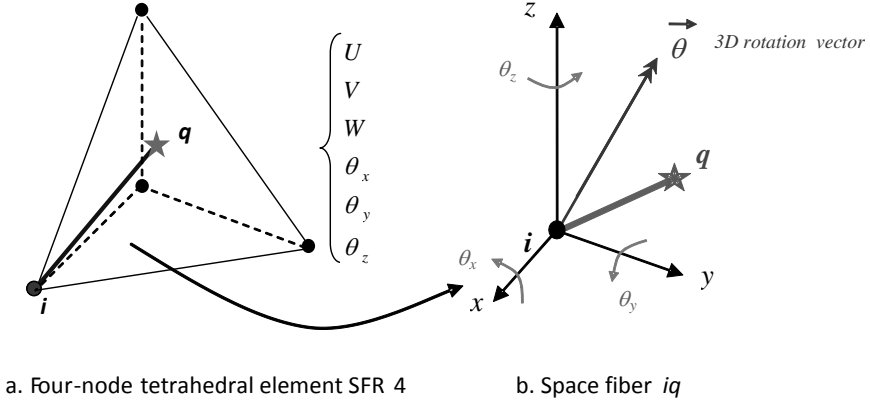


Figure 1: Geometry and kinematics of a virtual space fiber (SFR approach).

By performing the vector product  $\underline{\theta}_i \wedge \underline{i}q$ , we obtain the following approximation:

$$\{U\} = [N]\{U_n^e\}; [N] = \begin{bmatrix} \dots & [N_{Ui}] & \dots \\ \dots & [N_{Vi}] & \dots \\ \dots & [N_{Wi}] & \dots \end{bmatrix}; i = 1, \dots, 4, \quad (5)$$

where

$$\begin{aligned} [N_{Ui}] &= [N_i \quad 0 \quad 0 \quad 0 \quad N_i(z-z_i) \quad -N_i(y-y_i)] \\ [N_{Vi}] &= [0 \quad N_i \quad 0 \quad -N_i(z-z_i) \quad 0 \quad N_i(x-x_i)] \\ [N_{Wi}] &= [0 \quad 0 \quad N_i \quad N_i(y-y_i) \quad -N_i(x-x_i) \quad 0] \end{aligned} \quad (6)$$

and

$$\{u_n^e\} = \{\dots U_i \quad V_i \quad W_i \quad \theta_{xi} \quad \theta_{yi} \quad \theta_{zi} \quad \dots\}^T; i = 1, \dots, 4 \quad (7)$$

is the nodal degrees of freedom vector of SFR4 element containing three translational and three fictive rotational DOFs per node, see Fig. 1(a) [10], [11].

The strain tensor of any point  $q$  is classically defined in the global coordinate system by:

$$\varepsilon_{xx} = U_{,x}; \varepsilon_{yy} = V_{,y}; \varepsilon_{zz} = W_{,z}; \gamma_{xy} = 2\varepsilon_{xy} = U_{,y} + V_{,x} \quad (8.a)$$

$$\gamma_{xz} = 2\varepsilon_{xz} = U_{,z} + W_{,x}; \gamma_{yz} = 2\varepsilon_{yz} = V_{,z} + W_{,y}. \quad (8.b)$$

Using expressions Eq. (8) of the mechanical strains and the approximation Eq. (5) of the displacement vector, we obtain a matrix relationship between the strain vector  $\{\varepsilon\}$  and the nodal degrees of freedom vector  $\{U_n\}$ :

$$\{\varepsilon\} = [B]\{U_n\}; \quad [B] = \begin{matrix} & \begin{matrix} \{N_{U,x}\}^T \\ \{N_{V,y}\}^T \\ \{N_{W,z}\}^T \end{matrix} \\ \begin{matrix} \{N_{U,y}\}^T + \{N_{V,x}\}^T \\ \{N_{U,z}\}^T + \{N_{W,x}\}^T \\ \{N_{V,z}\}^T + \{N_{W,y}\}^T \end{matrix} & \end{matrix}, \quad (9)$$

where

$$\begin{aligned} [N_{\alpha,x}] &= j_{11}[N_{\alpha,\xi}] + j_{12}[N_{\alpha,\eta}] + j_{13}[N_{\alpha,\zeta}] \\ [N_{\alpha,y}] &= j_{21}[N_{\alpha,\xi}] + j_{22}[N_{\alpha,\eta}] + j_{23}[N_{\alpha,\zeta}] \\ [N_{\alpha,z}] &= j_{31}[N_{\alpha,\xi}] + j_{32}[N_{\alpha,\eta}] + j_{33}[N_{\alpha,\zeta}] \end{aligned}; \quad \alpha \equiv U, V, W \quad (10)$$

and  $j_{lk}$  are the inverse Jacobian matrix components.

For linear elastic problems, the stiffness matrix of SFR4 takes the following simple form:

$$[K^e] = \int_0^1 \int_0^{1-\zeta} \int_0^{1-\eta-\zeta} ([B]^T [C] [B] DetJ)_{\xi,\eta,\zeta} d\xi d\eta d\zeta = \sum_{i=1}^{N_{pi}} w_i ([B]^T [C] [B] DetJ)_{\xi_i,\eta_i,\zeta_i}, \quad (11)$$

where  $[C]$  is the elasticity matrix relating the stress and strain vectors and  $N_{pi}$  is the number of integration points. For a homogeneous and isotropic material this matrix for a three-dimensional problem can be written as:

$$[C] = \begin{bmatrix} 2G + \lambda & \lambda & \lambda & 0 & 0 & 0 \\ \lambda & 2G + \lambda & \lambda & 0 & 0 & 0 \\ \lambda & \lambda & 2G + \lambda & 0 & 0 & 0 \\ 0 & 0 & 0 & G & 0 & 0 \\ 0 & 0 & 0 & 0 & G & 0 \\ 0 & 0 & 0 & 0 & 0 & G \end{bmatrix}. \quad (12)$$

The Lamé coefficients are expressed in terms of Young's modulus,  $E$ , and Poisson's ratio,  $\nu$ , by:

$$\lambda = \frac{E\nu}{(1+\nu)(1-2\nu)} \quad \text{and} \quad G = \frac{E}{2(1+\nu)}. \quad (13)$$

The approximation of the part corresponding to the rotation of space fiber is quadratic in terms of  $\xi$ ,  $\eta$  and  $\zeta$ . The element stiffness matrix is integrated exactly using a four-point numerical quadrature ( $N_{pi} = 4$ ) [15].

### 3. Numerical examples

In this section, we present various three-dimensional benchmark problems, selected from the literature, have been used to evaluate the performance and convergence rate of the proposed four-node tetrahedral solid element SFR4.

#### A. Cantilever beam

Fig. 2 shows a cantilever benchmark problem used in convergence study by Tian et al. [4]. The material parameters are: Young's modulus is  $E = 3.1 \times 10^7$  N/cm<sup>2</sup> and the Poisson's ratio is  $\nu = 0.3$ . The exact solution of deflection ( $v_{exact}$ ) at the center point of the free end is given by Timoshenko and Goodier [16]:

$$v_{exact} = \frac{P}{6EI} \left[ 3\nu \left( y - \frac{H}{2} \right)^2 (L - x) + \frac{1}{4} (4 + 5\nu) H^2 x + (3L - x)x^2 \right] \quad (14)$$

The displacements in the directions of the applied loads are computed and normalized with respect to the exact solutions of (14). Table 1 presents the convergence of the normalized tip deflection ( $v_{num}/v_{exact}$ ) at the center point of the free end. Obviously, the present element appeared to be the better performer compared to the classical first-order Tet4 element taken from Reference [1].

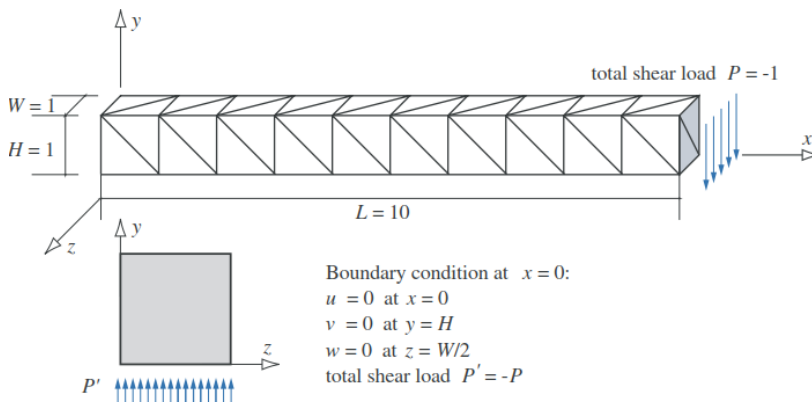


Figure 2: The cantilever benchmark problem used in convergence study, a  $10 \times 10 \times 10$  mesh is shown; a brick is disassembled into six tetrahedrons ( $W = 1$  cm,  $H = 1$  cm,  $L = 10$  cm and  $P = -1$  N).

Table 1: Normalized tip deflection ratios for the cantilever problem ( $v_{\text{num}}/v_{\text{exact}}$ )

Mesh	Tet4	SFR4
$10 \times 1 \times 1$	0.247	0.576
$20 \times 2 \times 2$	0.531	0.734
$30 \times 4 \times 4$	0.803	0.923
$40 \times 8 \times 8$	0.939	0.992

B. In-plane bending of a cantilever beam

Fig. 3 shows the geometry, boundary conditions and material properties of a cantilever beam subjected to a plane transverse bending load. A reference analytic solution of the transverse displacement of point C, belonging to the beam’s end face, is obtained using the Timoshenko beam theory:  $V_{ref}^C = 4.03 \text{ mm}$ . This cantilever beam is modeled with six meshes: three regular meshes M1, M2 and M3 and three distorted ones M4, M5 and M6 as shown in Fig. 4 (a brick element is disassembled into six tetrahedral elements). We summarize in Table 2 the normalized transverse displacement results. These numerical results show that the four-node tetrahedral SFR4 element is sensitive to mesh distortion. We also remark that SFR4 results are better than those of the non-rotational standard four-node tetrahedral element Tet4.

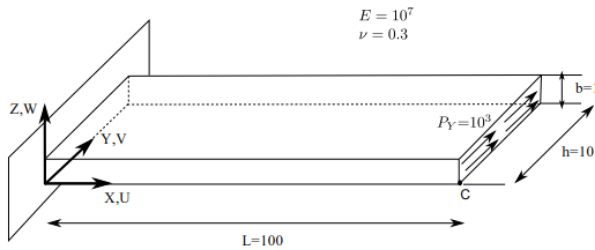


Figure 3: Plane bending of a thin cantilever beam ( $E = 10^7$  MPa,  $\nu = 0.3$ ,  $L = 100 \text{ mm}$ ,  $b = 1 \text{ mm}$ ,  $h = 10 \text{ mm}$  and  $P_Y = 10^3 \text{ N}$ ).

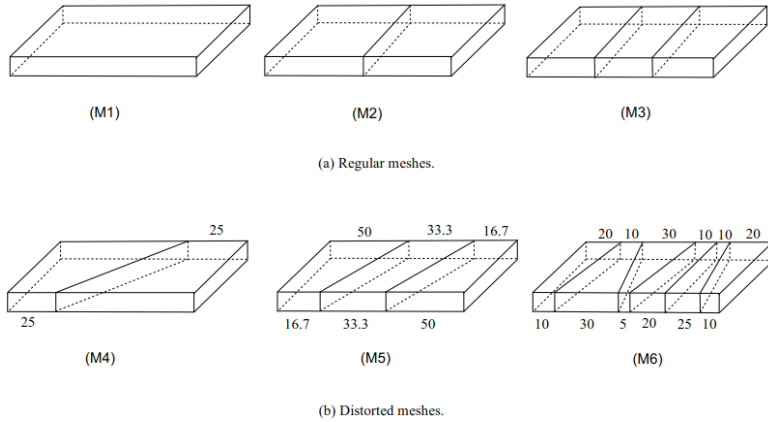


Figure 4: Plane bending of a cantilever beam. 3D meshing.

Table 2: In-plane bending of a cantilever beam. Normalized transverse displacement of point C

Mesh	Tet4	SFR4
M1	0.012	0.060
M2	0.034	0.221
M3	0.064	0.382
M4	0.014	0.110
M5	0.024	0.161
M6	0.058	0.306

### C. Straight cantilever beam

The straight cantilever beam test proposed by MacNeal and Harder [17] also investigates sensitivity to mesh distortion in bending. The beam is meshed with six elements (where a brick is disassembled into six tetrahedrons) and subjected to unit-shear force at free end (*Fig. 5*). The elements are distorted from regular bricks to parallelogram-shaped elements. Geometries, material properties and loading of straight cantilever beams are defined in *Fig. 5*. The theoretical solutions for beam problems obtained from MacNeal and Harder [17] are summarized in *Table 3*. The normalized tip deflection results are summarized in *Table 4*. These numerical results are always more accurate than the first-order tetrahedral element Tet4 in all mesh configurations.

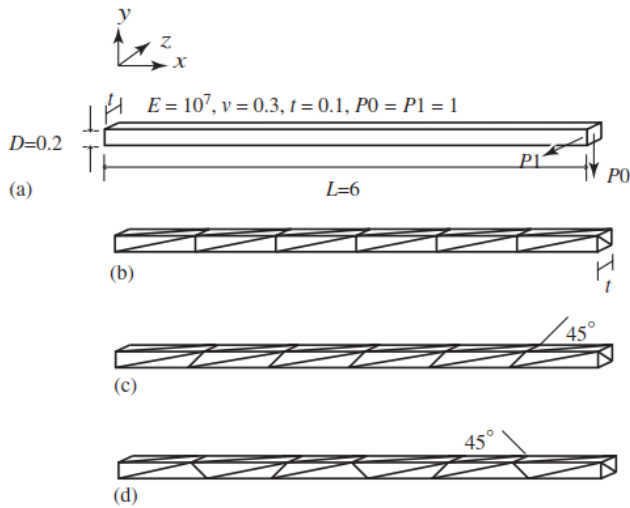


Figure 5: Straight cantilever beam: (a) geometry and material parameters; (b) regular mesh; (c) parallelogram mesh; (d) trapezoid mesh ( $E = 10^7 \text{ N/cm}^2$ ,  $\nu = 0.3$ ,  $L = 6 \text{ cm}$ ,  $t = 0.1 \text{ cm}$ ,  $D = 0.2 \text{ cm}$  and  $P_0 = P_1 = 1 \text{ N}$ ).

Table 3: Theoretical solutions for beam problems

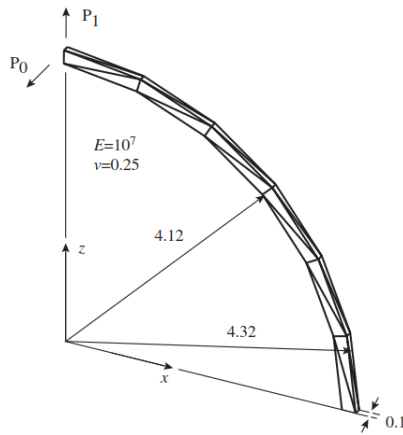
Tip load direction	Straight beam	Curved beam
In-plane shear	0.1081 (cm)	0.08734 (cm)
Out-of-plane shear	0.4321 (cm)	0.5022 (cm)

Table 4: Normalized tip deflection of the straight cantilever beam

Element shape	Load type	Tet4	SFR4
Regular	In-plane	0.010	0.053
	Out-of-plane	0.012	0.064
Trapezoidal	In-plane	0.006	0.032
	Out-of-plane	0.007	0.037
Parallelogram	In-plane	0.010	0.054
	Out-of-plane	0.007	0.038

#### D. Curved beam

The curved beam is portrayed in *Fig. 6*. This figure shows the geometry, meshes and material properties. All nodal DOFs at the clamped end are restrained. At the free end, in-plane and out-of-plane forces are applied. The displacements at the free end in the directions of the forces are computed and normalized by the reference solution of MacNeal and Harder [17] reported in *Table 3*. The normalized end deflections in the loading directions are tabulated in *Table 5*. Superior accuracy of the SFR4 element over the standard 4-node tetrahedral element can be observed.



*Figure 6*: Curved cantilever beam loaded with an in-plane  $P_1$  and out-of-plane  $P_0$  shear load ( $E = 10^7 \text{ N/cm}^2$ ,  $\nu = 0.25$ ,  $R_{int} = 4.12 \text{ cm}$ ,  $R_{ext} = 4.32 \text{ cm}$  and  $P_0 = P_1 = 1 \text{ N}$ ).

*Table 5*: Normalized end deflection of the curved beam

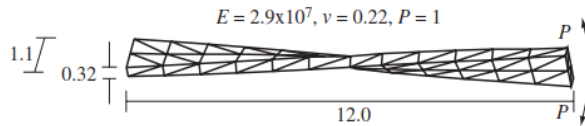
Load type	Tet4	SFR4
In-plane	0.023	0.092
Out-of-plane	0.005	0.121

#### E. Twisted beam

The clamped thick twisted beam proposed by MacNeal and Harder [17], under in-plane and out-of-plane unit loading ( $P = 1 \text{ N}$ ) at its free end, is analyzed. This test and the mesh are presented in *Fig. 7*. All the displacements at the clamped end are restrained. The theoretical solutions for displacements in the directions of the applied loads to the problems are [17]:  $0.005424 \text{ cm}$  for in-plane loading and  $0.001754 \text{ cm}$  for out-of-plane loading. The normalized results



with respect to the theoretical solutions of MacNeal and Harder [17] are summarized in *Table 6*. Again, the new element presented in this paper using SFR possesses the better performance compared with the classical 4-node tetrahedral element.



*Figure 7:* Twisted beam subjected to unit in-plane force and out-of-plane force ( $E = 2.9 \times 10^7 \text{ N/cm}^2$ ,  $\nu = 0.22$ ,  $L = 12 \text{ cm}$ ,  $b = 1.1 \text{ cm}$ ,  $h = 0.32 \text{ cm}$  and  $P = 1 \text{ N}$ ).

*Table 6:* Normalized displacements in the loading directions for the twisted cantilever beam problem

Tip load direction	Tet4	SFR4
In-plane loading	0.096	0.234
Out-of-plane loading	0.080	0.271

#### 4. Summary and conclusions

In this paper, a new four-node tetrahedral solid element SFR4 with six DOFs (three translations and three rotations) per node based on the Space Fiber Rotation concept is presented. This concept considers the 3D rotation of a virtual fiber that improves the displacement field by additional terms incorporated in any classical first-order elements. Numerical results show that the proposed four-node tetrahedral element SFR4 provides further improvement to the classical first-order four-node tetrahedral element Tet4, which is fully reflected in the analysis of three-dimensional elastic problems. In addition, the SFR concept is shown to be an efficient tool for developing high accuracy elements. As a future work, the reduced integration rule with one-point will be tested in SFR4 element to prevent some locking phenomena and to enhance computational efficiency.

#### References

[1] Pawlak, T. P., Yunus, S. M. and Cook, R. D., “Solid elements with rotational degrees of freedom: Part II—tetrahedron elements”, *International Journal for Numerical Methods in Engineering*, 31, 593–610, 1991. doi.org/10.1002/nme.1620310311.

- 
- [2] Sze, K. and Pan, Y., “Hybrid stress tetrahedral elements with Allman’s rotational DOFs”, *International journal for numerical methods in engineering*, 48, 1055–1070, 2000. doi.org/10.1002/(SICI)1097-0207(20000710)48:7<1055::AID-NME916>3.0.CO;2-P
  - [3] Matsubara, H., Iraha, S., Tomiyama, J., Yamashiro, T., and Yagawa, G. “Free mesh method using tetrahedral element including the vertex rotations”, in: *Proceedings-Japan Society of Civil Engineers*, DOTOKU GAKKAI, pp. 97–108, 2004.
  - [4] Tian, R. and Yagawa, G., “Generalized nodes and high-performance elements”, *International Journal for Numerical Methods in Engineering*, 64, 2039–2071, 2005. doi.org/10.1002/nme.1436.
  - [5] Tian, R., Matsubara, H. and Yagawa, G., “Advanced 4-node tetrahedrons”, *International Journal for Numerical Methods in Engineering*, 68, 1209–1231, 2006. doi.org/10.1002/nme.1744
  - [6] Tian, R., Matsubara, H., Yagawa, G., Iraha, S. and Tomiyama, J., “Accuracy improvements on free mesh method: A high performance quadratic triangular/tetrahedral element with only corners”, in: *Proc. of the Sixth World Congress on Computational Mechanics (WCCM VI)*, 2004.
  - [7] Hua, X. and To, C., “Simple and efficient tetrahedral finite elements with rotational degrees of freedom for solid modeling”, *Journal of Computing and Information Science in Engineering*, 7, 382–393, 2007. doi:10.1115/1.2798120.
  - [8] Ayad, R., “Contribution à la Modélisation numérique pour l’analyse des solides et des structures, et pour la mise en forme des fluides non newtoniens. Application à des matériaux d’emballage [Contribution to the numerical modeling of solids and structures and the non-Newtonian fluids forming process. Application to packaging materials]”, Habilitation to conduct researches, University of Reims, Reims, France, (in French), 2002.
  - [9] Meftah, K., “Modélisation numérique des solides par éléments finis volumiques basés sur le concept SFR [Numerical modeling of 3D structure by solid finite elements based upon the SFR concept] (Space Fiber Rotation)”, PhD thesis, University of Biskra, Algeria, (in French), 2013.
  - [10] Meftah, K., Ayad, R. and Hecini, M., “A new 3D 6-node solid finite element based upon the “Space Fibre Rotation” concept”, *European Journal of Computational Mechanics*, 22, 1-29, 2012. doi.org/10.1080/17797179.2012.721502.
  - [11] Ayad, R., Zouari, W., Meftah, K., Zineb, T. B., and Benjeddou, A., “Enrichment of linear hexahedral finite elements using rotations of a virtual space fiber”, *International Journal for Numerical Methods in Engineering*, 95, 46-70, 2013. doi.org/10.1002/nme.4500.
  - [12] Meftah, K., Zouari, W., Sedira, L. and Ayad, R., “Geometric non-linear hexahedral elements with rotational DOFs”, *Computational Mechanics*, 57, 37-53, 2016. doi.org/10.1007/s00466-015-1220-8.
  - [13] Meftah, K., Sedira, L., Zouari, W., Ayad, R., and Hecini, M., “A multilayered 3D hexahedral finite element with rotational DOFs”, *European Journal of Computational Mechanics*, 24, 107-28, 2015. doi.org/10.1080/17797179.2015.1089462.
  - [14] Zouari, W., Assarar, M., Meftah, K. and Ayad, R., “Free vibration analysis of homogeneous piezoelectric structures using specific hexahedral elements with rotational DOFs”, *Acta Mechanica*, 226, 1737-56, 2015. doi.org/10.1007/s00707-014-1274-2.
  - [15] Dhondt, G. D. C., “The finite element method for three-dimensional thermomechanical applications”, John Wiley & Sons Inc, 2004.
  - [16] Timoshenko, S. P. and Goodier, J. N., “Theory of Elasticity”, 3<sup>rd</sup> edition, McGraw-Hill, New York, 1970.
  - [17] MacNeal, R. H., and Harder, R. L., “A proposed standard set of problems to test finite element accuracy”, *Finite Elements in Analysis and Design*, 1, 3–20, 1985. doi.org/10.1016/0168-874X(85)90003-4.

## A Liquid Metal Flow Between Two Coaxial Cylinders System

Abdelkrim MERAH<sup>1</sup>, Ridha KELAIAIA<sup>2</sup>, Faiza MOKHTARI<sup>3</sup>

<sup>1</sup>Department of Mechanical Engineering, Faculty of Technology, M'Hamed Bougara  
University of Boumerdes. Algeria, e-mail: abdelkrimerah@univ-boumerdes.dz

<sup>2</sup>Faculty of Technology, Université 20 Août 1955-Skikda, BP 26 Route Elhadeik, Skikda,  
Algeria, e-mail: r.kelaiaia@univ-skikda.dz

<sup>3</sup>Faculty of Physics, University of Sciences and Technology, USTHB, BP, BP 32 El-Alia,  
Bab-Ezzouar, Algiers, 16111, Algeria, e-mail: faiza.mokhtari@gmail.com

Manuscript received September 22, 2018; revised December 30, 2018

**Abstract:** The Taylor-Couette flow between two rotating coaxial cylinders remains an ideal tool for understanding the mechanism of the transition from laminar to turbulent regime in rotating flow for the scientific community. We present for different Taylor numbers a set of three-dimensional numerical investigations of the stability and transition from Couette flow to Taylor vortex regime of a viscous incompressible fluid (liquid sodium) between two concentric cylinders with the inner one rotating and the outer one at rest. We seek the onset of the first instability and we compare the obtained results for different velocity rates. We calculate the corresponding Taylor number in order to show its effect on flow patterns and pressure field.

**Keywords:** Taylor-Couette, rotating cylinders, liquid metal flow.

### 1. Introduction

The fluid contained in the rotor-stator gap, driven by the inner rotating cylinder is called Couette flow, or commonly, Taylor-Couette flow [1-4]. The rotation of the inner cylindrical wall produces the least stable situation, because it generates a centrifugal force which ejects the fluid towards the outer wall, thus destabilizing the flow. A theoretical formalization of this problem has developed for the case of inviscid fluids [2, 3].

In 1923, in a seminal paper, Taylor [4] combined the theoretical and experimental approaches and studied the linear stability of a viscous fluid, as shown by the Couette profile, valid for low speeds. When the angular velocity of the inner cylinder is increased above a certain threshold, the circular Couette flow becomes unstable and toroidal vortices flow known as Taylor vortex flow are occurring Taylor has shown that the stability calculation methods and the

assumed boundary conditions give results that exactly match the experimental data. Since Taylor's famous article [4], numerous experimental, theoretical and numerical studies on the presence and evolution of Taylor's vortices have been undertaken and extended to other geometries [5-12]. The subject of liquid metal flow between two coaxial, independently rotating cylinders is important for the understanding of nonlinear phenomena of the rotating flows. These are ubiquitous in nature and technology contexts such as stellar interiors, accretion discs, the Earth's core, crystal growth furnaces intended for the ingots production according to the Kyropoulos or Czochralski techniques, and rotating machinery such as electric motors, pumps, rotating blade couplers. Moreover, the liquid sodium is widely used as a primary coolant for nuclear fusion reactors due to the physical and chemical features, high heat capacity and high thermal conductivity, that allow it to be used as a primary coolant for nuclear fusion reactors. In this paper, the focus is on the transition of Couette flow to Taylor vortex for different Taylor numbers. The considered fluid is the liquid sodium, which has many applications in industrial and engineering processes.

## 2. Modelling

The main objective of this work is to investigate numerically and to highlight the effect of the Taylor number values on the velocity field of the liquid sodium, which is an incompressible, inviscid and Newtonian liquid, contained in a small cylindrical gap with a large aspect ratio. The outer cylinder (stator), with  $R_2 = 28.5 \text{ mm}$  is maintained stationary, and the inner one (rotor) with radius  $R_1 = 23.65 \text{ mm}$  is rotating. The gap ratio  $\delta$  is given by ( $\delta = d / R_1$ ) where  $d = 4.85 \text{ mm}$  is the gap between the cylinders ( $d = R_2 - R_1$ ), as shown in *Fig. 1*. The height of the considered Taylor-Couette system is  $H = 155 \text{ mm}$  as shown in *Fig. 1*. Therefore, this flow system is governed by the following parameters: radii ratio  $R_1 / R_2 = 0.8$ , which corresponds to a small annular gap, and a large aspect ratio  $H / d = 31.9$ . The inner cylinder rotates at angular velocity  $\Omega$  which is increased stepwise during the computation. Different flow structures are then found. The first pattern corresponds to the circular Couette flow followed by the Taylor-vortex flow (TVF). TVF appears at a critical value  $T_c$  of the Taylor number defined as  $Ta = Re \cdot \delta^{1/2}$ . Reynolds number is given by  $Re = \rho R_1 \Omega d / \mu$ . The working fluid is liquid sodium. It has constant density and viscosity  $\rho = 920 \text{ kg.m}^{-3}$  and  $\mu = 6.53 \cdot 10^{-4} \text{ kg.m}^{-1} \text{ s}^{-1}$ , respectively. The governing equations for the flow system are the conservation equations, namely, the continuity and Navier-Stokes equations. The cylindrical gap is conveniently described by  $r$ ,  $\theta$  and  $z$ , denoting the usual cylindrical coordinates the radial, azimuthal and axial directions respectively, as shown in *Fig. 1*. Further, we denote the velocity components in the increasing  $r$ ,  $\theta$  and  $z$  directions  $V_r$ ,

$V_\theta$  and  $V_z$  respectively, and the pressure  $P$ . The governing equations can be written as,

$$\frac{1}{r} \frac{\partial}{\partial r} (rV_r) + \frac{1}{r} \frac{\partial}{\partial \theta} (V_\theta) + \frac{\partial}{\partial z} (V_z) = 0 \quad (1)$$

$$V_r \frac{\partial V_r}{\partial r} + \frac{V_\theta}{r} \frac{\partial V_r}{\partial \theta} + V_z \frac{\partial V_r}{\partial z} - \frac{V_\theta^2}{r} = -\frac{1}{\rho} \frac{\partial P}{\partial r} + \nu \left\{ \nabla^2 V_r - \frac{V_r}{r^2} - \frac{2}{r^2} \frac{\partial V_\theta}{\partial \theta} \right\} \quad (2)$$

$$V_r \frac{\partial V_\theta}{\partial r} + \frac{V_\theta}{r} \frac{\partial V_\theta}{\partial \theta} + V_z \frac{\partial V_\theta}{\partial z} + \frac{V_r V_\theta}{r} = -\frac{1}{\rho} \frac{1}{r} \frac{\partial P}{\partial \theta} + \nu \left\{ \nabla^2 V_\theta - \frac{V_\theta}{r^2} + \frac{2}{r^2} \frac{\partial V_r}{\partial \theta} \right\} \quad (3)$$

$$V_r \frac{\partial V_z}{\partial r} + \frac{V_\theta}{r} \frac{\partial V_z}{\partial \theta} + V_z \frac{\partial V_z}{\partial z} = -\frac{1}{\rho} \frac{\partial P}{\partial z} + \nu \nabla^2 V_z \quad (4)$$

$$\nabla^2 = \frac{\partial^2}{\partial r^2} + \frac{1}{r} \frac{\partial}{\partial r} + \frac{1}{r^2} \frac{\partial^2}{\partial \theta^2} + \frac{\partial^2}{\partial z^2}, \quad (5)$$

where  $\rho$  and  $\nu$  denote the liquid sodium density and kinematic viscosity respectively.

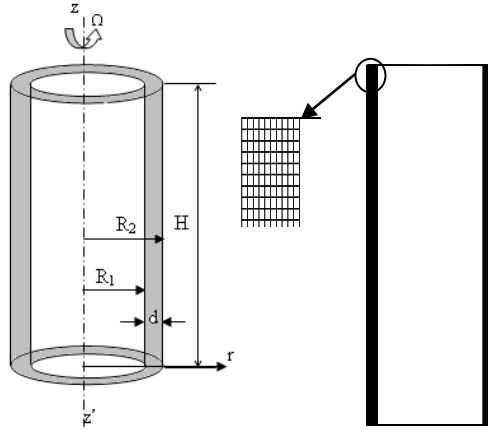


Figure 1.: Flow system, notations and used meshes.

In this paper, the focus is on the understanding of the Taylor number  $Ta$  effect on the distribution of velocity field in liquid confined between two coaxial cylinders. The Taylor number quantifies the ratio between centrifugal and viscous forces acting on liquid. Above the critical Taylor number value, centrifugal forces exceed viscous forces, and the flow becomes unstable. There

are various forms of the Taylor number and the choice varies from one investigation to another, and it is used as a criterion of the stability of flow. In this work, the inner cylinder is rotating and the outer cylinder is fixed. At the wall, the flow has zero axial and radial velocity, while it is characterized by a tangential velocity component. Therefore, the associated non-slip boundary conditions are assumed. The radial, tangential and axial velocity components at the inner, outer walls and end-plates are given as  $V_r(r = R_1 \text{ or } r = R_2) = 0$ ,  $V_\theta(Z = 0 \text{ or } Z = H) = 0$ ,  $V_\theta(r = R_1) = \Omega R_1$ ,  $V_\theta(r = R_2) = 0$ ,  $V_\theta(Z = 0 \text{ or } Z = H) = 0$ ,  $V_z(r = R_1 \text{ or } r = R_2) = 0$  and  $V_z(Z = 0 \text{ or } r = H) = 0$ , respectively.

The problem is solved using the code ANSYS®Fluent 16.0 package based on the finite volume method. The momentum discretization has been performed with a QUICK scheme. The PISO algorithm (Pressure Implicit with Splitting of Operator) is applied for pressure-velocity coupling and the pressure-based solver has been discretized with PRESTO scheme (PREssure STaggering Option). The Green-Gauss cell-based method has been used for gradients evaluation. The convergence is handled by monitoring residuals of continuity and momentum equations, while the residuals are set to  $10^{-6}$ . The used mesh is regular and it has about one million nodes. In Fig. 1, the structure of the mesh employed in the three-dimensional simulations is given.

### 3. Results and discussion

The stable laminar regime which is the basic flow existing in the absence of any disturbance.

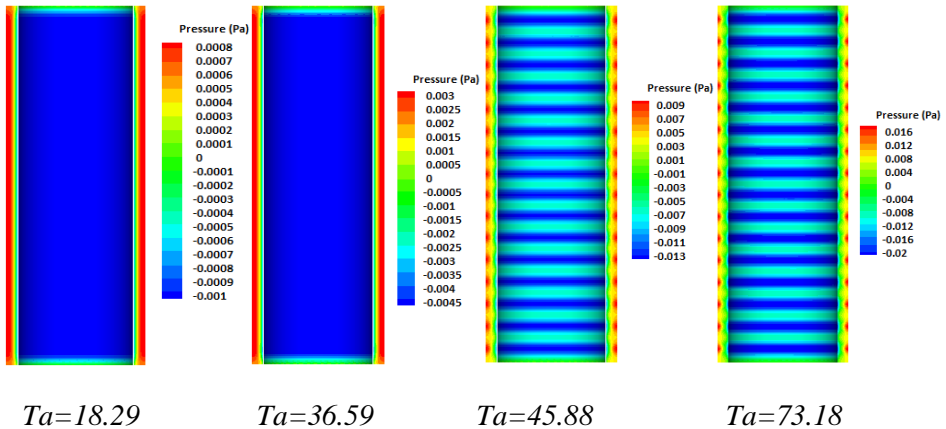


Figure 2: Computed pressure for different Taylor numbers.

This can be described as a homogeneous movement with a high degree of symmetry throughout the fluid, which is characterized by the occurrence of two cells, one located at the lower edge and the other at the upper edge. Then, the speed of rotation is slightly increased and then the formation of Taylor vortices occurs, which propagate from the edges towards the middle until the complete appearance of the cells in the whole cylinder. The appearance of the first instability of Taylor-Couette consists of the occurrence of a periodic axial stationary wave associated with the base flow.

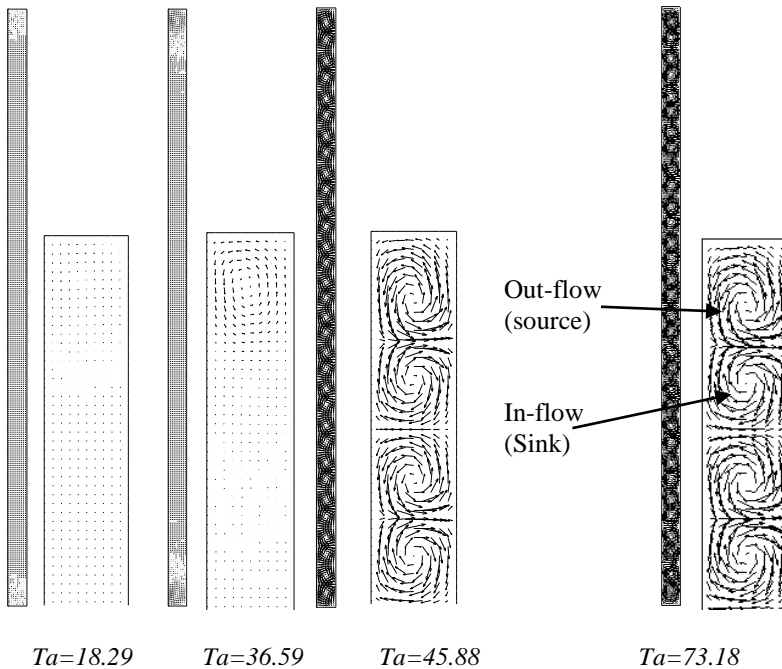
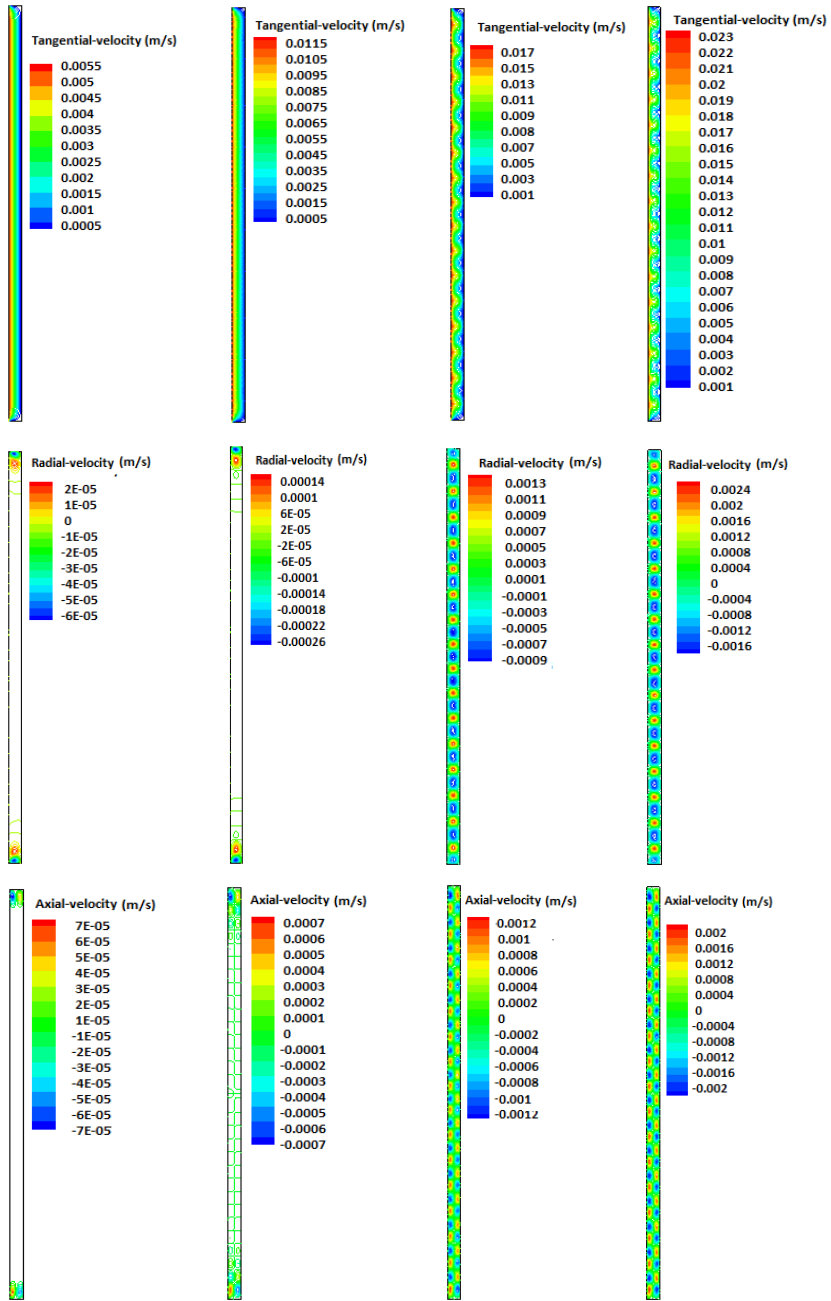


Figure 3:  $(V_r, V_z)$  components for different Taylor numbers.

The inner cylinder rotates counterclockwise as shown in *Fig. 1*, and the upper vortex rotates in the same direction as shown in *Fig. 3*. In succession, more vortices are added in the cylindrical gap, and the flow is organized in the form of rolls or Taylor vortices. These vortices travel along and around the inner cylinder. During the rotation flow, the source and the sink zones appear. *Fig. 4* depicts the axial, radial and tangential components of the flow in horizontal right plane. The velocity field  $V$  of the fluid is time-independent until the Taylor number exceeds a critical value  $Ta=41.35$ . This value is found to be in a good agreement with experimental and theoretical results found before [5, 10-12].



$Ta=18.29$

$Ta=36.59$

$Ta=45.88$

$Ta=73.18$

Figure 4: Velocity components for different Taylor numbers.



No-slip conditions imposed on the endplates of the system are responsible for the reducing of the azimuthal velocity component. The velocity components depend on Taylor Ta number values.

### 3. Conclusion

The first hydrodynamic instability of sodium liquid flow contained between two infinite coaxial cylinders, where the outer cylinder is stationary and the inner one is rotating was investigated numerically using the code ANSYS®Fluent 16.0 package based on the finite volume method. For very low Taylor numbers, the results show that the basic flow is stationary, axisymmetric invariant by vertical translation, and no cells are formed in the gap. By increasing the Taylor number, two first cells appeared close to each end plates, called Eckman's vortices. Beyond a threshold value, it is observed that this basic flow becomes unstable. For large Taylor numbers, the contra-rotating rollers in the liquid sodium cylindrical gap flow are appearing, and extend all-around of the inner cylinder. The tangential velocity values are larger than radial and axial velocity components. The results seem satisfactory regarding the hydrodynamic instability behavior, in agreement with experimental data found in the literature [13].

### References

- [1] Stokes, G., "On a difficulty in the theory of Sound", *Philosophical Magazine*, 1848, Series 3, 33, Issue 223.
- [2] Couette, M., "La viscosité des liquides", *Bulletin des Sciences Physiques*, vol. 4, pp. 40-62, 1888.
- [3] Mallock, A., "Determination of the viscosity of water", *Proceedings Royal Society*. London, vol.45, pp. 126-132, 1888.
- [4] Taylor, G. I., "Stability of a viscous liquid contained between two rotating cylinders", *Philosophical Transaction of the Royal Society*. London, vol. A 223, pp. 289-343, 1923.
- [5] Ahlers, G., Cannell, D. S., Dominguez-Lerma, M. A., "Possible mechanism for transitions in wavy Taylor-vortex flow", *Physical Review*, vol. A 27, pp. 1225-1227, 1983.
- [6] Wimmer, M., "An experiment investigation of Taylor vortex flow between conical cylinders", *Journal of Fluid Mechanics*, vol. 292, pp. 205-227, 1995.
- [7] Sprague, M. A., Weidman, P. D., "Continuously tailored Taylor vortices", *Physics of Fluids*, vol. 21 pp. 014106-014114, 2009.
- [8] Hoffmann, F. H., Busse, N. P., "Instabilities of shear flows between two coaxial differentially rotating cones", *Physics of Fluids*, vol. 11, p. 1676, 1999.
- [9] Chandrasekhar, S., "Hydrodynamic and Hydromagnetic Stability", Oxford Press, 1961.
- [10] Ellingsen, S. A., Andersson, H. I., "Mixing layer between two co-current Taylor-Couette flows", *European Journal of Mechanics B/Fluids*, vol. 37, pp. 23-28, 2013.
- [11] Lalaoua, A., "Transition to Taylor vortex flow between combinations of circular and conical cylinders", *European Physical Journal Applied Physics*, vol. 77(1), pp. 11101-11108, 2017.

- [12] Tilton, N., Martinand, D., “Taylor–Couette–Poiseuille flow with a weakly permeable inner cylinder: absolute instabilities and selection of global modes”, *Journal of Fluid Mechanics*, vol. 849, pp. 741-776, 2018.
- [13] Fenstermacher, P. R., Swinney, H. L., Gollub, J. P., “Dynamical instabilities and the transition to chaotic Taylor vortex flow”, *Journal of Fluid Mechanics*, 1979, vol. 94, pp.103-128.



## Numerical Study of Fluid Flow Through a Confined Porous Square Cylinder

Salah GUERBAAI<sup>1</sup>, Mouna TOUIKER<sup>2</sup>, Kamel MEFTAH<sup>3</sup> and  
Abdeslam OMARA<sup>4</sup>

<sup>1</sup> Department of Mechanical Engineering, Université 20 Août 1955- Skikda,  
e-mail: guer\_salah@yahoo.fr

<sup>2</sup> Department of Physics, Université 20 Août 1955- Skikda, e-mail: Touikerm21@yahoo.fr

<sup>3</sup> University of Biskra, Laboratoire de Génie Energétique et Matériaux (LGEM),  
Faculty of Science and Technology, Biskra 07000, Algeria, e-mail: meftah.kamel@gmail.com

<sup>4</sup> Department of Physics, Université des frères Mentouri Constantine 1,  
e-mail: abdeslam\_omara@yahoo.fr

Manuscript received January 21, 2019; revised July 7, 2019.

**Abstract:** A numerical study is performed to analyze steady state forced convection fluid flow through a confined porous square cylinder. The Darcy-Brinkman-Forchheimer model is adopted for the porous region. The finite volume method and the iterative SIMPLE algorithm are used to solve the governing equations. The results obtained are presented for the streamlines, variation of Nusselt number and drag coefficient for the range of conditions as  $5 \leq Re \leq 40$  and  $10^{-2} \leq Da \leq 10^{-6}$ .

**Keywords:** Forced convection, porous square cylinder, drag coefficient, Darcy number, finite volume method.

### 1. Introduction

The study of flows past or through a cylinder, triangular or square prism has received considerable attention in recent years because of their wide applications in engineering, for example, the cooling of electrical components, heat exchangers and cooling towers.

Breuer et al. [1] studied the confined flow of an incompressible fluid around a square cylinder with a blockage ratio of 1/8 using two different numerical techniques, namely Lattice-Boltzmann automata (LBA) and a finite volume method (FVM). Gupta et al. [2] have investigated the two dimensions forced convective heat transfer of a non-Newtonian fluid past a square cylinder with a blockage ratio of 1/8. The same study was carried out by Paliwal et al. [3], but

for unconfined flow and with a blockage ratio of 1/15 and by Dhiman et al. [4] for an isolated unconfined square cylinder. The effect of Reynolds and Prandtl numbers on heat transfer across a square cylinder was tested by Dhiman et al. [5]. Sharma et al. [6] analyzed the effect of buoyancy forces on the upward flow of an incompressible fluid around a square cylinder

<b>Nomenclature</b>		
$b$	Side length of the square cylinder, $m$	$X, Y$ Dimensionless Cartesian coordinates
$C_{Df}$	Viscous drag coefficient	<i>Greek symbols:</i>
$C_{DP}$	Pressure drag coefficient	$\mu$ Dynamic viscosity, $kg\ m^{-1}s^{-1}$
$C_D$	Total drag coefficient	$\Lambda$ Viscosity ratio, $\mu_{eff}/\mu_f$
$d$	Particle diameter, $m$	$\varepsilon$ Porosity
$Da$	Darcy number, $\kappa/b^2$	$\theta$ Dimensionless temperature
$H$	Height of the computational domain, $m$	$\varphi$ Blockage ratio, $b/H$
$k$	Thermal conductivity, $W/m\ K$	$\kappa$ Permeability of the material, $m^2$
$L$	Length of the computational domain, $m$	
$Nu$	Nusselt number	<i>Subscripts:</i>
$P$	Dimensionless pressure	<i>eff</i> Effective
$Pr$	Prandtl number	<i>f</i> Fluid
$Re$	Reynolds number	<i>fr</i> Front face
$R_k$	Ratio of thermal conductivity of porous and fluid layers, $k_{eff}/k_f$	<i>r</i> Rear face
$T$	Temperature, $K$	<i>t</i> Top face
$U, V$	Dimensionless velocity components	<i>b</i> Bottom face

Flow and heat transfer through permeable bodies has been a subject of great interest in these last years since they have a large contact surface and therefore tend to improve heat exchange compared to their solid counterparts. Alazmi and Vafai [7] analyzed in detail the different types of interfacial conditions between a porous medium and a fluid layer. The effect of Reynolds and Darcy numbers on the structure of a flow through a porous square cylinder was investigated by Yu et al. [8]. Wu and Wang [9] analyzed numerically an unsteady flow and convection heat transfer for a heated square porous cylinder in a channel. The heat transfer through an isolated porous square cylinder maintained at a constant temperature was examined by Dhinakaran and Ponmozhi [10], their results showed that the flow pattern through and around the porous cylinder depends much on the Darcy number of the porous medium. Mahdhaoui et al. [12] examined the effects of Darcy and Reynolds numbers on the flow structure and heat transfer through a porous square cylinder with a blockage ratio of 1/11. Their results show principally that for a low Darcy number, there is a recirculation zone after the porous medium, at  $Da=10^{-6}$  the flow structure is similar to that of a solid square cylinder.

The aim of this work is to study the effects of Reynolds and Darcy numbers of the flow pattern through and around a porous cylinder placed between two parallel plates with a blockage ratio of 1/8.

## 2. Mathematical formulation

The geometric model studied is identical to that examined by Dhiman et al. [11] but in the case of a porous square cylinder which is exposed to a parabolic stream velocity as shown in *Fig.1*. The values of  $X_u$ ,  $X_d$  and  $H$  are respectively  $8.5b$ ,  $16.5b$  and  $8b$ .

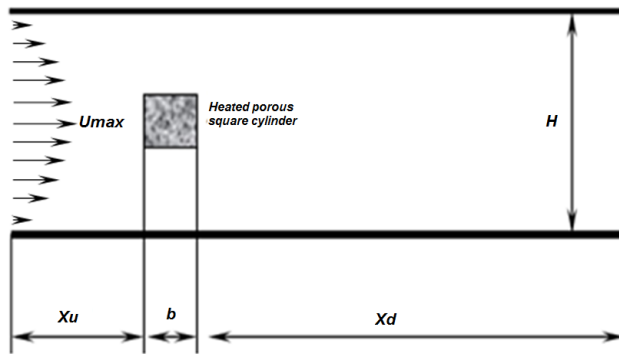


Figure 1: Schematic diagram of the physical system.

In the Cartesian coordinate system, the fundamental dimensionless governing equations based on Darcy-Brinkman-Forchheimer extended model are as follows:

Continuity equation:

$$\frac{\partial U}{\partial X} + \frac{\partial V}{\partial Y} = 0 \quad (1)$$

Momentum equations:

$$\begin{aligned} \frac{1}{\varepsilon} \left( U \frac{\partial U}{\partial X} + V \frac{\partial U}{\partial Y} \right) &= -\varepsilon \frac{\partial P}{\partial X} + \frac{\Lambda}{Re} \left( \frac{\partial^2 U}{\partial X^2} + \frac{\partial^2 U}{\partial Y^2} \right) - \\ &- C \left( \varepsilon \frac{1}{ReDa} U + \frac{1.75}{\sqrt{150}} \frac{1}{\sqrt{Da}} \times \frac{\sqrt{U^2 + V^2}}{\sqrt{\varepsilon}} U \right) \quad (2) \\ \frac{1}{\varepsilon} \left( U \frac{\partial V}{\partial X} + V \frac{\partial V}{\partial Y} \right) &= -\varepsilon \frac{\partial P}{\partial Y} + \frac{\Lambda}{Re} \left( \frac{\partial^2 V}{\partial X^2} + \frac{\partial^2 V}{\partial Y^2} \right) - \end{aligned}$$

$$-C \left( \varepsilon \frac{1}{ReDa} V + \frac{1.75}{\sqrt{150}} \frac{1}{\sqrt{Da}} \times \frac{\sqrt{U^2 + V^2}}{\sqrt{\varepsilon}} V \right) \quad (3)$$

Energy equation:

$$\frac{1}{\varepsilon} \left( U \frac{\partial \theta}{\partial X} + V \frac{\partial \theta}{\partial Y} \right) = \frac{Rk}{RePr} \left( \frac{\partial^2 \theta}{\partial X^2} + \frac{\partial^2 \theta}{\partial Y^2} \right) \quad (4)$$

$$C = \begin{cases} 0. & \text{outside the porous medium} \\ 1. & \text{in the porous medium} \end{cases} \quad (5)$$

$$\varepsilon = \begin{cases} 1. & \text{outside the porous medium} \\ 0 < \varepsilon < 1 & \text{in the porous medium} \end{cases} \quad (6)$$

The dimensionless variables introduced are given as:

$$X = \frac{x}{b}; Y = \frac{y}{b}; U = \frac{u}{u_{max}}; V = \frac{v}{u_{max}}; P = \frac{p}{\rho_f u_0^2}; \theta = \frac{T - T_0}{\Delta T} \quad (7)$$

The porosity and the Darcy number are related by the Carman-Kozeny equation given by:

$$Da = \frac{1}{180.b^2} \frac{\varepsilon^3 d^2}{(1-\varepsilon)^2} = \frac{\kappa}{b^2}. \quad (8)$$

$d$  is the mean particle diameter in the porous cylinder, each particle may be of 100  $\mu\text{m}$  in diameter [10].

The dimensionless boundary conditions are:

$$\begin{aligned} U = 0. ; V = 0. ; \frac{\partial \theta}{\partial Y} = 0 & \quad \text{at upper and lower boundary} \\ U = 0.5Y(1 - 0.125Y); V = 0; \theta = 0 & \quad \text{at the inlet boundary} \\ \theta = 1 & \quad \text{on the surface of the square cylinder} \\ \frac{\partial U}{\partial X} = \frac{\partial V}{\partial X} = \frac{\partial \theta}{\partial X} = 0 & \quad \text{at the exit boundary} \\ \mu_f \frac{\partial u_n}{\partial n} \Big|_f = \mu_{eff} \frac{\partial u_n}{\partial n} \Big|_p & \quad \text{at the porous - fluid interface} \end{aligned} \quad (9)$$

where  $n$  represents the direction normal to the surface of the cylinder and

$$\mu_{eff} = \frac{\mu_f}{\varepsilon} \quad (10)$$

The heat transfer from the porous cylinder to the fluid is evaluated from the local Nusselt number calculated as:

$$Nu = -\frac{k_{eff} \partial \theta}{k_f \partial n}. \quad (11)$$

$R_k = \frac{k_{eff}}{k_f}$  is taken equal to 1.

The total drag coefficient  $C_D$  on the cylinder is given by:

$$C_D = C_{D_p} + C_{D_f} \quad (12)$$

The drag coefficients due to the pressure and viscous forces can be obtained by evaluating the following integrals:

$$C_{D_p} = 2.0 \int_0^1 (P_{fr} - P_r) dY, \quad C_{D_f} = \frac{2.0}{Re} \int_0^1 \left[ \left( \frac{\partial U}{\partial Y} \right)_b + \left( \frac{\partial U}{\partial Y} \right)_t \right] dX \quad (13)$$

### 3. Solution method and validation

#### 3.1. Solution method

A control volume approach presented by Patankar [13] is used to discretize the dimensionless governing equations (1) - (4). The semi-implicit method for pressure-linked equation (SIMPLE) algorithm was used for solving the coupled momentum and continuity equations using the corresponding boundary conditions given in equations (9). The convergence of the sequential iterative solution is obtained when:

$$\max \left( (\phi_{i,j}^{k+1} - \phi_{i,j}^k) / \phi_{i,j}^{k+1} \right) \leq 10^{-5}, \quad (14)$$

where  $\phi_{i,j}^k$  is the general dependent variable which can stand for  $U$ ,  $V$ , or  $\theta$  at every  $(X, Y)$  position of the discretized domain,  $k$  is the iteration step.

#### 3.2. Code validation

The currently used FORTRAN code is firstly validated in terms of the drag coefficient and the recirculation length with the published results of Dhiman et al. [11], Breuer et al. [1] and Gupta et al. [2] for the case of a flow of an incompressible fluid ( $Pr = 0.7$ ) across a solid square cylinder with a blockage ratio of 1/8 as can be shown in *Table 1*.

*Table 1:* Comparison of drag coefficient ( $C_D$ ) and recirculation length ( $L_r$ ) with the literature for the case of solid square cylinder

	$Re = 20$		$Re = 30$		$Re = 40$	
	$L_r$	$C_D$	$L_r$	$C_D$	$L_r$	$C_D$
Present work	1.05	2.44	1.63	2.00	2.17	1.76
Dhiman et al. [11]	1.05	2.44	1.62	1.99	2.17	1.75
Breuer et al. [1]	1.04	2.50	1.60	2.00	2.15	1.70
Gupta et al. [2]	0.90	2.45	1.40	2.06	1.90	1.86

A second validation was made with a comparison of the streamlines drawn by Mahdhaoui et al. [12] for a laminar flow through a porous square cylinder with blockage ratio of 1/11 and for different values of Darcy number ( $Da = 10^{-2}$ ,  $10^{-4}$  and  $10^{-6}$ ) at  $Re = 20$ . This comparison is presented in *Fig.2*.

The results show that the present study is in good agreement with the published results.

#### 4. Results and discussion

A numerical study was conducted to investigate the effects of porous properties on several hydrodynamic and thermal parameters such as wake structure, streamlines, drag coefficient and heat transfer rate. The results have been obtained for the following range of parameters:

Reynolds number:  $1 < Re < 40$ , Darcy number:  $Da = 10^{-6}$ ,  $10^{-4}$ ,  $10^{-3}$ ,  $10^{-2}$  and the corresponding porosity:  $\varepsilon = 0.629$ ,  $0.8$ ,  $0.977$ ,  $0.993$  respectively.

*Fig.3* shows the effects of Reynolds and Darcy numbers on the flow structure. Streamlines near the square cylinder are given for  $Re = 10$ ,  $20$  and  $40$  and  $Da = 10^{-2}$ ,  $10^{-3}$ ,  $10^{-4}$  and  $10^{-6}$ . For high values of Darcy number, the fluid encounters a low resistance as it passes through the porous medium with the complete absence of recirculation cells after the obstacle. With the decrease in permeability of the obstacle, two counter rotating eddies are formed behind the square cylinder, whose size increases with increasing of the Reynolds number.

For very small Darcy number values ( $Da = 10^{-6}$ ) the flow structure is similar to that of the flow through a solid square cylinder and the fluid cannot pass through the square cylinder.



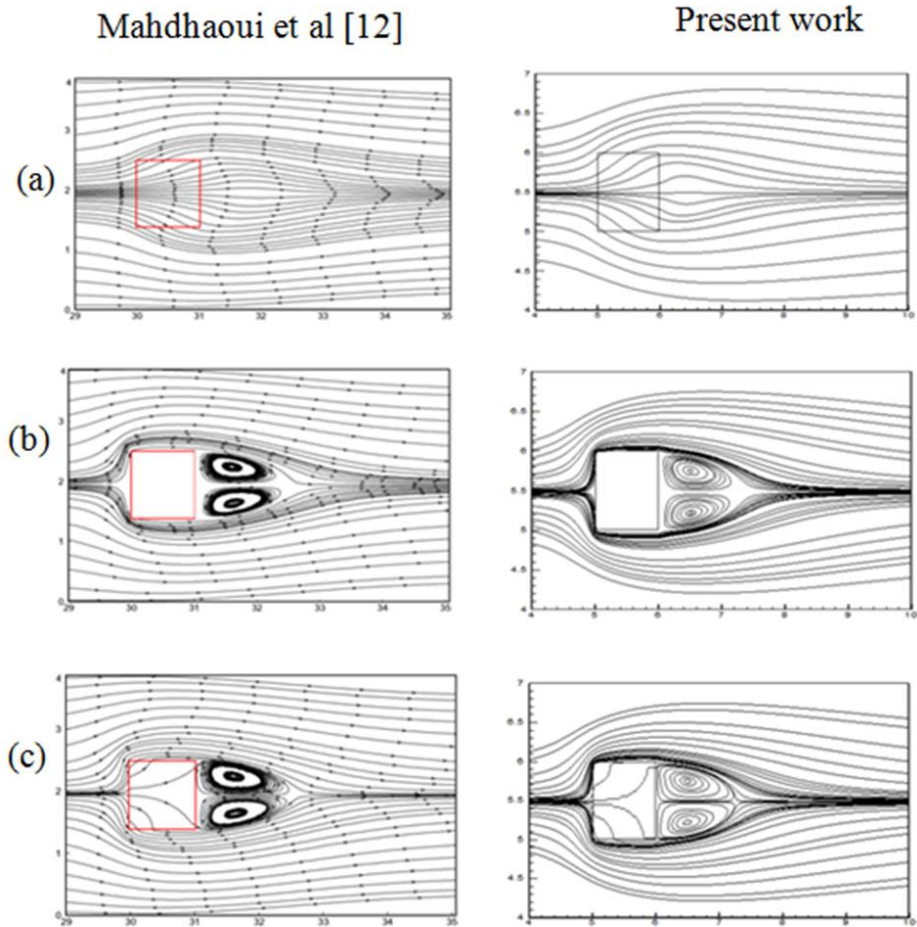


Figure 2: Comparison of stream lines between the present numerical solution and those of Mahdhaoui et al. [12] at  $Re = 20$  and at different  $Da$ . (a)  $Da = 10^{-2}$ , (b)  $Da = 10^{-4}$  and (c)  $Da = 10^{-6}$ .

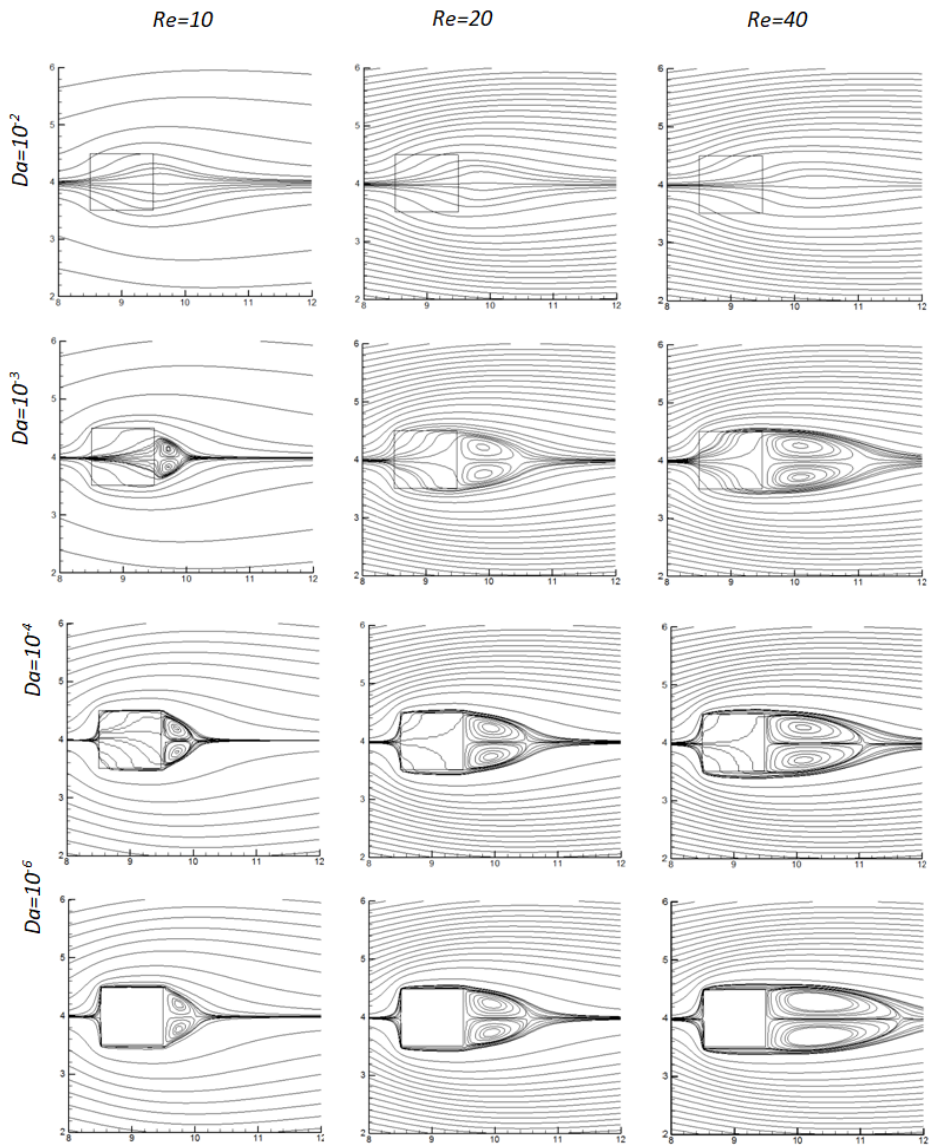


Figure 3: Streamline plots for various Reynolds and Darcy numbers.

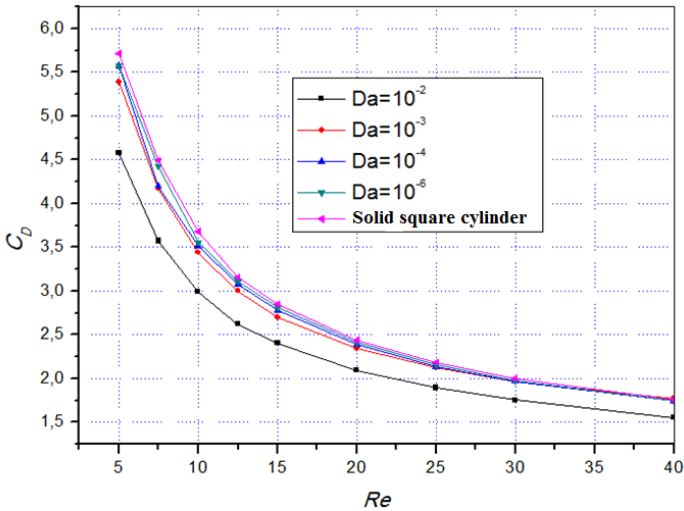


Figure 4: Variation of the drag coefficient with Reynolds number for different Darcy numbers.

The value of the drag coefficient decreases with the increase in the value of the Reynolds number which results in a depletion of the viscous layer.

The high values of the permeability of the material cause a low resistance to the flow of the fluid and thus a reduction of the pressure gradient inside the porous medium, which causes a decrease in the value of the drag coefficient as shown in Fig 4.

Fig. 5 shows the variation of the average Nusselt number for different Darcy and Reynolds numbers. It can clearly be seen that the heat transfer rate increases with the increase in Reynolds number on the one hand and with the increase in the permeability of the material of the obstacle on the other hand.

The variation of the length of the recirculation region with Reynolds number is shown in Fig. 6. It shows that the wake length decreases with the increasing Darcy number for  $Re < 35$  and increases for  $Re > 35$ . This same observation was reported by Dhinakaran and Ponmozhi [10].

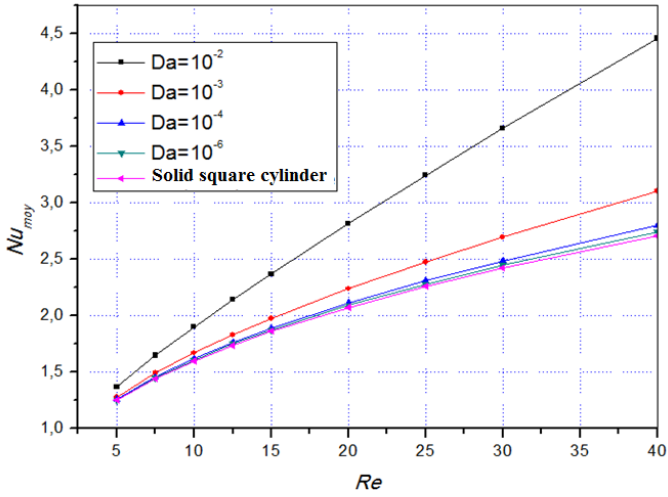


Figure 5: Variation of the average Nusselt number with Reynolds number for different Darcy numbers.

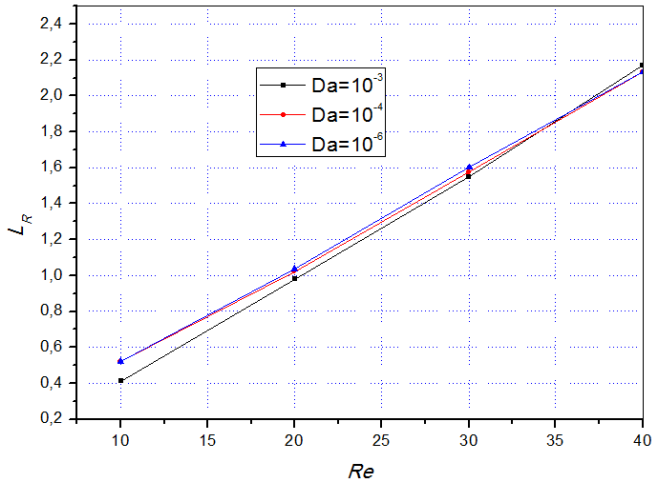


Figure 6: Variation of recirculation wake length with Reynolds number for different Darcy numbers.

### 5. Conclusion

The laminar flow of an incompressible fluid around and through a square cylinder maintained at a constant temperature and placed between two parallel

plates has been studied. The equations governing this flow are solved numerically by the finite volume method using the SIMPLE algorithm. The effects of Reynolds and Darcy numbers on the flow and heat transfer characteristics have been presented. The following conclusions have been drawn from the studies presented:

The drag coefficient increases with the decrease in the Darcy number and this approximates the case of a flow through a solid body for  $Da = 10^{-6}$ .

For high permeability, the fluid receives a slight resistance to penetration into the square cylinder and thus the absence of the recirculation zone for different values of the Reynolds number.

The length of the recirculation zone increases with the increase of the number of Reynolds and decreases slightly with the increase of the Darcy number for  $Re < 35$ .

The transfer rate increases with the increase of the Reynolds number on the one hand and with the increase of the permeability of the material on the other hand.

## References

- [1] Breuer, M., Bernsdorf, J., Zeiser, T., and Durst, F., "Accurate computations of the laminar flow past a square cylinder based on two different methods: lattice-Boltzmann and finite-volume", in *Int. J. of Heat and Fluid Flow*, vol. 21, pp. 186-196, 2000.
- [2] Gupta, A.K., Sharma, A., Chhabra, R.P., and Eswaran, V., "Two dimensional steady flow of a power law fluid past a square cylinder in a plane channel: momentum and heat transfer characteristics", in *Ind. Eng. Chem. Res.*, vol. 42, pp. 5674-5686, 2003.
- [3] Paliwal, B., Sharma, A., Chhabra, R.P., and Eswaran, V., "Power law fluid flow past a square cylinder: momentum and heat transfer characteristics", in *Chem. Eng. Sci.*, vol. 58, pp. 5315-5329, 2003.
- [4] Dhiman, A.K., Chhabra, R.P., and Eswaran, V., "Steady flow of power-law fluids across a square cylinder", in *Chemical Engineering Research and Design*, vol. 84(A4), pp. 300-310, 2006.
- [5] Dhiman, A. K., Chhabra, R. P., Sharma, A., and Eswaran, V., "Effects of Reynolds and Prandtl numbers on heat transfer across a square cylinder in the steady flow regime", in *Numerical Heat Transfer, Part A*, vol. 49, pp. 717-731, 2006.
- [6] Sharma, N., Dhiman, A.K., and Kumar, S., "Mixed convection flow and heat transfer across a square cylinder under the influence of aiding buoyancy at low Reynolds numbers", in *Int.J. Heat Mass Transfer* vol. 48, pp. 2601-2614, 2012.
- [7] Alazmi, B., and Vafai, K., "Analysis of fluid and heat transfer interfacial conditions between a porous medium and fluid layer", in *Int.J. Heat Mass Transfer*, vol. 44, pp. 1735-1749, 2001.
- [8] Yu, P., Zeng, Y., Lee, T.S., Bai, H.X., and Low, H.T., "Wake structure for flow past and through square cylinder", in *Int.J. Heat and fluid flow* vol. 31, pp. 141-153, 2010.
- [9] Wu, H.-W., and Wang, R.-H., "Convective heat transfer over a heated square porous cylinder in a channel", in *Int.J. Heat Mass Transfer*, vol. 53, pp. 1927-1937, 2010.
- [10] Dhinakaran, S., and Pormmozhi, J., "Heat transfer from a permeable square cylinder to a flowing fluid", in *Energy conversion and management*, vol. 52, pp. 2170-2182, 2011.

- 
- [11] Dhiman, A.K., Chhabra, R.P. and Eswaran, V., "Flow and heat transfer across a confined square cylinder in the steady flow regime : effect of the Peclet number", in *Int.J. Heat Mass Transfer*, vol. 48, pp. 4598-4614, 2007.
  - [12] Mahdhaoui, H., Chesneau, X., and Laatar, A.H., "Numerical simulation of flow through a porous square cylinder", in *Energy Procedia.*, vol. 139, pp. 785-790, 2017.
  - [13] Patankar, S.V., "Numerical Heat Transfer and Fluid Flow", McGraw-Hill, New York, 1980.



## Study of Powder Particle Size Effect on Microstructural and Geometrical Features of Laser Claddings Using Response Surface Methodology RSM

El Hadi BOUSSAHA<sup>1</sup>, Samia AOUCI<sup>2</sup>, Hamdi AOUCI<sup>3</sup>,  
Abida BAHLOUL<sup>4</sup>

<sup>1</sup> Department of Petrochemistry and Process Engineering, Faculty of Technology, Université 20 Août 1955 Skikda, Algeria, e-mail: bhedi3@yahoo.fr

<sup>2</sup> Department of Mechanical Engineering, Faculty of Technology, Université 20 Août 1955 Skikda, Algeria, e-mail: auoici\_s@yahoo.fr

<sup>3</sup> Higher National School of Technology, Rouiba, Algeria, e-mail: hamdi.aouici@enst.dz

<sup>4</sup> L.A.I.G.M. Laboratory, Faculty of Science and Technology University of Guelma, BP. 401, Algeria, e-mail: abida\_bahloul@yahoo.fr

Manuscript received September 22, 2018; revised May 3, 2019

**Abstract:** A continuous CO<sub>2</sub> laser (10.6  $\mu\text{m}$  wavelength) was adopted to investigate the influence of powder particle sizes on microstructural and morphological characteristics of laser claddings.

To study the potential of powder in controlling the incident laser energy, different average particle sizes of Ni-base powder were deposited on an austenitic stainless steel X3CrNi18-10 substrate. The energy value necessary to melt a mass  $m$  of powder was calculated. The results indicate that this energy decreases with particle sizes.

The claddings obtained with small particle sizes revealed a good morphological aspect and a low dilution of the cladding layer in the substrate, yet enough to create a very good metallurgical bond. The residual stress state was also influenced. Concerning modeling, we have elaborated residual stress model in the case of laser cladding by exploiting the response surface methodology (RSM), using a quadratic regression model. Combined effects of three laser cladding parameters on the residual stress is explored by a statistical analysis of variance (ANOVA). Results show that the residual stress is influenced principally by the power delivered by laser beam and by the scanning speed. It is also indicated that the size of powder particle is the dominant factor affecting the residual stress.

**Keywords:** Laser cladding, particle size, energy absorption, morphology, microstructure, RSM, ANOVA.

## 1. Introduction

The availability of high power lasers has opened many new and diversified applications in several technological areas [1,3]. The laser cladding obtained by powder injection offers the possibility to apply a broad variety of metallurgical and ceramic coatings on the surface of materials. The Ni-Cr alloys are widely used in the glassware industry for coating parts working at high temperature in order to ensure a protection against corrosion and abrasion [4,5]. However, the quality of the coatings with regard to microstructural defects (cracking and porosity), mechanical properties (microhardness and wear resistance) and residual stresses state depends on many parameters such as laser power, powder feed rate and beam focus relative to the substrate surface and usually, no systematic study of the combined influence of these parameters was carried out. Such an investigation appears very useful for obtaining the appropriate operating conditions.

The influence of processing conditions on geometrical features of laser claddings obtained by powder injection has been studied [6,7]. However, the relationship between the powder characteristics and geometrical features of laser claddings has not been thoroughly examined.

Furthermore, it has been shown that the amount of the photonic energy participating in the resulting heating of the powder is strongly dependent on the screen opacity formed by the powder [8]. So the particle size appears like one of the predominant factors.

The aim of this work was to study the influence of particle sizes on the microstructure and morphological aspect of claddings obtained by powder injection with a continuous wave CO<sub>2</sub> laser. Deposition is made on an austenitic stainless steel (304L). Coaxial powder injection is chosen to localize the powder flow in the previously formed cladding.

Different particle sizes of powder have been chosen in order to investigate their effects on the laser absorption and consequently on the properties of laser claddings. Concerning modeling, we have elaborated the residual stresses model in the case of laser claddings by exploiting the response surface methodology (RSM), using a quadratic regression model. Combined effects of particle sizes ( $d$ ,  $\mu\text{m}$ ), laser power ( $P$ ,  $W$ ) and scan speed ( $V$ ,  $\text{mm/s}$ ) parameters on the performance of residual substrate and deposit stress are explored by a statistical analysis of variance (ANOVA).

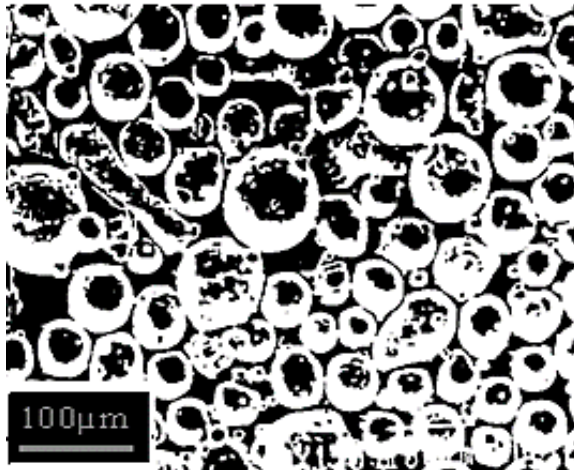
This article concludes with a number of suggestions for improving the quality of laser claddings.



## 2. Experimental procedure

### 2.1 Materials

A Ni-base alloy powder (PEM 133) with a particle size ranging from 20 to 120  $\mu\text{m}$  was chosen as coating material (*Fig. 1*).  $180 \times 70 \times 10 \text{ mm}^3$  rectangular samples of an austenitic stainless steel X3CrNi18-10 (304L) have been used as substrates. The chemical compositions (in wt. %) are listed in *Table 1*. These materials were selected because they have different machining characteristics and are important in industry [9]. Prior to the laser cladding process, the sample surface was degreased with acetone and cleaned with alcohol.



*Figure 1:* Optical micrograph showing particle sizes and shapes of the Ni-base powder.

*Table 1:* Chemical composition (wt. %) of Ni-alloy powder coating and stainless steel substrate

Elements	C	B	Si	Cr	Fe	Ni	Mn	P
Powder (PEM 133)	0.65	3.15	4.4	14	4	Balance		
X3CrNi18-10 (304L)	0.03	-	0.75	18	68.7	10	1.5	0.02

### 2.2 Laser claddings

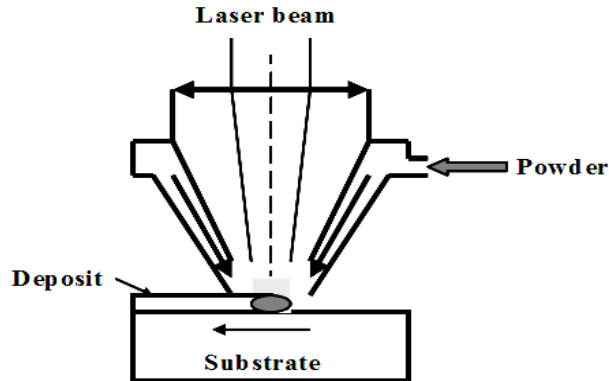
Specimens were mounted on a numerically controlled X-Y table and irradiated with a continuous wave CO<sub>2</sub> laser (10.6  $\mu\text{m}$  wavelength), the power of which can reach 3.6 kW.

A 191 mm focal-length lens was employed to focus the beam at a distance of 20 mm away from the specimen surface. The claddings were achieved by

spraying alloy powders using a Metco 4 MP spray system. Argon was used to prevent oxidation and protect the alloy powder which was injected towards the molten pool via a coaxial nozzle (*Fig. 2*).

The parameters used for the treatments were as follows:

Laser power:  $1500 < P < 2200$  W; scanning speed:  $5 < V < 10$  mms-1; beam diameter at the impinging point:  $1.5 < d_b < 2$  mm.



*Figure 2:* Coaxial nozzle.

### 2.3 Characterization

Following laser irradiation, the treated zones were characterized using optical microscopy (Leitz Metallovert). Scanning electron microscope (JEOL. 840-LGS) was used to study the morphology of the claddings. For optical micrography, samples were cut with a diamond grinding wheel, polished with abrasive paper, then with diamond paste and etched in the following reagent: 150 cm<sup>3</sup> HCl, 25 g K<sub>2</sub>Cr<sub>3</sub>O<sub>7</sub>, 50 cm<sup>3</sup> H<sub>2</sub>O.

The residual stress fields were obtained by measuring the deformation resulting from the successive removal of thin layers [10, 11]. This method so-called bending deflection method doesn't generate any stresses [12].

### 3. Results and discussion

The thermo-physical data and mechanical properties of most alloys are poorly known, especially at high temperature. In addition, the high thermal gradients and cooling rates generated during laser treatment render difficult an estimation of the phase transformations [12, 13]. Therefore, only qualitative trends will be discussed below.

### 3.1 Energy statement

When the laser beam has irradiated the surface of material, long enough, the surface temperature reaches the melting temperature ( $T_M$ ). The material begins to absorb the latent heat of fusion ( $\Delta H_M$ ) and a molten liquid-solid interface propagates into the material. The minimum energy required to melt a mass,  $m$  of this material is given by:

$$E = m(c\Delta T + \Delta H_M), \quad (1)$$

with  $\Delta T = T_M - T_0$ , where  $T_0$  is the initial temperature and  $c$  is the specific heat capacity.

In the present study; the main compounds of the powders are iron, nickel and chromium. These transition elements have similar properties [14]. Then these elements can be considered to have the following average values of the parameters.

$$\rho = 8000 \text{ kg m}^{-3}, c = 0.5 \text{ kJ} \cdot \text{kg}^{-1} \cdot \text{K}^{-1}, \Delta H_M = 250 \text{ kJ} \cdot \text{kg}^{-1}, T_M = 1500 \text{ }^\circ\text{C}.$$

So, melting 1g of material requires approximately 1000J. However, this value has to be modified since the efficiency  $\gamma$  of the laser cladding process is lower than 100% and part of the energy is reflected by the powder. This rate is characterized by the reflectivity  $R$ .

In this investigation, both factors have been taken into account. Assuming that  $R$  does not change significantly before the surface reaches its melting point, the minimum energy becomes:

$$E = 1000 \frac{F\gamma}{(1-R)}, \quad (2)$$

where  $F$  is the powder feed rate,  $1-R=A$  is the coefficient of absorptivity, and  $E$  is expressed in  $\text{J} \cdot \text{g}^{-1} \cdot \text{s}^{-1}$ .

### 3.2 Effect of particle size on the thermodynamic properties

If powder particles are assumed to be spheres, then the minimum energy required for melting a particle with an average radius  $r_p$  and a mass density  $\rho$  is described by the equation:

$$E_p = \frac{4}{3} \pi \rho (r_p)^3 [c\Delta T + \Delta H_m] \quad (3)$$

For example, the amount of energy required to melt large particle size ( $r_p = 50 \text{ } \mu\text{m}$ ) is about 125 times larger than the amount that would have been required by small ones ( $r_p = 10 \text{ } \mu\text{m}$ ) and consequently we can see the effect of particle size on the thermodynamic properties of materials, especially the

amount of energy required for melting a small particle size smaller than that of larger size. Physically, this means the absorption of laser energy is a much localized surface phenomenon. The reduction in the size of the particle for a given powder mass leads to a multiplication of these surfaces and consequently to an increase in the resulting absorption.

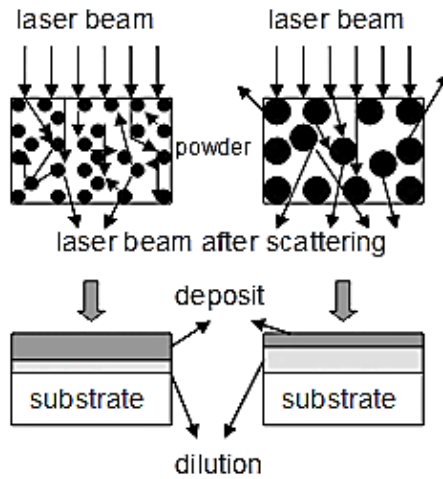
### 3.3 Effect of particle size on the screen opacity

The reflectance  $R$  of the surface is an important factor. It defines how much of the energy incident on the surface is reflected. Reflected energy, of course, does not contribute to the heating. In the present case this assumption appears realistic, since the average dimensions of powder particles are large enough. Therefore, the absorptivity is essentially equal to  $(1-R)$ .

In practice as we have seen above the minimum energy does change significantly with the particle sizes. When the particle size is large enough (average particle size:  $r_p = 50 \mu\text{m}$ ), the powder forms a dispersed particle screen for the incident laser beam, which interacts only once with each particle. Consequently, only a small fraction of the incident energy is absorbed by the powder. Whereas, small particle size (average particle size:  $r_p = 15 \mu\text{m}$ ) induces a concentrated screen, within which each particle is submitted to a multiple scattering phenomenon (*Fig. 3*).

This phenomenon leads to an increase in absorption and then to a better efficiency of the laser cladding process.

A simple observation indicates that if the laser beam interacts  $n$  times with particles the absorbed energy is no longer  $E(1-R)$  but  $E(1-R^n)$ . Taking for example  $\gamma = 30\%$ ,  $F = 30 \text{ g}\cdot\text{min}^{-1} (=0.5 \text{ g s}^{-1})$ , and  $R = 50\%$ , we obtain for large particles ( $n = 1$ ):  $E = 300 \text{ J}$  and for small ones ( $n = 2$ ):  $E = 450 \text{ J}$ . The amount of energy absorbed by small particles ( $r_p = 10 \mu\text{m}$ ) is about 1.5 times larger than the amount that would have been absorbed by the particles with great dimensions ( $r_p = 50 \mu\text{m}$ ).



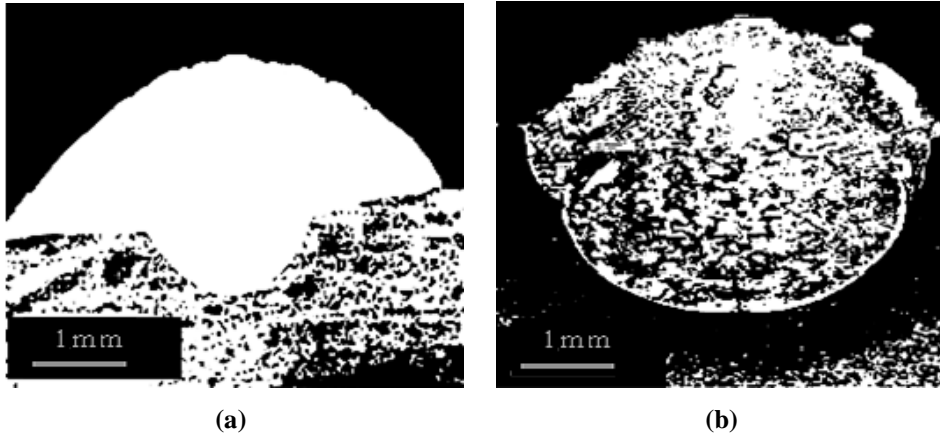
(a) Small particle size      (b) Dispersed particle screen

*Figure 3:* Schematic illustration showing the multiple scattering phenomenon within the screen formed by the powder and its effect on the geometrical characteristics of the cladding. (a) small particle size, (b) dispersed particle screen.

## 4. Laser claddings properties

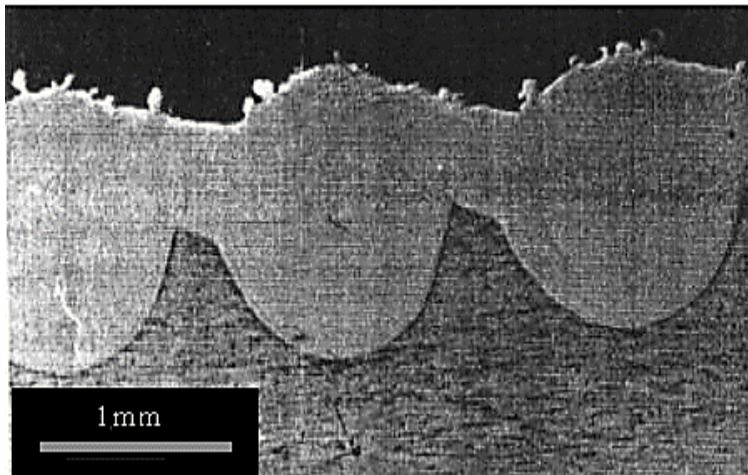
### 4.1 Morphological aspect and dilution rate

The dilution rate is defined as the ratio of the thickness of the cladding layer to the total thickness in which melting occurred. *Fig. 4* shows the optical micrograph of the cladding layers formed with different particle sizes at a laser power of 1600 W and a scan speed of  $6.6 \text{ mm s}^{-1}$ . The thickness of coatings was about 1.5 mm. The clad layer obtained with small particle size presents a good morphological aspect with a low dilution rate (*Fig.4a*). While the cladding obtained with large particle sizes shows a very high dilution with partially molten particles at the top surface (*Fig.4b*). This is probably due to the fact that during the flight through the laser beam, large particles are heated or only partially molten. Melting occurs when the powder reaches the melt zone that has been initiated on the substrate.



*Figure 4:* Optical micrographs showing the morphological aspect and the dilution rate of the clad layer: a) small particle size, b) large particle size.

The small particles are melted by the laser beam before reaching the melting zone (Figure 5), which gives a good morphological appearance of the coating while using the optimized parameters of the treatment

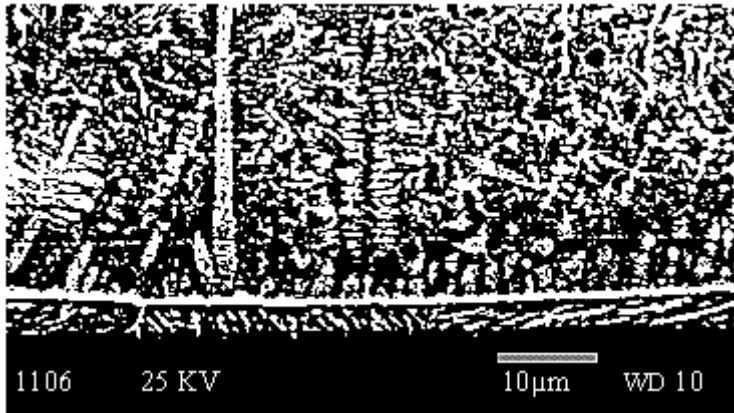


*Figure 5:* Optical micrograph showing the overlapping passes which resulted in coating.

#### 4.2 Microstructure

The cladings obtained with different particles sizes revealed a cellular and dendritic microstructure which is typical of laser cladding. However, the microstructure of the cladding layer obtained with small particles size showed

columnar growth traversing the cross section (*Fig.6*). In addition, a region with a thickness of few micrometers, corresponding to planar front growth was also observed at the interface between the substrate and the cladding layer. This is may be attributed to the effect of the particle size on the solidification rate and thermal gradients.



*Figure 6:* SEM micrograph showing the typical microstructure of the clad layer obtained with small particle sizes: directional solidification from a planar interface.

#### 4.3 Residual stress state

It was observed (*Fig.7*) on residual stress profiles of the coatings obtained with different particle sizes on an austenitic stainless steel substrate, that the form of the stress distribution is not affected by the change of the particle size: high tensile stresses in the coating followed by a rapid decrease in compression at the interface coating/base material. However, the magnitude of these stresses decreases with the particle size. The claddings obtained with small size particles result in moderate tensile stresses in the surface and subsurface regions, with a smooth transition from tension to compression with depth.

These differences may be attributed to thermal cycles much faster and higher for the great particles than those obtained with small ones.

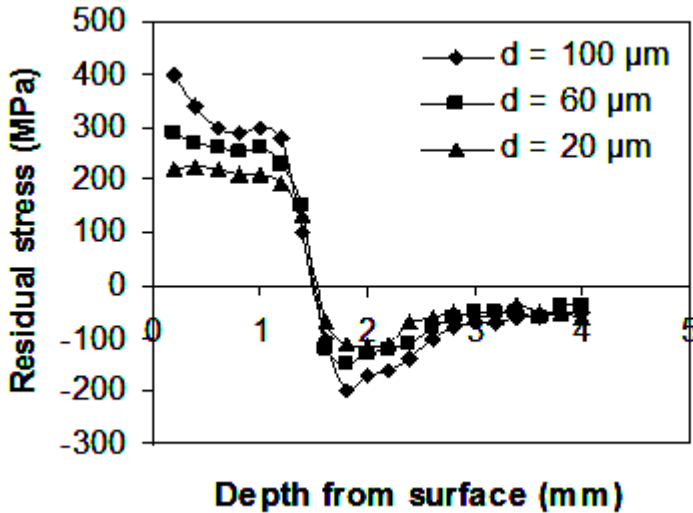


Figure 7: Residual stress fields of Ni-alloy coatings on stainless steel substrate for different average particle sizes,  $d$ .

## 5. Statistical analysis

### 5.1 Response surface methodology

Response surface methodology is an experimental technique used for predicting and modeling complicated relations between independent factors and one or more responses. In addition, the performance of RSM which is a well-recognized method in finding optimum condition is evaluated for finding optimal values of cutting parameters to minimize the values of cutting force components. To achieve these aims the following steps are designated: (1) defining the independent input variables and the desired output responses, (2) adopting an experimental design plan, (3) performing regression analysis with the quadratic regression models of RSM, (4) calculating the ANOVA for the independent input variables in order to find parameters which significantly affect the response, (5) determining the situation of quadratic regression models of RSM and finally, (6) optimizing, conducting confirmation experiment and verifying the predicted performance characteristics [15].

In our study particle sizes ( $d$ ,  $\mu\text{m}$ ) (diameter of the particle), laser power ( $P$ , W) and scan speed ( $V$ , mm/s) have been chosen as process parameters. The residual stresses have been chosen as response factor.



The relationship between the input parameters and the output parameters is given:

$$Y = \phi(S, P, V), \quad (4)$$

where  $Y$  is the desired the microstructural and geometrical aspect and is the response function. The approximation of  $Y$  is proposed by using a multiple linear mathematical model, which is suitable for studying the interaction effects of process parameters on microstructural and geometrical characteristics. In the present work, the RSM based multiple linear mathematical model is given by the following:

$$Y = a_0 + \sum_{i=1}^k b_i X_i + \sum_{i,j}^k b_{ij} X_i X_j, \quad (5)$$

where  $a_0$  is the free term of the regression equation, the coefficients  $b_1, b_2, \dots, b_k$  and  $b_{12}, b_{13}, \dots, b_{kk}$  are the linear and the interaction terms, respectively.  $X_i$  represents input parameters ( $d, P$  and  $V$ ). The output (residual stresses  $\sigma_s$  and  $\sigma_d$ ) is also called the response factors.

The experimental plan and result of the trials is reported in *Table 2*. Based on  $3^3$  full factorial design, a total of 27 tests were carried out. The range of each parameter is set at three different levels, namely particle sizes, laser power and scan speed.

## 5.2 Experiments design

The plan of tests was developed with the aim of relating the influence of particle sizes ( $\mu\text{m}$ ), laser power (W) and scan speed (mm/s), with the residual substrate stress  $\sigma_s$  and residual deposit stress  $\sigma_d$ . *Table 4* shows all values of residual stresses  $\sigma_s$  and  $\sigma_d$ . The residual stresses  $\sigma_s$  and  $\sigma_d$  were obtained in the range of 200 – 440; -220 – -90 MPa for  $\sigma_s$  and  $\sigma_d$ .

Table 2: Experimental plan and results

N°	Input parametric			Output responses	
	$d, \mu\text{m}$	$P, \text{W}$	$V, \text{mm/s}$	$\sigma_s, \text{MPa}$	$\sigma_d, \text{MPa}$
1	20	1600	5.5	220	-115
2	20	1600	6.6	210	-110
3	20	1600	9	200	-90
4	20	1800	5.5	235	-120
5	20	1800	6.6	220	-115
6	20	1800	9	205	-109
7	20	2000	5.5	250	-135
8	20	2000	6.6	235	-120
9	20	2000	9	220	-122
10	60	1600	5.5	300	-145
11	60	1600	6.6	285	-140
12	60	1600	9	270	-125
13	60	1800	5.5	345	-160
14	60	1800	6.6	325	-155
15	60	1800	9	305	-130
16	60	2000	9	310	-145
17	60	2000	5.5	360	-180
18	60	2000	6.6	340	-170
19	100	1600	9	375	-170
20	100	1600	6.6	385	-180
21	100	1600	5.5	400	-200
22	100	1800	9	380	-175
23	100	1800	6.6	390	-172
24	100	1800	5.5	425	-210
25	100	2000	6.6	420	-210
26	100	2000	5.5	440	-220
27	100	2000	9	400	-200

### 5.3 Analysis of variance ANOVA

The statistical significance of the fitted quadratic models was evaluated by the Prob. values of ANOVA. In the ANOVA table, the sum of squares is used to estimate the square of deviation from the significant mean. Mean squares are estimated by separating the sum of squares by degrees of freedom. F ratio is an index used to check the suitability of the model in which the calculated value of F should be greater than the F-table value. F-table value corresponding 95% confidence level in calculation of process parameters accurately is

$F_{0.05, 1, 20} = 4.35$ . The model is suitable at a 95 % confidence level because the calculated F value is greater than the F value from the table. When the Prob. values are <95 % confidence (0.05), the models achieved are considered

statistically significant. The Design-Expert (State-Ease, version 8) software was used for a statistical analysis of experimental data and to generate the response surface. Table 3 shows that the particle sizes ( $d$ ,  $\mu\text{m}$ ) have the statistically most significant influence on the residual substrate stress  $\sigma_s$ , followed by laser power ( $P$ , W) and scan speed ( $V$ , mm/s), their contributions being (3.68 and 3.29) %, respectively. The interactions ( $d \times P$ ), ( $d \times V$ ) and ( $P \times V$ ) are not significant. Respectively, their contributions are (0.03; 0.04 and 0.11) %. The determination coefficient model's  $R^2$  is 0.9896. The Pred.  $R^2$  of 0.9834 is in reasonable agreement with the Adj.  $R^2$  of 0.9864. The equation in terms of real factors is given as follows:

$$\sigma_s = -40,922 + 1,991d + 0,151P + 11,660V + 0,00026d \times P - 0,029d \times V - 0,011P \times V \quad (6)$$

Table 3: ANOVA of residual substrate stress  $\sigma_s$

Source	Sum of squares	DF	Mean square	F-value	Prob.	Cont. %	Remarks
Model	157155.003	6	26192.500	315.960	< 0.0001		Significant
$d$ , $\mu\text{m}$	141843.108	1	141843.108	1711.056	< 0.0001	92.85	Significant
$P$ , W	5625.144	1	5625.144	67.856	< 0.0001	3.68	Significant
$V$ , mm/s	5022.951	1	5022.951	60.592	< 0.0001	3.29	Significant
$d \times P$	52.083	1	52.083	0.628	0.4373	0.03	Not significant
$d \times V$	55.046	1	55.046	0.664	0.4247	0.04	Not significant
$P \times V$	174.921	1	174.921	2.110	0.1618	0.11	Not significant
Error	1657.959	20	82.897				
Total	158812.963	26				100	
SD = 9.104					$R^2 = 0.9896$		
Mean = 312.963					$R^2$ Adjusted = 0.986		
Coefficient of variation = 2.909					$R^2$ Predicted = 0.983		
Predicted residual error of sum of squares (PRESS) = 2638.9726					Adequate precision = 53.471		

The ANOVA results of residual deposit stress  $\sigma_d$  presented in Table 4 show that the most significant model term is the particle sizes ( $d$ ) with 82.78 % of contribution, followed by  $P$  with lower contribution of 8.94 %. The term  $V$  appears especially significant on thrust force. Its contribution is 7.95 %. On the opposite side, the interactions ( $d \times P$ ), ( $d \times V$ ) and ( $P \times V$ ) are not significant. Respectively, their contributions are (0.08; 0.22 and 0.02) %. The coefficient  $R^2$  of about 0.9631 is considered good, but the Pred.  $R^2$  of 0.9283 which represents the efficiency of the model to expect new runs is not as close to the Adj.  $R^2$  of 0.9520. The equation in terms of real factors resulted from the backward elimination process is given as follows:

$$\sigma_d = -55,521 - 0,874d - 0,037P + 8,31V - 0,00018d \times P + 0,0339d \times V - 0,0021P \times V \quad (7)$$

Table 4: ANOVA of residual deposit stress  $\sigma_d$

Source	Sum of squares	DF	Mean square	F-value	Prob.	Cont. %	Remarks
Model	32794.411	6	5465.735	86.949	< 0.0001		Significant
$d, \mu\text{m}$	26310.995	1	26310.995	418.558	< 0.0001	82.78	Significant
$P, W$	2841.184	1	2841.184	45.197	< 0.0001	8.94	Significant
$V, \text{mm/s}$	2527.234	1	2527.234	40.203	< 0.0001	7.95	Significant
$d \times P$	27	1	27	0.429	0.5197	0.08	Not significant
$d \times V$	70.795	1	70.795	1.126	0.3012	0.22	Not significant
$P \times V$	6.604	1	6.604	0.105	0.7492	0.02	Not significant
Error	1257.218	20	62.860				
Total	34051.629	26				100	
SD = 7.928				$R^2 = 0.9631$			
Mean = -152.703				$R^2$ Adjusted = 0.952			
Coefficient of variation = 5.1921				$R^2$ Predicted = 0.928			
Predicted residual error of sum of squares (PRESS) = 2441.888				Adequate precision = 31.180			

The predicted values of response factors illustrating residual substrate stress  $\sigma_s$  and residual deposit stress  $\sigma_d$ , from regression Eqs. (6) – (7) corresponding to different combinations of input parameters, are reported in Table 2.

Fig. 8 shows the comparison between the predicted and measured values of residual substrate stress  $\sigma_s$  and residual deposit stress  $\sigma_d$ . It is concluded that the results of the comparison prove that predicted values of the residual stresses ( $\sigma_s$  and  $\sigma_d$ ) are very close to those determined experimentally.

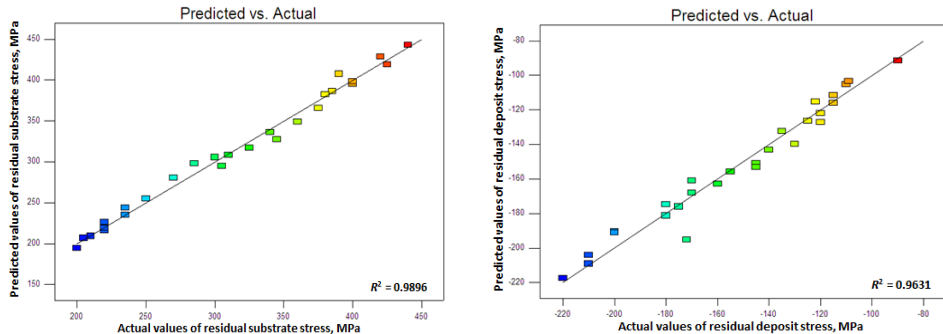


Figure 8: Comparison between measured and predicted values for residual stresses ( $\sigma_s$  and  $\sigma_d$ ).

Fig. 9 represents a perturbation plot for the ( $\sigma_s$  and  $\sigma_d$ ), in which the line represented by the different factors, particle sizes (A), laser power (B) and scan speed (C) revealed their individual behaviors on ( $\sigma_s$  and  $\sigma_d$ ), respectively, keeping other parameters constant. Fig. 8 depicts an increasing trend of residual stresses by increasing the particle sizes (A), where as a decreasing trend with increase in scan speed (C).

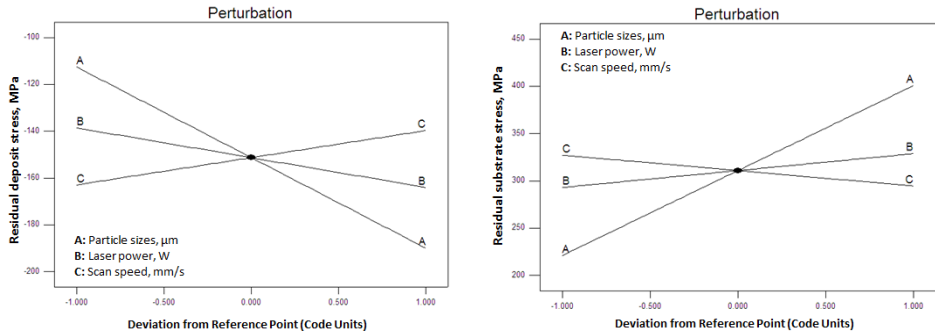


Figure 9: Effect of input parameters on  $\sigma_s$  and  $\sigma_d$ .

In order to investigate the influence of the scan speed and laser power parameters at various particle sizes on the residual stresses (substrate stress  $\sigma_s$  and deposit stress  $\sigma_d$ ), response surface is drawn in Fig. 10. Fig. 10 depicts the influence of scan speed (V) and laser power (P) on the residual stresses (stress  $\sigma_s$  and  $\sigma_d$ ), reported before. The highest residual stresses are achieved with the combination of the highest scan speed and the highest laser power when the particle sizes (d) are kept at high level.

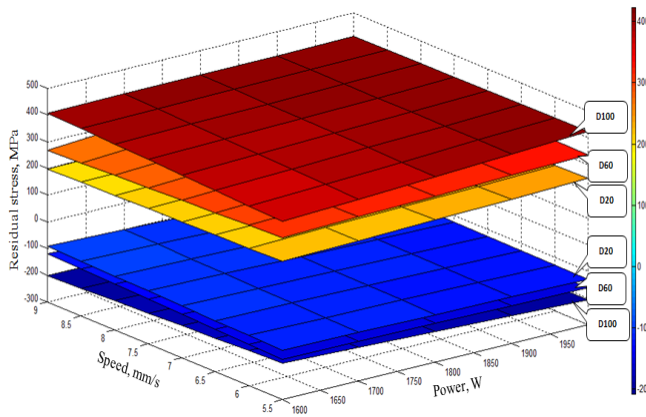


Figure 10: Effect of the scan speed and laser power on the residual stresses.

### 5.4 Optimization of input conditions

In the present study, the desired function optimization of the RSM has been employed for residual substrate and deposit stress optimizations using Design Expert Software. The goals and the parameter ranges defined for the optimization process are summarized in *Table 5* for minimizing the values of the residual stresses (substrate stress  $\sigma_s$  and deposit stress  $\sigma_d$ ). The desirability levels are constant up to solutions no. 8. After these solutions (*Table 6*), the desirability levels decrease when the operating parameter is changing. So, we can conclude that in the case of the highest particle sizes, highest laser power and lowest scan speed, the performances of the deposit are optimized and the desirability levels are (83.65 and 83.23) % in these conditions.

*Table 5:* Constraints for optimization of deposit conditions

Condition	Goal	Lower limit	Upper limit
Particle sizes, $d$ ( $\mu\text{m}$ )	Is in range	20	100
Laser power, $P$ (W)	Is in range	1600	2000
Scan speed, $V$ (mm/s)	Is in range	5.5	9
$\sigma_s$ (MPa)	Minimize	200	440
$\sigma_d$ (MPa)	Minimize	-220	-90

*Table 6:* Response optimization for residual substrate and deposit stress

Test n°	$d$ ( $\mu\text{m}$ )	$P$ (W)	$V$ (mm/s)	Residual stress		Desirability
				$\sigma_s$ (MPa)	$\sigma_d$ (MPa)	
1	100.00	2000.00	5.50	348.878	-217.356	0.8365
2	100.00	1999.96	5.53	348.579	-217.158	0.8359
3	100.00	2000.00	5.54	348.403	-217.042	0.8355
4	100.00	1994.31	5.50	348.262	-216.971	0.8353
5	100.00	1991.73	5.50	347.985	-216.799	0.8348
6	100.00	2000.00	5.58	347.951	-216.744	0.8346
7	100.00	1987.81	5.50	347.561	-216.534	0.8340
8	100.00	2000.00	5.67	346.881	-216.038	0.8323

## 6. Conclusion

Based on a study of the influence of powder particle size on the characteristics of coatings the following conclusions are made:

- Absorption of beam laser energy is a much localized surface phenomenon.

- Reducing particle sizes leads to an increase in the resulting laser absorption.

- Small particles sizes form a dense screen with the appearance of a multiple scattering phenomenon which absorbs very efficiently the incident laser beam.

Consequently, the laser energy density may be reduced and good morphological aspects of claddings with an optimal dilution, enough to create good metallurgical bond, can be obtained. In addition, low levels of residual stresses can be obtained because of thermal gradients attenuation. Further, experiments are in progress to study the case of very small particle sizes, especially by using spherical shape particles of uniform diameter.

- Also, the results of ANOVA and the validation experiments confirm that the developed mathematical model shows excellent fit and predicted values are very close to experimental values.

- The residual substrate stress ( $\sigma_s$ ) and residual deposit stress ( $\sigma_d$ ) are influenced principally by the particle sizes factor with contribution of (82.78 and 92.85) %, respectively.

## 7 References

- [1] Yakovlev, A., Bertrand, P., and Smurov, I., "Laser Cladding of Wear Resistant Metal Matrix Composite Coatings", *Thin Solid Films*, v. 453-454, pp. 133-138, 2004.
- [2] Pei, Y.T., Ouyang, J.H., and Lei, T.C., "Microstructure of bonding zones in laser-clad Ni-alloy-based composite coatings reinforced with various ceramic powders", *Surf. Metall. Mater. Trans.*, vol. 27A2, pp. 391-400, 1996.
- [3] Hidouci, A., Pelletier, J.M., Ducoin, F., Dezert, D., and El Guerjouma, R., "Microstructural and mechanical characteristics of laser coatings", *Surface and Coatings Technology*, vol. 123, pp. 17-23, 2000.
- [4] Safonov, A.N., and Aleksenko, S., "Effect of laser treatment on the wear resistance of steels", *Metal Science and Heat treatment*, vol. 40, pp. 399-401, 1998.
- [5] Sexton, C.L., Byrne, G., and Walkins, K.G., "Alloy development by laser cladding: an overview", *Journal of Laser Applications*, vol. 13, pp. 2-11, 2001.
- [6] De Oliveira, U., Ocelik, V., and De Hosson, J.T.M., "Analysis of coaxial laser cladding processing conditions", *Surface and Coatings Technology*, vol. 197, pp. 127-136, 2005.
- [7] Sallamand, P., "Alliage de surface et revêtements élaborés sous faisceau laser par projection de poudre sur substrat base aluminium: caractérisation microstructurale, mécanique et tribologique", *Thesis*, INSA de Lyon, 1994.
- [8] Pelletier, J.M., Sahour, M.C., Pilloz, M., and Vannes, A.B., "The Influence of processing conditions on geometrical features of laser claddings obtained by powder injection", *Journal of Materials Science*, vol. 28 (19), pp. 5184-5188, 1993.
- [9] Jackson, M.J., and O'Neill, W., "Laser micro-drilling of tool steel using Nd:YAG lasers", *Journal of Materials Processing Technology*, vol. 142 (2), pp. 517-525, 2003.
- [10] Laracine, M., Bignon, C., Lormand, M., Vannes, A.B., and Bedrin, C., "Determination of residual stresses in multimaterial, multilayer pieces : adaptation to ceramic coatings", *CIRP Annals*, vol. 40, pp. 535-539, 1991.

- 
- [11] Laribi, A., Mesrati, N., Vannes, A.B., and Treheux, D., “Adhesion and residual stresses determination of thermally sprayed molybdenum on steel”, *Surface and Coating Technology*, Elsevier, vol. 166, pp. 206-212, 2003.
  - [12] Flavenot, J.F., “Mesure des Contraintes Résiduelles: Methode de la Flèche - Methode de la Source des Contraintes”, *Les mémoires techniques du CETIM*, vol. 31, 1977.
  - [13] De, A., and DebRoy, T., “A smart model to estimate effective thermal conductivity and viscosity in the weld pool”, *Journal of Applied Physics*, vol. 95 (9), pp. 5230-5240, 2004.
  - [14] Monaghan, B.J., Neale, J.G.J., and Chapman, L., “Some Thermal Properties of a Copper–Tin Alloy”, *International Journal of Thermophysics*, Springer, vol. 20 (4), pp. 1051-1060, 1999.
  - [15] Touloukian, S., and Dewitt, D.P., *Thermophysical Properties of Matter*, Vol. 8, p. 31, IFI/Plenium New York, N.Y. 1972.
  - [16] Aouici, H., Yallese, M.A., Chaoui, K., Mabrouki, T., and Rigal, J.-F., “Analysis of surface roughness and cutting force components in hard turning with CBN tool: prediction model and cutting conditions optimization”, *Measurement*, vol. 45, pp. 344–353, 2012.



# Acta Universitatis Sapientiae

The scientific journal of Sapientia Hungarian University of Transylvania (Cluj-Napoca, Romania) publishes original papers and surveys in several areas of sciences written in English.

Information about each series can be found at

<http://www.acta.sapientia.ro>.

## Editor-in-Chief

László DÁVID

## Main Editorial Board

Laura NISTOR  
Ágnes PETHŐ

Zoltán KÁSA

András KELEMEN  
Emőd VERESS

# Acta Universitatis Sapientiae Electrical and Mechanical Engineering

## Executive Editor

András KELEMEN (Sapientia Hungarian University of Transylvania, Romania)  
[kandras@ms.sapientia.ro](mailto:kandras@ms.sapientia.ro)

## Editorial Board

Dénes FODOR (University of Pannonia, Hungary)

Katalin GYÖRGY (Sapientia Hungarian University of Transylvania, Romania)

Dionisie HOLLANDA (Sapientia Hungarian University of Transylvania, Romania)

Maria IMECS (Technical University of Cluj-Napoca, Romania)

András KAKUCS (Sapientia Hungarian University of Transylvania, Romania)

Levente KOVÁCS (Óbuda University, Hungary)

András MOLNÁR (Óbuda University, Hungary)

Géza NÉMETH (Budapest University of Technology and Economics, Hungary)

Csaba SIMON (Budapest University of Technology and Economics, Hungary)

Gheorghe SEBESTYÉN (Technical University of Cluj-Napoca, Romania)

Iuliu SZÉKELY (Sapientia Hungarian University of Transylvania, Romania)

Imre TIMÁR (University of Pannonia, Hungary)

Mircea Florin VAIDA (Technical University of Cluj-Napoca, Romania)

József VÁSÁRHELYI (University of Miskolc, Hungary)



Sapientia University



Scientia Publishing House

ISSN 2065-5916

<http://www.acta.sapientia.ro>

# Information for authors

**Acta Universitatis Sapientiae, Electrical and Mechanical Engineering** publishes only original papers and surveys in various fields of Electrical and Mechanical Engineering. All papers are peer-reviewed.

Papers published in current and previous volumes can be found in Portable Document Format (PDF) form at the address: <http://www.acta.sapientia.ro>.

The submitted papers must not be considered to be published by other journals. The corresponding author is responsible to obtain the permission for publication of co-authors and of the authorities of institutes, if needed. The Editorial Board is disclaiming any responsibility.

The paper must be submitted both in MSWord document and PDF format. The submitted PDF document is used as reference. The camera-ready journal is prepared in PDF format by the editors. In order to reduce subsequent changes of aspect to minimum, an accurate formatting is required. The paper should be prepared on A4 paper (210 × 297 mm) and it must contain an abstract of 200-250 words.

The language of the journal is English. The paper must be prepared in single-column format, not exceeding 12 pages including figures, tables and references.

The template file from <http://www.acta.sapientia.ro/acta-emeng/emeng-main.htm> may be used for details.

Submission must be made only by e-mail ([acta-emeng@acta.sapientia.ro](mailto:acta-emeng@acta.sapientia.ro)).

One issue is offered to each author free of charge. No reprints are available.

## **Contact address and subscription:**

Acta Universitatis Sapientiae, Electrical and Mechanical Engineering  
Sapientiae Hungaricae University of Transylvania  
RO 400112 Cluj-Napoca  
Str. Matei Corvin nr. 4.  
E-mail: [acta-emeng@acta.sapientia.ro](mailto:acta-emeng@acta.sapientia.ro)

**Printed by F&F INTERNATIONAL**

Director: Enikő Ambrus